# THEORETICAL INVESTIGATION OF THE INSTABILITY OF HYBRID HALIDE PEROVSKITES

# THEORETICAL INVESTIGATION OF THE INSTABILITY OF HYBRID HALIDE PEROVSKITES

BY

CHAO ZHENG, M.S.

A THESIS

SUBMITTED TO THE DEPARTMENT OF MATERIALS SCIENCE AND ENGINEERING

AND THE SCHOOL OF GRADUATE STUDIES

OF MCMASTER UNIVERSITY

IN PARTIAL FULFILMENT OF THE REQUIREMENTS

FOR THE DEGREE OF

DOCTOR OF PHILOSOPHY

Doctor of Philosophy (2019) McMaster University

(Materials Science and Engineering) Hamilton, Ontario, Canada

| | |
|---|---|
| TITLE: | Theoretical investigation of the instability of hybrid halide perovskites |
| AUTHOR: | Chao Zheng<br>M.S. |
| SUPERVISOR: | Prof. Oleg Rubel |
| NUMBER OF PAGES: | xvii, 152 |

# Abstract

It has been 10 years since the first hybrid halide perovskite photovoltaics was fabricated. Power conversion efficiency increases from the initial 3.8% to the current 25.2%. Fabrication method envolves from spin-coating to printable technology, and we deeply experience the drastic development of hybrid halide perovskite photovoltaics.

Although hybrid halide photovoltaics render a variety of advantages over traditional photovoltaics, we still cannot find any practical application of these hybrid halide photovoltaics. There exist a few issues which hinder the commercialization of this type of solar cell. Among these issues, the long-term instability of hybrid halide perovskite is the main concern for the next development. This thesis expands on investigating the instability of hybrid halide perovskites from first principles.

In Chapter 1, two computational methods employed in the thesis: density functional theory and *Ab initio* molecular dynamics are introduced.

Theoretical investigations of the instability of $CH_3NH_3PbI_3$ using density functional theory method are mainly conducted at 0 K. The finite temperature effect on this instability of $CH_3NH_3PbI_3$ is usually neglected. In Chapter 2 of this thesis, we combined density functional calculations and additional thermodynamic data to explain the intrinsic instability of $CH_3NH_3PbI_3$ under finite temperature conditions. We also analyzed the stability under humid conditions. It is shown that the aqueous solubilities of reactants play an important role in the products' stabilities.

The Born–Haber cycle of NaCl splits the enthalpy change into several components which will give a better understanding of the origin of the corresponding enthalpy change. In Chapter 3, with the extension of the Born–Haber cycle to the hybrid halide perovskites, the reaction enthalpies which govern the intrinsic instability of ionic compounds were analyzed. We proposed a criterion that helps to filter the hybrid halide perovskites with improved stability aimed for photovoltaics.

Since the instability of $CH_3NH_3PbI_3$ is intrinsic. The long-term instability can be settled by discovering alternative perovskite absorber. In Chapter 4, based on literature research, we propose a three-membered ring cation which has a suitable size to fit into the Pb-I framework, leading to optimal band gap for photovoltaics. Besides, the cation has a good ionization energy which will potentially render better stability. Whereas, a comprehensive study of this cyclic ring based perovskite indicates that the instability of the three-membered ring cation will make it impossible to synthesize this theoretical structure.

Moisture degradation mechanisms of $CH_3NH_3PbI_3$ are investigated intensively. More importantly, for practical photovoltaics, we have to imagine different situations the modules will encounter, e.g. after a couple of years, cracks appearing on the modules are inevitable, at this stage, understanding of the degradation mechanism of $CH_3NH_3PbI_3$ according to liquid water becomes important. Chapter 6 elaborately describes a comprehensive degradation mechanism of $CH_3NH_3PbI_3$ under liquid water. We investigate the energy barrier for the first dissolution event of $CH_3NH_3PbI_3$ in water. Furthermore, thermodynamic analyses of $CH_3NH_3PbI_3$ dissolution in water clearly explain the spontaneity of $CH_3NH_3PbI_3$ degradation in water. Besides, different mechanisms of $CH_3NH_3PbI_3$ and $CsPbI_3$ dissolution in water are discussed.

# Declaration of Academic Achievements

The major research results during my PhD study were published or submitted to peer-reviewed journals. The publications and submitted manuscripts are listed as below:

Eric Tenuta, **Chao Zheng**, and Oleg Rubel. "Thermodynamic origin of instability in hybrid halide perovskites." *Scientific Reports* 6 (2016): 37654. (As a co-author of this paper, my contribution to this project accounts for 40%.) Copyright of this paper from *Scientific Reports* is retained by authors.

**Chao Zheng**, and Oleg Rubel. "Ionization energy as a stability criterion for halide perovskites." Reprinted with permission from *The Journal of Physical Chemistry C* 121, no. 22 (2017): 11977-11984. Copyright (2017) ©American Chemical Society.

**Chao Zheng**, and Oleg Rubel. "Aziridinium lead iodide: a stable, low-band-gap hybrid halide perovskite for photovoltaics." Reprinted with permission from *The Journal of Physical Chemistry Letters* 9, no. 4 (2018): 874-880. Copyright (2018) ©American Chemical Society.

Kangze Ren, **Chao Zheng**, Michael A. Brook and Oleg Rubel. "Stability of aziridinium lead iodide perovskite: ring strain and water vulnerability" (As a co-author of this paper, my contribution to this project accounts for 40%.)

**Chao Zheng**, and Oleg Rubel. "Unraveling the water degradation mechanism of

$CH_3NH_3PbI_3$." Reprinted with permission from *The Journal of Physical Chemistry C* 123, no. 32 (2019): 19385-19394. Copyright (2019) ©American Chemical Society.

In addition to the major work listed above, I also contributed for a project hosted by Prof. Oleg Rubel:

**Chao Zheng**, Shidong Yu, and Oleg Rubel. "Structural dynamics in hybrid halide perovskites: Bulk Rashba splitting, spin texture, and carrier localization." Reprinted (abstract/excerpt/figure) with permission from *Physical Review Materials* 2, no. 11 (2018): 114604. Copyright (2018) ©by the American Physical Society. (As a co-author of this paper, my contribution to this project accounts for 20%. Due to minor contribution, this paper is attached in Appendix B.)

*I would like to dedicate my thesis*

*to my beloved wife, son, and parents.*

# Acknowledgements

First of all, I would like to express special thanks to my supervisor Dr. Oleg Rubel. I appreciate Dr. Oleg Rubel to provide the chance for me to pursue a PhD degree at McMaster University. During my PhD study, I enjoy doing research with Dr. Oleg Rubel. I appreciate the kindness, patience, guidance from Dr. Oleg Rubel. The encouragement and full support from Dr. Oleg Rubel are appreciated during my whole PhD study.

Secondly, I would like to acknowledge my supervisory committee member Dr. Adrian Kitai and Dr. Yurij Mozharivskyj for giving me valuable guidance on proceeding my doctoral projects.

Thanks for Dr. Yurij Mozharivskyj and Dr. Ayse Turak at McMaster University to point out the overlooked issue of Chapter 4. During the research of Chapter 6, we are indebted to Dr. Claudine Katan, Dr. Mikaël Kepenekian and Dr. Xavier Rocquefelte from Université de Rennes 1 for commenting on the initial perovskite-water interface. Thanks for Dr. Yurij Mozharivskyj to address the entropy effect during the proceeding of Chapter 6.

I appreciate the creative discussions about research and life with our research group members: Christopher Pashartis, Divyanshu Gupta and Magdalena Laurien.

Last, but most importantly, I would like to acknowledge my wife, my son, my parents, my uncle and aunt, and all other family members for their unconditional love.

# Contents

# List of Figures

# List of Tables

# Chapter 1

# Introduction

## 1.1 World energy consumption and photovoltaics

In the next 50 years, the current 7.7 billion people will extend to 10 billion. Energy, water, food, environment, poverty, war, disease, education, democracy, and population growth are the top ten problems that human beings need to face in the future. Among them, a sustainable supply of energy takes the first place[4]. It seems that finding such a clear endless source of energy is urgent[16]. Solar energy is considered to be affordable, inexhaustible, clean and powerful. The fact is that the amount of solar energy reaching the earth within one hour can provide demand for the whole world for about one year[33]. Although solar energy seems very promising, the usage of the solar resource is quite low compared with world energy consumption, shown in Fig. 1.1. It indicates the consumption of solar energy is only $\backsim$2% among all energy consumption in 2016 and the usage of solar energy smoothly increases. A quite large amount of solar power we consume today is coming from concentrated sunlight and running stream turbines activated by the heat from boiled water or salts after absorbing solar radiation[3]. Photovoltaics contributes 30% of this amount and mainly produced by silicon-based panels[2]. Mining raw materials, fabrication of solar module, the transmission of electricity generated from solar power are responsible for the

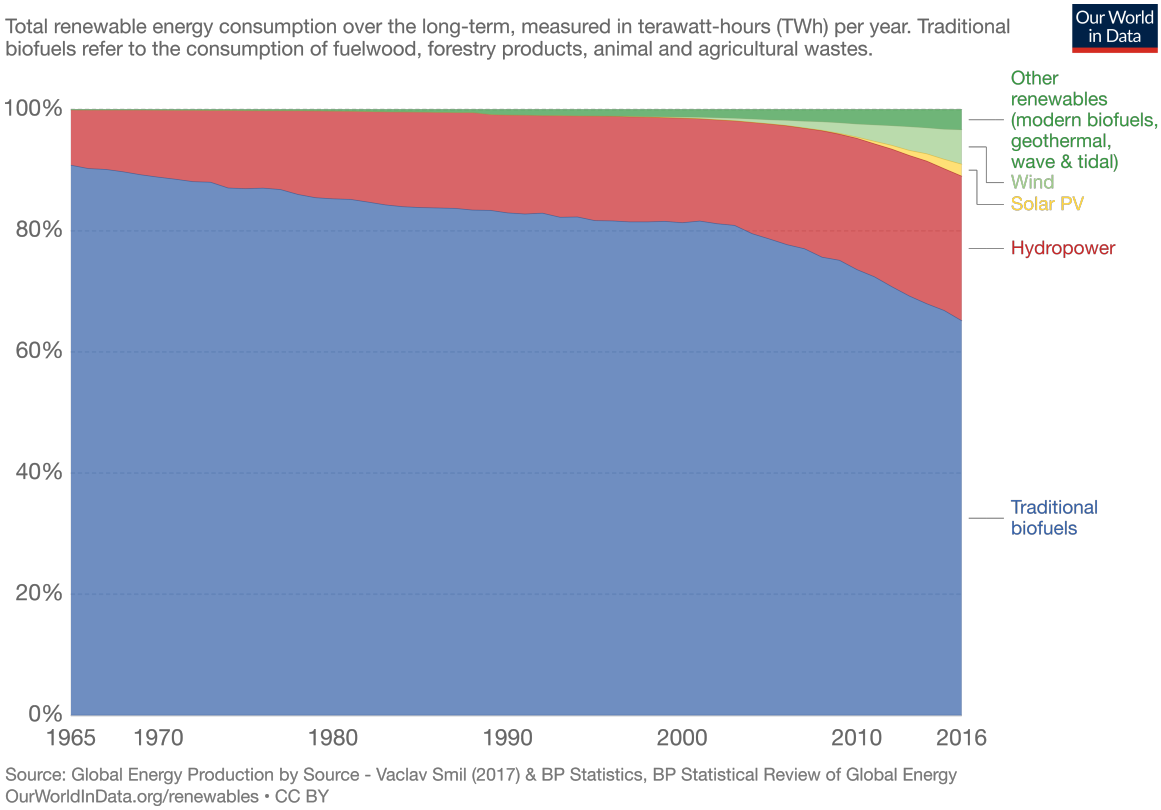


Figure 1.1: Global renewable energy consumption, terawatt-hours. [Courtesy of Our World in Data]

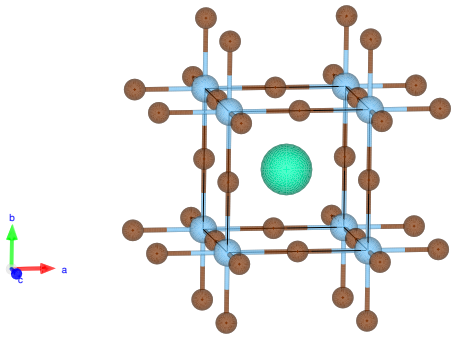

Figure 1.2: The crystal structure of $CaTiO_3$: Ca atom is coloured green, Ti atom is coloured in blue and O atom is coloured in brown.

low usage of silicon photovoltaics. To improve these drawbacks of the traditional solar cell, there are several emerging photovoltaic materials, such as the dye-sensitized solar cell[36], the quantum dot solar cell[20], the organic solar cell[18], etc. Among these emerging technologies, hybrid halide perovskite[24] solar cells demonstrate the most potential to change the quota of world energy consumption.

## 1.2 Hybrid halide perovskite photovoltaics

### 1.2.1 Emerging of perovskite photovoltaics and its development

In 1839, a German mineralogist named Gustav Rose discovered the perovskite structure $CaTiO_3$ in the Ural Mountains. The crystal structure is shown in Fig. 1.2. The general formula of this compound is $ABX_3$. Ca atom occupies the body center (A site) of perovskite structure, Ti atoms are located at each corner (B site), and O atoms stay in the middle of each bond (X site). The ion radius on A site is usually larger than the one on B site. The unit cell of an ideal perovskite structure consists of corner-sharing $BX_6$ octahedra and A is occupied cuboctahedral in the center. Over a century later of finding the natural perovskite $CaTiO_3$, Weber[44] first synthesized hybrid halide perovskite in 1978. The crystal structures of hybrid halide organic-inorganic perovskite are originated from the mineral $CaTiO_3$. A

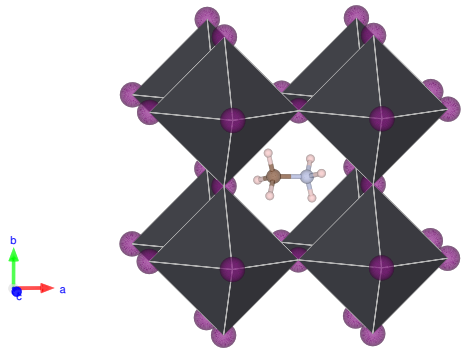


Figure 1.3: The crystal structure of $CH_3NH_3PbI_3$: C atom is coloured brown, N atom is coloured cyan, H atom is coloured light pink, Pb atom is in the center of the octahedral surrounded by purple I atom.

large monovalent organic methylammonium ($CH_3NH_3$) cation was located at the A site, a lead atom possesses B site of the structure and halide atoms are located at the X sites between two adjacent lead atoms. The structure is illustrated in Fig. 1.3. Early research of the hybrid perovskites was focused on the potential of superconductor[31], carrier transport as semiconducting channels[21], etc. Until 2009, the first hybrid halide perovskite solar cell was fabricated as a form of dye-sensitized solar cell with a power conversion efficiency (PCE) of 3.81% by Tsutomu Miyasaka[24]. Tsutomu Miyasaka used hybrid halide perovskite as the dye absorbed on mesoscopic $TiO_2$. However, the first version of the perovskite solar cell was quite unstable. The halide electrolyte will erode the perovskite active layer within a few minutes. A breakthrough came three years later: instead of iodine/iodide redox electrolyte, using a solid-state spiro-OMeTAD as the hole transporter largely increases the stability of hybrid halide perovskite solar cell with a PCE larger than 9%[22,26]. In 2013, Burschka et al.[7] utilized a novel sequential deposition method and made a planar cell structure rather than the previous mesoporous scaffold perovskite, with a PCE about 15%. Introducing another promising formamidinium cation into current methylammonium lead halide perovskite improved the crystallization properties of the perovskite thin film and boosted the PCE to 20.2%. In 2016, Saliba et al.[41] obtained a more stable perovskite solar

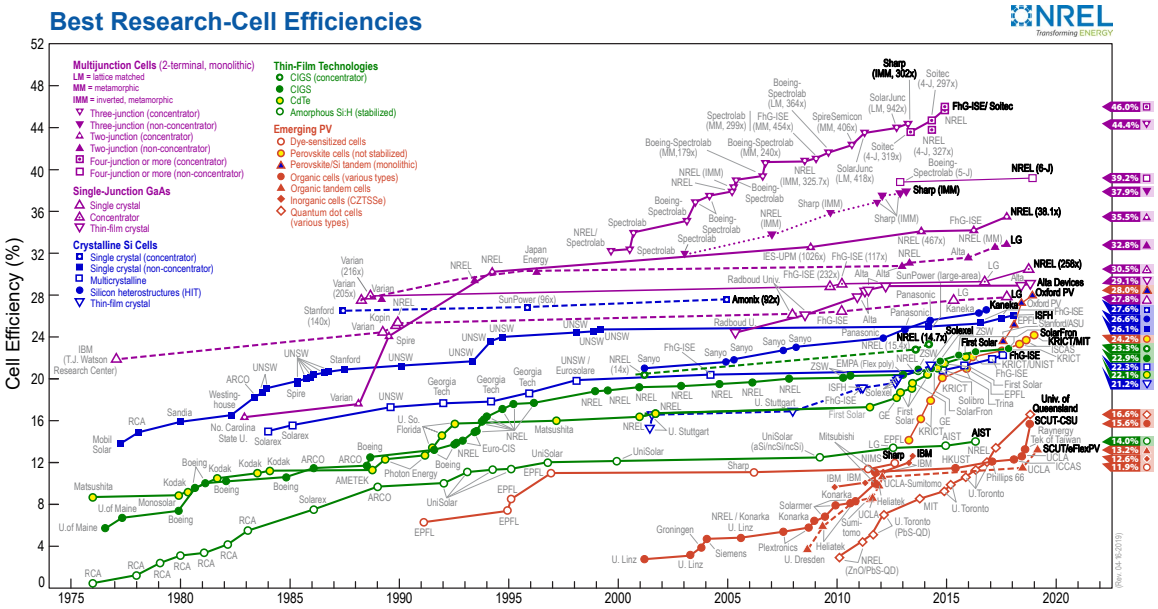


Figure 1.4: 2019 Best Research-Cell Efficiencies chart from the National Renewable Energy Laboratory[1]

cell when adding a third type of cation Cs into the perovskite alloy with a PCE of 21.1%. The best research-cell efficiencies chart from the National Renewable Energy Laboratory records the development of different photovoltaic technologieshave from 1975 to nowadays, shown in Fig. 1.4. The chart clearly shows that the dramatic increase of PCE for perovskite-based photovoltaics compared with other emerging photovoltaic technologies. It is certified that the latest world record PCE of perovskite photovoltaics has roared up to 25.2% which have already competed for the thin-film polycrystalline silicon photovoltaics(21.2%)[1]. Except for the high PCE of perovskite solar cells, the intrinsic softness of hybrid halide perovskite[32] makes the procedure of cell module fabrication printable[30,39]. These printable technologies will largely diminish the drawbacks mentioned previously of traditional solar cells.

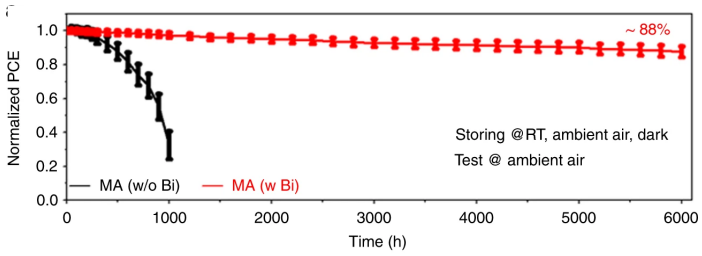


Figure 1.5: Adding a bismuth layer to repel stimuli which potentially degrade $CH_3NH_3PbI_3$[46]. With permission requested from Nature Communications.

### 1.2.2 Problems to overcome

Although the hybrid halide perovskite solar cells possess a lot of unique advantages compared with the traditional solar cells even along with the emerging of the printable technology, there still exist a few issues to address which hinder the commercialization of this technology. Among these issues, the long-term instability of hybrid halide perovskite is the main concern.

Plenty of methods have been proposed to stabilize hybrid halide perovskites. In 2019, Wu et al.[46] proposed that adding a chemically inert bismuth interlayer will largely improve the stability of perovskite photovoltaic devices. And this protective Bi-based film will keep 88% of its initial PCE after 250 days when stored in ambient air in the dark without any encapsulation, shown in Fig. 1.5. The cost of perovskite module is less than 50% of the cost of silicon techonology[10]. Whereas, successfully commercialized solar cells should meet an essential condition which is to work stably as long as 25 years. One-year lifetime for perovskite photovoltaics questions the practical cost of perovskite photovoltaics[15]. It still has a long way to go. To be specific, the hybrid halide perovskite solar cells will degrade under humidity, heat, light and even oxygen[6,12,28,38]. From the first–principles prediction, the hybrid halide perovskite $CH_3NH_3PbI_3$ is thermodynamically unstable[49]. As a result, room–temperature tetragonal $CH_3NH_3PbI_3$ phase will separate into two different phases: $CH_3NH_3I$ and $PbI_2$. It means that hybrid halide perovskites are unstable even

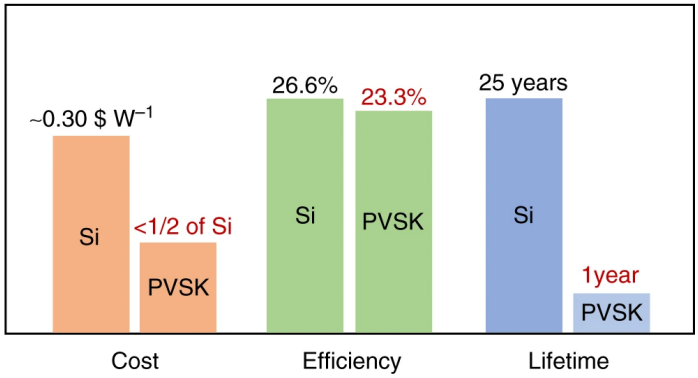


Figure 1.6: Compared with silicon techonoly, 1 year lifetime for perovskite photovoltaics hinders its commercialization[15]. With permission requested from Nature Communications.

without contacting water, oxygen, and light. It is soon experimentally proved that this type of perovskite is intrinsically unstable. At 85° which is assumed as the photovoltaics operation temperature on a roof on a hot summer day according to International Standards (IEC 61646 climatic chamber tests), it is proved that the crystal structure of $CH_3NH_3PbI_3$ decomposes into $PbI_2$ and $CH_3NH_3I$ without invasion of any water, oxygen, and light[11]. As discussed above, encapsulation cannot stabilize the hybrid halide perovskites as long as 25 years. Thermodynamical instability will finally break down the perovskites within a short period. To commercialize hybrid halide perovskite solar cells, it is important to develop the alternative hybrid halide perovskite materials which possess comparable properties for photovoltaics and have to be intrinsic stable.

Another problem is that lead ions ($Pb^{2+}$) are poisonous for lives. It can cause damage to brains, internal organs and bones. Air, water, soil, food can be contaminated by lead. Unfortunately, lead in hybrid halide perovskite plays an important role in these excellent properties. Early investigations on electronic properties of hybrid halide perovskites indicate that lead and halide atoms make a great contribution to the optimum band gaps for photovoltaics[13,43,48]. Lead-free hybrid halide perovskite solar cells seem to be promising. $CH_3NH_3SnI_3$ based perovskite solar cells were reported with the highest efficiency exceeding 6%[19,35]. $NH_2CH{=}NH_2$ is slightly larger than $CH_3NH_3$, replacement of $CH_3NH_3$

with $NH_2CH{=}NH_2$ will generate a even more suitable band gap (1.43 eV) material for photovoltaics[37]. A year later, $NH_2CH{=}NH_2SnI_3$ perovskite solar cells were reported with efficiency around 5%[23,27]. However, under ambient environment, $Sn^{2+}$ ion will be easily oxidized, and transfer to $Sn^{4+}$ ion with higher oxidation state which breaks the charge neutrality and the Sn–based perovskites decompose[35].

In this thesis, we focus on the instability of hybrid halide perovskites from the first principle sides. The project expands as in the following order. Firstly, characterize the instability through density functional theory calculation combined with experimental data. Secondly, decompose the close-to-zero reaction enthalpy, and get a deeper understanding of the instability. Then, trying to find a perovskite structure with good stability as well as promising photovoltaic properties. However, we focus on the stability defined by phase separation, we neglect the instability of the proposed three-membered ring cation.

At last, water degrades hybrid halide perovskite immediately[17]. Two extreme water content conditions have to be considered: atmospheric moisture and liquid water. Both of the mechanisms are important. For fresh perovskite photovoltaics, moisture degradation is important for endurance. There are many publications investigating the moisture–induced degradation of $CH_3NH_3PbI_3$[5,14,25,29,40,42,45,47]. However, since it is photovoltaics, we have to imagine different situations it will encounter, e.g. after a couple of years, cracks appearing on the modules are inevitable, at this stage understanding the liquid water degradation mechanism becomes important.

However, there are fewer publications about liquid water degradation pathway[8,9,34]. It is still unclear about the mechanism of $CH_3NH_3PbI_3$ degradation in liquid water, such as the energy barrier, decomposition details. To investigate this unknown area, using *ab initio* metadynamics to find the energy barrier for the initial dissolution, and using density functional theory combined with thermodynamic data, we explain the mechanisms for $CH_3NH_3PbI_3$ and $CsPbI_3$ dissolution in water.

# Bibliography

[1] Best research-cell efficiency chart. https://www.nrel.gov/pv/cell-efficiency.html. Accessed: 2019-10-01.

[2] Solar power. https://en.wikipedia.org/wiki/Solar_power#Self_consumption, . Accessed: 2019-10-01.

[3] Solar power consumption. https://en.wikipedia.org/wiki/Solar_thermal_energy, . Accessed: 2019-10-02.

[4] N. Abumhadi, E. Todorovska, B. Assenov, S. Tsonev, D. Vulcheva, D. Vulchev, L. Atanasova, S. Sanova, and A. Atanassov. Agricultural research in 21st century: Challenges facing the food security under the impacts of climate change. *Bulg. J. Agric. Sci.*, 18(6):801–818, 2012.

[5] N. Aristidou, C. Eames, M. S. Islam, and S. A. Haque. Insights into the increased degradation rate of $CH_3NH_3PbI_3$ solar cells in combined water and $O_2$ environments. *J. Mater. Chem. A*, 5(48):25469–25475, 2017. doi: 10.1039/c7ta06841g.

[6] T. A. Berhe, W.-N. Su, C.-H. Chen, C.-J. Pan, J.-H. Cheng, H.-M. Chen, M.-C. Tsai, L.-Y. Chen, A. A. Dubale, and B.-J. Hwang. Organometal halide perovskite solar cells: Degradation and stability. *Energy Environ. Sci.*, 9(2):323–356, 2016. doi: 10.1039/C5EE02733K.

[7] J. Burschka, N. Pellet, S.-J. Moon, R. Humphry-Baker, P. Gao, M. K. Nazeeruddin, and M. Grätzel. Sequential deposition as a route to high-performance perovskite-sensitized solar cells. *Nature*, 499(7458):316–319, 2013. doi: 10.1038/nature12340.

[8] C. Caddeo, M. I. Saba, S. Meloni, A. Filippetti, and A. Mattoni. Collective molecular mechanisms in the $CH_3NH_3PbI_3$ dissolution by liquid water. *ACS Nano*, 11(9):9183–9190, Aug. 2017. doi: 10.1021/acsnano.7b04116.

[9] C. Caddeo, D. Marongiu, S. Meloni, A. Filippetti, F. Quochi, M. Saba, and A. Mattoni. Hydrophilicity and water contact angle on methylammonium lead iodide. *Adv. Mater. Interfaces*, page 1801173, Dec. 2018. doi: 10.1002/admi.201801173.

[10] M. Cai, Y. Wu, H. Chen, X. Yang, Y. Qiang, and L. Han. Cost-performance analysis of perovskite solar modules. *Adv. Sci.*, 4(1):1600269, 2017. doi: 10.1002/advs.201600269.

[11] B. Conings, J. Drijkoningen, N. Gauquelin, A. Babayigit, J. D'Haen, L. D'Olieslaeger, A. Ethirajan, J. Verbeeck, J. Manca, E. Mosconi, et al. Intrinsic thermal instability of methylammonium lead trihalide perovskite. *Adv. Energy Mater.*, 5(15):1500477, 2015. doi: 10.1002/aenm.201500477.

[12] P. Docampo and T. Bein. A long-term view on perovskite optoelectronics. *Acc. Chem. Res.*, 49(2):339–346, 2016. doi: 10.1021/acs.accounts.5b00465.

[13] J. Even, L. Pedesseau, J.-M. Jancu, and C. Katan. Importance of spin–orbit coupling in hybrid organic/inorganic perovskites for photovoltaic applications. *J. Phys. Chem. Lett.*, 4(17):2999–3005, 2013. doi: 10.1021/jz401532q.

[14] J. M. Frost, K. T. Butler, F. Brivio, C. H. Hendon, M. van Schilfgaarde, and A. Walsh. Atomistic origins of high-performance in hybrid halide perovskite solar cells. *Nano Lett.*, 14(5):2584–2590, Apr. 2014. doi: 10.1021/nl500390f.

[15] P. Gao, A. R. B. M. Yusoff, and M. K. Nazeeruddin. Dimensionality engineering of hybrid halide perovskite light absorbers. *Nat. Commun.*, 9(1):5028, Nov. 2018. doi: 10.1038/s41467-018-07382-9.

[16] J. Goldemberg. *World Energy Assessment: Energy and the challenge of sustainability.* United Nations Pubns, 2000.

[17] B. Hailegnaw, S. Kirmayer, E. Edri, G. Hodes, and D. Cahen. Rain on methylammonium lead iodide based perovskites: Possible environmental effects of perovskite

solar cells. *J. Phys. Chem. Lett.*, 6(9):1543–1547, Apr. 2015. doi: 10.1021/acs.jpclett.5b00504.

[18] J. J. Halls, K. Pichler, R. H. Friend, S. Moratti, and A. Holmes. Exciton diffusion and dissociation in a poly (p-phenylenevinylene)/$C_{60}$ heterojunction photovoltaic cell. *Appl. Phys. Lett.*, 68(22):3120–3122, 1996. doi: 10.1063/1.115797.

[19] F. Hao, C. C. Stoumpos, D. H. Cao, R. P. Chang, and M. G. Kanatzidis. Lead-free solid-state organic-inorganic halide perovskite solar cells. *Nat. Photonics*, 8(6):489–494, 2014. doi: 10.1038/nphoton.2014.82.

[20] A. H. Ip, S. M. Thon, S. Hoogland, O. Voznyy, D. Zhitomirsky, R. Debnath, L. Levina, L. R. Rollny, G. H. Carey, A. Fischer, et al. Hybrid passivated colloidal quantum dot solids. *Nat. Nanotechnol.*, 7(9):577–582, 2012. doi: 10.1038/nnano.2012.127.

[21] C. R. Kagan. Organic-inorganic hybrid materials as semiconducting channels in thin-film field-effect transistors. *Science*, 286(5441):945–947, Oct. 1999. doi: 10.1126/science.286.5441.945.

[22] H.-S. Kim, C.-R. Lee, J.-H. Im, K.-B. Lee, T. Moehl, A. Marchioro, S.-J. Moon, R. Humphry-Baker, J.-H. Yum, J. E. Moser, et al. Lead iodide perovskite sensitized all-solid-state submicron thin film mesoscopic solar cell with efficiency exceeding 9%. *Sci. Rep.*, 2:591, 2012. doi: 10.1038/srep00591.

[23] T. M. Koh, T. Krishnamoorthy, N. Yantara, C. Shi, W. L. Leong, P. P. Boix, A. C. Grimsdale, S. G. Mhaisalkar, and N. Mathews. Formamidinium tin-based perovskite with low Eg for photovoltaic applications. *J. Mater. Chem. A*, 3(29):14996–15000, 2015. doi: 10.1039/C5TA00190K.

[24] A. Kojima, K. Teshima, Y. Shirai, and T. Miyasaka. Organometal halide perovskites as

visible-light sensitizers for photovoltaic cells. *J. Am. Chem. Soc.*, 131(17):6050–6051, 2009. doi: 10.1021/ja809598r.

[25] F. U. Kosasih and C. Ducati. Characterising degradation of perovskite solar cells through *In-Situ* and operando electron microscopy. *Nano Energy*, 47:243–256, May 2018. doi: 10.1016/j.nanoen.2018.02.055.

[26] M. M. Lee, J. Teuscher, T. Miyasaka, T. N. Murakami, and H. J. Snaith. Efficient hybrid solar cells based on meso-superstructured organometal halide perovskites. *Science*, 338(6107):643–647, 2012. doi: 10.1126/science.1228604.

[27] S. J. Lee, S. S. Shin, Y. C. Kim, D. Kim, T. K. Ahn, J. H. Noh, J. Seo, and S. I. Seok. Fabrication of efficient formamidinium tin iodide perovskite solar cells through $SnF_2$–pyrazine complex. *J. Am. Chem. Soc.*, 138(12):3974–3977, 2016. doi: 10.1021/jacs.6b00142.

[28] T. Leijtens, G. E. Eperon, N. K. Noel, S. N. Habisreutinger, A. Petrozza, and H. J. Snaith. Stability of metal halide perovskite solar cells. *Adv. Energy Mater.*, 5(20):1500963, 2015. doi: 10.1002/aenm.201500963.

[29] J. A. McLeod and L. Liu. Prospects for mitigating intrinsic organic decomposition in methylammonium lead triiodide perovskite. *J. Phys. Chem. Lett.*, 9(9):2411–2417, Apr. 2018. doi: 10.1021/acs.jpclett.8b00323.

[30] A. Mei, X. Li, L. Liu, Z. Ku, T. Liu, Y. Rong, M. Xu, M. Hu, J. Chen, Y. Yang, M. Gratzel, and H. Han. A hole-conductor-free, fully printable mesoscopic perovskite solar cell with high stability. *Science*, 345(6194):295–298, July 2014. doi: 10.1126/science.1254763.

[31] D. B. Mitzi, S. Wang, C. A. Feild, C. A. Chess, and A. M. Guloy. Conducting layered organic-inorganic halides containing (110)-oriented perovskite sheets. *Science*, 267 (5203):1473–1476, Mar. 1995. doi: 10.1126/science.267.5203.1473.

[32] K. Miyata, T. L. Atallah, and X.-Y. Zhu. Lead halide perovskites: Crystal-liquid duality, phonon glass electron crystals, and large polaron formation. *Sci. Adv.*, 3(10): e1701469, Oct. 2017. doi: 10.1126/sciadv.1701469.

[33] O. Morton. Solar energy: A new day dawning?: Silicon valley sunrise. *Nature*, 443 (7107):19–22, 2006. doi: 10.1038/443019a.

[34] E. Mosconi, J. M. Azpiroz, and F. D. Angelis. *Ab Initio* molecular dynamics simulations of methylammonium lead iodide perovskite degradation by water. *Chem. Mater.*, 27 (13):4885–4892, July 2015. doi: 10.1021/acs.chemmater.5b01991.

[35] N. K. Noel, S. D. Stranks, A. Abate, C. Wehrenfennig, S. Guarnera, A.-A. Haghighirad, A. Sadhanala, G. E. Eperon, S. K. Pathak, M. B. Johnston, et al. Lead-free organic–inorganic tin halide perovskites for photovoltaic applications. *Energy Environ. Sci.*, 7 (9):3061–3068, 2014. doi: 10.1039/C4EE01076K.

[36] B. O'regan and M. Grätzel. A low-cost, high-efficiency solar cell based on dye-sensitized colloidal $TiO_2$ films. *Nature*, 353(6346):737–740, 1991. doi: 10.1038/353737a0.

[37] S. Pang, H. Hu, J. Zhang, S. Lv, Y. Yu, F. Wei, T. Qin, H. Xu, Z. Liu, and G. Cui. $NH_2CH{=}NH_2PbI_3$: An alternative organolead iodide perovskite sensitizer for mesoscopic solar cells. *Chem. Mater.*, 26(3):1485–1491, 2014. doi: 10.1021/cm404006p.

[38] Y. Rong, L. Liu, A. Mei, X. Li, and H. Han. Beyond efficiency: The challenge of stability in mesoscopic perovskite solar cells. *Adv. Energy Mater.*, 5(20):1501066, 2015. doi: 10.1002/aenm.201501066.

[39] Y. Rong, Y. Hu, A. Mei, H. Tan, M. I. Saidaminov, S. I. Seok, M. D. McGehee, E. H. Sargent, and H. Han. Challenges for commercializing perovskite solar cells. *Science*, 361(6408):eaat8235, Sept. 2018. doi: 10.1126/science.aat8235.

[40] M. I. Saidaminov, J. Kim, A. Jain, R. Quintero-Bermudez, H. Tan, G. Long, F. Tan, A. Johnston, Y. Zhao, O. Voznyy, and E. H. Sargent. Suppression of atomic vacancies via incorporation of isovalent small ions to increase the stability of halide perovskite solar cells in ambient air. *Nat. Energy*, 3(8):648–654, July 2018. doi: 10.1038/s41560-018-0192-2.

[41] M. Saliba, T. Matsui, J.-Y. Seo, K. Domanski, J.-P. Correa-Baena, M. K. Nazeeruddin, S. M. Zakeeruddin, W. Tress, A. Abate, A. Hagfeldt, et al. Caesium-containing triple cation perovskite solar cells: Improved stability, reproducibility and high efficiency. *Energy Environ. Sci.*, 9(6):1989–1997, 2016. doi: 10.1039/C5EE03874J.

[42] E. Smecca, Y. Numata, I. Deretzis, G. Pellegrino, S. Boninelli, T. Miyasaka, A. L. Magna, and A. Alberti. Stability of solution-processed $MAPbI_3$ and $FAPbI_3$ layers. *Phys. Chem. Chem. Phys.*, 18(19):13413–13422, 2016. doi: 10.1039/c6cp00721j.

[43] P. Umari, E. Mosconi, and F. De Angelis. Relativistic GW calculations on $CH_3NH_3PbI_3$ and $CH_3NH_3SnI_3$ perovskites for solar cell applications. *Sci. Rep.*, 4:4467, 2014. doi: 10.1038/srep04467.

[44] D. Weber. $CH_3NH_3PbX_3$, ein pb (II)-system mit kubischer perowskitstruktur/$CH_3NH_3PbX_3$, a pb (II)-system with cubic perovskite structure. *Z. Naturforsch. B Chem. Sci.*, 33(12):1443–1445, 1978. doi: 10.1515/znb-1978-1214.

[45] W. Wei and Y. H. Hu. Catalytic role of $H_2O$ in degradation of inorganic-organic perovskite ($CH_3NH_3PbI_3$) in air. *Int. J. Energy Res.*, 41(7):1063–1069, Nov. 2016. doi: 10.1002/er.3680.

[46] S. Wu, R. Chen, S. Zhang, B. H. Babu, Y. Yue, H. Zhu, Z. Yang, C. Chen, W. Chen, Y. Huang, S. Fang, T. Liu, L. Han, and W. Chen. A chemically inert bismuth interlayer enhances long-term stability of inverted perovskite solar cells. *Nat. Commun.*, 10(1): 1161, Mar. 2019. doi: 10.1038/s41467-019-09167-0.

[47] J. Yang, Z. Yuan, X. Liu, S. Braun, Y. Li, J. Tang, F. Gao, C. Duan, M. Fahlman, and Q. Bao. Oxygen- and water-induced energetics degradation in organometal halide perovskites. *ACS Appl. Mater. Interfaces*, 10(18):16225–16230, Apr. 2018. doi: 10.1021/acsami.8b04182.

[48] W.-J. Yin, T. Shi, and Y. Yan. Unusual defect physics in $CH_3NH_3PbI_3$ perovskite solar cell absorber. *Appl. Phys. Lett.*, 104(6):063903, Feb. 2014. doi: 10.1063/1.4864778.

[49] Y.-Y. Zhang, S. Chen, P. Xu, H. Xiang, X.-G. Gong, A. Walsh, and S.-H. Wei. Intrinsic instability of the hybrid halide perovskite semiconductor $CH_3NH_3PbI_3$. *Chin. Phys. Lett.*, 35(3):036104, 2018. doi: 10.1088/0256-307X/35/3/036104.

# Chapter 2

# Computational method

Density functional theory (DFT) is a computational modelling method based on quantum mechanics. From quantum mechanics, the wave function of a given system can tell all the information about the system. In order to find the wave function of a specific system, it is necessary to solve the Schrödinger equations. DFT is such a method that offers an approximate solution to the Schrödinger equations of an interested system. This Chapter discussed the theory and background of the simulation method used in the thesis.

## 2.1 The Schrödinger equation

The Schrödinger equation helps us to describe the properties of a system which consists of many atoms. One simple form of the Schrödinger equation is listed below:

$$H\Psi = E\Psi \tag{2.1.1}$$

It is the time independent, nonrelativistic Schrödinger equation. In the equation, Hamiltonian $H$ is the total energy operator for a system. $\Psi$ is the set of solutions, or eigenstates of the Hamiltonian. When input specific solutions $\Psi_n$ into the Schrödinger equation, it will

generate the corresponding eigenvalue $E_n$ which is a real number. It will be complicated when many electrons and nuclei exist in a system. In detail, $H$ explicitly describes the Coulombic electrostatic interactions between the quantum particles of the system.

$$H(\mathbf{R},\mathbf{r}) = T_{\mathrm{e}}(\mathbf{r}) + T_{\mathrm{n}}(\mathbf{R}) + U_{\mathrm{ee}}(\mathbf{r}) + U_{\mathrm{nn}}(\mathbf{R}) + U_{\mathrm{en}}(\mathbf{R},\ \mathbf{r}) \tag{2.1.2}$$

In Eq. (2.1.2), the first term on the right side is the kinetic energy operator of the electrons which can be described in detail:

$$T_{\mathrm{e}}(\mathbf{r}) = -\sum_i \frac{\hbar}{2m_{\mathrm{e}}}\nabla_i^2, \tag{2.1.3}$$

where $\mathbf{r}$ is the coordinates of electrons, $\hbar$ is the Planck's constant. $m_{\mathrm{e}}$ is mass of an electron, and $i$ indicates $i$-th electron. The second term on the right side gives the kinetic energy operator of the nuclei,

$$T_{\mathrm{n}}(\mathbf{R}) = -\sum_I \frac{\hbar}{2M_I}\nabla_I^2, \tag{2.1.4}$$

where $\mathbf{R}$ is the coordinates of nuclei, $M_{\mathrm{I}}$ is the mass of $I$-th nucleus. The third term describes the Coulombic interaction between electrons,

$$U_{\mathrm{ee}}(\mathbf{r}) = \frac{1}{2}\sum_{i\neq j}\frac{e^2}{4\pi\epsilon_0}\frac{1}{|\mathbf{r}_i - \mathbf{r}_j|}, \tag{2.1.5}$$

where $\epsilon_0$ is the permittivity of vacuum. The forth term indicates the Coulombic interaction between nuclei,

$$U_{\mathrm{nn}}(\mathbf{R}) = \frac{1}{2}\sum_{I\neq J}\frac{e^2}{4\pi\epsilon_0}\frac{Z_I Z_J}{|\mathbf{R}_I - \mathbf{R}_J|}, \tag{2.1.6}$$

where $Z$ is the charge of nucleus. The last term renders the Coulombic interaction between each electron with each nucleus,

$$U_{\text{en}}(\mathbf{R},\ \mathbf{r}) = -\frac{1}{2}\sum_{i,I}\frac{e^2}{4\pi\epsilon_0}\frac{Z_I}{|\mathbf{r}_i - \mathbf{R}_I|}. \tag{2.1.7}$$

Combine each term of the explicit $H$ (Eq. (2.1.3)–Eq. (2.1.7)) into Eq. (2.1.1), a more complicated *many-body Schrödinger equation* comes:

$$\begin{aligned}[-\sum_i \frac{\hbar}{2m_e}\nabla_i^2 - \sum_I \frac{\hbar}{2M_I}\nabla_I^2 + \frac{1}{2}\sum_{i\neq j}\frac{e^2}{4\pi\epsilon_0}\frac{1}{|\mathbf{r}_i - \mathbf{r}_j|} \\ + \frac{1}{2}\sum_{I\neq J}\frac{e^2}{4\pi\epsilon_0}\frac{Z_I Z_J}{|\mathbf{R}_I - \mathbf{R}_J|} - \frac{1}{2}\sum_{i,I}\frac{e^2}{4\pi\epsilon_0}\frac{Z_I}{|\mathbf{r}_i - \mathbf{R}_I|}]\Psi = E_{\text{tot}}\Psi\end{aligned} \tag{2.1.8}$$

To solve this *many-body Schrödinger equation* for a real material is too complicated. Several approximations are utilized to simplify this equation.

## 2.2 Hartree-Fock equations

From quantum mechanics, we know that nuclei are much heavier than electrons (more than 1800 times). That means when there exists external field, electrons must react much faster than nuclei. As a result, it is possible and easy to treat nuclei and electrons separately. This separation of nuclei and electrons can be realized by the *Oppenheimer approximation*. Therefore, it is considered that $M_I = \infty$. The kinetic energy of nuclei are disppeared:

$$\left[-\sum_i \frac{\hbar}{2m_e}\nabla_i^2 + \frac{1}{2}\sum_{i\neq j}\frac{e^2}{4\pi\epsilon_0}\frac{1}{|\mathbf{r}_i - \mathbf{r}_j|} - \frac{1}{2}\sum_{i,I}\frac{e^2}{4\pi\epsilon_0}\frac{Z_I}{|\mathbf{r}_i - \mathbf{R}_I|}\right]\Psi = E\Psi \tag{2.2.1}$$

Due to the immobile nuclei, the Coulombic interactions between nuclei become constants which are moved to right-hand side. In Eq. (2.2.1), $E$ captures the total energy of all the

electrons in the system

$$E = E_{\text{tot}} - \frac{1}{2}\sum_{I\neq J}\frac{e^2}{4\pi\epsilon_0}\frac{Z_I Z_J}{|\mathbf{R}_I - \mathbf{R}_J|}, \tag{2.2.2}$$

since coordinates of nuclei which are external parameters are regarded as constants.

However, the second term in Eq. (2.2.1) the Coulombic interaction between electrons requires the coordinates of each electron which cannot be measured. Instead of this electron-electron interaction, an average electrostatic potential generated by electrons is employed to simplify this interaction. Before iterating this average electrostatic potential, we first introduce a quantity which can be measured. Note that the wave function of any specific electron is impossible to be observed. At particular set of coordinates, $\mathbf{r}_1, \mathbf{r}_2, \ldots, \mathbf{r}_N$, the appearance probability of a single electron can be measured. This probability can be described as $\Psi^*(\mathbf{r}_1, \ldots, \mathbf{r}_N)\Psi(\mathbf{r}_1, \ldots, \mathbf{r}_N)$. The summation of the probability is the density of electrons $n(\mathbf{r})$ at a particular position.

$$n(\boldsymbol{r}) = 2\sum_i \Psi_i^*(\mathbf{r})\Psi_i(\mathbf{r}) \tag{2.2.3}$$

Through Poisson's equation, $n(\mathbf{r})$ will generate an electrostatic potential which is mentioned average electrostatic potential. $V_{\text{H}}$ is Hartree potential,

$$\nabla V_{\text{H}}(\mathbf{r}) = -4\pi n(\mathbf{r}) \tag{2.2.4}$$

Further, the Hartree potential is shown in

$$V_{\text{H}}(\mathbf{r}) = \int d\mathbf{r}' \frac{n(\mathbf{r}')}{|\mathbf{r} - \mathbf{r}'|}. \tag{2.2.5}$$

Based on Eq. (2.2.5), the Hartree energy can be obtained

$$U_{\text{H}}(\mathbf{r}) = \frac{1}{2}\int\int \frac{e^2}{4\pi\epsilon_0} d\mathbf{r} d\mathbf{r}' \frac{n(\mathbf{r})n(\mathbf{r}')}{|\mathbf{r} - \mathbf{r}'|}. \tag{2.2.6}$$

Here, the Hartree product is introduced based on an approximation which assumes the electrons are independant with each other.

$$\Psi = \phi_1(\mathbf{r}_1)\phi_2(\mathbf{r}_2)\cdots\phi_N(\mathbf{r}_N), \tag{2.2.7}$$

where $\phi_1(\mathbf{r}_1)$ is the single electron wavefunction. Corresponding energy on the right side becomes

$$E = \varepsilon_1 + \varepsilon_2 \cdots + \varepsilon_{\mathrm{N}}. \tag{2.2.8}$$

Now, incorporate Eq. (2.2.5) and Eq. (2.2.7) into Eq. (2.2.1), and write the resultant equation in the form of single-electron wavefunction equations

$$\left[-\frac{\hbar}{2m_e}\nabla_i^2 - \frac{1}{2}\frac{e^2}{4\pi\epsilon_0}\frac{Z_I}{|\mathbf{r}_i - \mathbf{R}_I|} + \int d\mathbf{r}'\frac{n(\mathbf{r}')}{|\mathbf{r} - \mathbf{r}'|}\right]\phi_i = \varepsilon_i\phi_i \tag{2.2.9}$$

Here, Pauli exclusion principle is realized by using the Slater determinant

$$\frac{\delta E}{\delta \phi_i^*} = 0, \tag{2.2.10}$$

$$\int d\mathbf{r}\phi_i^*(\mathbf{r}) = \delta_{ij} \tag{2.2.11}$$

Incorporate this extra term into Eq. (2.2.9), we can obtain the *Hartree-Fock equations*

$$\left[-\frac{\hbar}{2m_e}\nabla_i^2 - \frac{1}{2}\frac{e^2}{4\pi\epsilon_0}\frac{Z_I}{|\mathbf{r}_i - \mathbf{R}_I|} + \int d\mathbf{r}'\frac{n(\mathbf{r}')}{|\mathbf{r} - \mathbf{r}'|}\right]\phi_i - \frac{e^2}{4\pi\varepsilon_0}\sum_{j=1}^{N}\int d\mathbf{r}'\frac{\phi_j(\mathbf{r}')^*\phi_i(\mathbf{r}')\phi_j(\mathrm{r})}{|\mathbf{r} - \mathbf{r}'|}\delta_{\sigma_i}\delta_{\sigma_j} = \varepsilon_i\phi_i \tag{2.2.12}$$

Similar as previously mentioned, the first term on the left side of Eq. (2.2.12) is the kinetic energy of $i$-th electron; the second term gives the Coulombic interaction of $i$-th electron and

$I$-th nucleus; the third term approximates electron-electron interaction as an average electrostatic field $V_{\mathrm{H}}$ which includes self-interaction. However, to eleminate the self-interaction introduced from the third term, the forth term is introduced

$$V_x(\mathbf{r},\mathbf{r}') = -\sum_j \frac{\phi_j^*(\mathbf{r}')\phi_j(\mathbf{r})}{|\mathbf{r}-\mathbf{r}'|}, \tag{2.2.13}$$

this $V_x$ is named Fock exchange potential. This additional potential increases the accuracy from *independant electron approximation* in Eq. (2.2.12).

## 2.3 Kohn-Sham equations

The setting of *Hartree-Fock equations* can solve the Schrödinger equation and the solutions are improved by Fock exchange potential of Eq. (2.2.13). Whereas, the Slater determinant cannot capture the full Coulombic correlations of electrons. Here, another component is added to the current Hamiltonian. This additional term is $U_c$ which accounts for the rest correlations between electrons. Including all the components discussed before, it is obtained the *Kohn-Sham equations*

$$[\overbrace{T_{\mathrm{e}} + U_{\mathrm{en}} + U_{\mathrm{H}}}^{\text{known}} + \underbrace{E_{\mathrm{x}} + E_{\mathrm{c}}}_{\text{unknown}}]\phi_i(\mathbf{r}) = \varepsilon_i\phi_i(\mathbf{r}), \tag{2.3.1}$$

where $E_{\mathrm{x}}$ is exchange energy that can be obtained via Eq. (2.2.13). $E_{\mathrm{c}}$ is the correlation energy which account for the electron correlation not captured by Hartree Fock theory. Since from Eq. (2.1.1), the energy value can be obtained through

$$E = \langle\Psi|H|\Psi\rangle\,. \tag{2.3.2}$$

In Eq. (2.3.1), the kinetic energy, Coulombic interaction between electrons and nuclei and the Hartree potential are known, and combined with Eq. (2.3.2), the known energy $E_{\text{known}}$

$$E_{\text{known}} = \langle \Psi | U_{\text{en}} | \Psi \rangle + \langle \Psi | T_{\text{e}} + U_{\text{H}} | \Psi \rangle \,. \tag{2.3.3}$$

$E_{\text{known}}$ is the total energy under *independant electron approximation.* Kohn and Sham combine the unknown $E_{\text{x}}$ and $E_{\text{c}}$ together as a exchange-correlation term $E_{\text{xc}}$. The Hobenberg-Kohn theorem states that the total energy of electrons from a system at its ground state is a functional of the electron density. Hence, *Kohn-Sham equations*[2,4] can be expressed as below

$$E = -\frac{\hbar}{2m_e}\sum_i \int d(\mathbf{r})\phi_i^*(\mathbf{r})\nabla_i^2\phi_i(\mathbf{r}) - \frac{1}{2}\frac{e^2}{4\pi\epsilon_0}\int d(\mathbf{r})n(\mathbf{r})\frac{Z_I}{|\mathbf{r}_i - \mathbf{R}_I|} + \frac{1}{2}\frac{e^2}{4\pi\epsilon_0}\int\int d\mathbf{r}d\mathbf{r}'\frac{n(\mathbf{r})n(\mathbf{r}')}{|\mathbf{r}-\mathbf{r}'|} + E_{\text{xc}}[n(\mathbf{r})] \tag{2.3.4}$$

### 2.3.1 Exchange and correlation functional

In Kohn's Nobel Prize lecture[3], he talked about the exchange-correlation term:

"*The Kohn–Sham theory may be regarded as the formal exactification of Hartree theory. With the exact $E_{xc}$ and $V_{xc}$ all many-body effects are in principle included. Clearly this directs attention to the functional $E_{xc}[n]$. The practical usefulness of ground-state DFT depends entirely on whether approximations for the functional $E_{xc}[n]$ could be found, which are at the same time sufficiently simple and sufficiently accurate.*"

To solve the *Kohn–Sham equations*, the exchange–correlation function, $E_{\text{xc}}[\{\Psi_i\}]$, has to be specified. It is hard to find the specific $E_{\text{xc}}[\{\Psi_i\}]$. However, there is one way to derive the $E_{\text{xc}}[\{\Psi_i\}]$. The uniform electron gas which has constant electron density at all points, $n(\mathbf{r})$ = constant, provides a practical way to solve the *Kohn–Sham equations.* Set the known exchange–correlation potential from the uniform electron gas at the electron density

observed at that position instead of the exchange–correlation potential in the *Kohn–Sham equations*

$$V_{\mathrm{xc}}(\mathbf{r}) = V_{\mathrm{xc}}^{\text{electron gas}}[n(\mathbf{r})]. \tag{2.3.5}$$

This approximation is called *local density approximation* (LDA)[7]. It uses only the local density to estimate the exchange–correlation functional. Although the LDA is not the true exchange–correlation functional, it is important that the LDA completely defines the *Kohn–Sham equations*. Many different exchange–correlation functionals have been developed by researchers afterward. But there is still no perfectly defined exchange–correlation functional that can accurately solve the *Kohn–Sham equations* for systems with plenty numbers of atoms.

Compared with LDA, *generalized gradient approximation* (GGA) is an approach which contains more physical information than LDA. There are many distinct GGA functionals, for example, the Perdew–Wang functional (PW91)[5] and the Perdew–Burbe–Ernzerhof functional (PBE)[6] can predict accurate results for solid systems.

## 2.4 *Ab Initio* molecular dynamics

Instead of approximation of static nuclei from DFT, the movement of nuclei in *Ab Initio* molecular dynamics is considered. Compared with static calculations of DFT, *Ab Initio* molecular dynamics makes understanding dynamic structures possible. Specifically, the *Ab Initio* molecular dynamics can capture the bond breaking and forming during a chemical reaction. This advantage facilitates the progressing of Chapter 6.

### 2.4.1 Formalism of *Ab Initio* molecular dynamics

Different from previously discussed time-independent Schrödinger equation, *Ab Initio* molecular dynamics starts from time-dependent Schrödinger equation

$$H\Psi(t) = i\hbar\frac{\partial}{\partial t}\Psi(t) \tag{2.4.1}$$

Rewrite the Hamiltonian of Eq. (2.1.2) for a system

$$H(\mathbf{R},\mathbf{r}) = U_{\mathrm{nn}}(\mathbf{R}) + \overbrace{T_{\mathrm{e}}(\mathbf{r}) + T_{\mathrm{n}}(\mathbf{R}) + U_{\mathrm{ee}}(\mathbf{r}) + U_{\mathrm{en}}(\mathbf{R},\ \mathbf{r})}^{H_{\mathrm{e}}(\mathbf{R},\mathbf{r})} \tag{2.4.2}$$

Combine the $T_{\mathrm{e}}(\mathbf{r})$, $T_{\mathrm{n}}(\mathbf{R})$, $U_{\mathrm{ee}}(\mathbf{r})$, $U_{\mathrm{en}}(\mathbf{R},\ \mathbf{r})$ to a electronic Hamiltonian $H_{\mathrm{e}}(\mathbf{R},\mathbf{r})$. Split the wavefunction to individual wavefunctions generates,

$$\Psi(\mathbf{r},\mathbf{R},t) = \sum \phi_l(\mathbf{r},\mathbf{R})\chi_l(\mathbf{R},t), \tag{2.4.3}$$

where $\chi_l$ is regarded as the corresponding wavefunction of the nucleus. This expansion of the wavefunction is similar to Eq. (2.2.7). The difference between Eq. (2.2.7) and Eq. (2.4.3) is the latter time-dependent wavefunction of the nucleus is coupled with wavefunction of electrons. Combine Eq. (2.4.1) and Eq. (2.4.3), it is obtained the time-dependent Schrödinger equation for dynamic nuclei,

$$\left[-\sum_I \frac{\hbar^2}{2M_I}\nabla_I^2 + E_k(\mathbf{R}_I)\right]\chi_k + \sum_l \varsigma_{kl}\chi_l = i\hbar\frac{\partial}{\partial t}\chi_k \tag{2.4.4}$$

where $\varsigma_{kl}$ denotes a coupling operator which gives the degree of coupling between electron wavefunction and nuclear wavefunction.

Here, *Born-Oppenheimer approximation* is taken to simply Eq. (2.4.4): the electrons and nuclei are fully decoupled. Under this approximation, $\varsigma_{kl}$ disappears and Eq. (2.4.4)

comes to

$$\left[-\sum_I \frac{\hbar^2}{2M_I}\nabla_I^2 + E_k(\mathbf{R}_I)\right]\chi_k = i\hbar\frac{\partial}{\partial t}\chi_k \tag{2.4.5}$$

Based on Hamiltonian of *many-body Schrödinger equation* and time-dependent Schrödinger equation, the Schrödinger equation of nuclei is obtained for a specific molecular dynamics step. Next step is to utilize classical mechanics updating the positions of corresponding nuclei.

Write one solution for a nuclear wavefunction

$$\chi_k(\mathbf{R}_I, t) = A_k(\mathbf{R}_I, t)\exp\left[iS_k(\mathbf{R}_I), t/\hbar\right], \tag{2.4.6}$$

where $A_k$ is the amplitude of the solution and $S_k$ is the phase for a specific electronic state $k$. Transforming Eq. (2.4.5) with Eq. (2.4.6) gives a relation between phase parameter $S_k$ with nuclear wavefunction at electronic state $k$

$$\frac{\partial S_k}{\partial t} + \sum_I \frac{1}{2M_I}(\nabla_I S_k)^2 + E_k = \hbar^2 \sum_I \frac{1}{2M_I}\frac{\nabla_I^2 A_k}{A_k}. \tag{2.4.7}$$

When considering classical limit $\hbar \to 0$, Eq. (2.4.7) simplifies to

$$\frac{\partial S_k}{\partial t} + \sum_I \frac{1}{2M_I}(\nabla_I S_k)^2 + E_k = 0. \tag{2.4.8}$$

From Eq. (2.4.6), probability density $\rho_k$ of the nucleus can be obtained

$$\rho_k = |{\chi_k}^2| \equiv {A_k}^2. \tag{2.4.9}$$

And define the current density $\mathbf{J}_{k,I}$ as

$$\mathbf{J}_{k,I} = {A_k}^2(\nabla_I S_k)/M_I. \tag{2.4.10}$$

According to the Hamilton-Jacobi formulation

$$\frac{\partial S_k}{\partial t} + H_k(\mathbf{R}_I, \nabla_I S_k) = 0. \tag{2.4.11}$$

Combined with classic Hamilton function, it is obtained the classical mechanics of nuclei

$$M_I \ddot{\mathbf{R}}_I(t) = -\nabla_I {V_k}^{\mathrm{BO}} \tag{2.4.12}$$

where ${V_k}^{\mathrm{BO}}$ is an effective potential which drives the movement of nuclei.

### 2.4.2 Born-Oppenheimer molecular dynamics

Next step of Born-Oppenheimer molecular dynamics is to obtain the electrons equations of motion. According to time-dependent Schrödinger equations, it is obtained the *Kohn–Sham equations* for the fixed nuclear positions. Followed by definition of the nuclei as classical points using equations of motion. Hence, definition of electronic equations of motion is relied on the classical dynamics of nuclei

$$M_I \ddot{\mathbf{R}}_I(t) = -\nabla_I \min\{\langle \Psi_0 | H_{\mathrm{e}} | \Psi_0 \rangle\}. \tag{2.4.13}$$

$$E_0 \Psi_0 = H_{\mathrm{e}} \Psi_0 \tag{2.4.14}$$

Then, use the framework of *Kohn-Sham equations* and Lagrange's formalism, Eq. (2.4.13) and Eq. (2.4.14) transform to

$$M_I \ddot{\mathbf{R}}_I(t) = -\nabla_I \min\{\langle \Psi_0 | {H_{\mathrm{e}}}^{\mathrm{KS}} | \Psi_0 \rangle\}, \tag{2.4.15}$$

$$H_{\mathrm{e}}{}^{\mathrm{KS}}\phi_i = \sum_j \Lambda_{ij}\phi_j. \tag{2.4.16}$$

where $H_{\mathrm{e}}{}^{\mathrm{KS}}$ denotes the Hamiltonian for electronic part of time-dependent Schrödinger equation under Kohn-Sham theory. $\Lambda_{ij}$ is the Lagrange multiplier which is used for imposing constrains.

## 2.5 Pseudopotential

A suitable pseudopotential describes a chosen set of core electrons which generate a smoothed density chosen to satisfy various important physical properties from a real set of core electrons. The introduction of pseudopotential can intensively increase calculating efficient. Alternatively, the calculations which do not introduce frozen core approximation are named all–electron calculations. Pseudopotentials with high cutoff energies are called hard pseudopotentials. Those pseudopotential requiring relatively low cutoff energies are recognized as soft pseudopotentials. Developed by Vanderbilt, the ultrasoft pseudopotentials (USPPs) are one widely used pseudopotentials. However, using USPPs is based on empirical parameters. Blöchl invented another pseudopotential called projector augmented–wave (PAW) method[1]. By careful comparison of USPPs, the PAW method, the results are basically identical in many kinds of calculations. When comparing these pseudopotential based calculations with all–electron calculations, the results are reliable. When it comes to materials that are related to containing elements with large differences in electronegativity and strong magnetic moments, the PAW method is more reliable than USPPs method.

## Bibliography

[1] P. E. Blöchl. Projector augmented-wave method. *Phys. Rev. B*, 50:17953–17979, Dec 1994. doi: 10.1103/PhysRevB.50.17953.

[2] P. Hohenberg and W. Kohn. Inhomogeneous electron gas. *Phys. Rev.*, 136:B864–B871, Nov 1964. doi: 10.1103/PhysRev.136.B864.

[3] W. Kohn. Nobel lecture: Electronic structure of matter-wave functions and density functionals. *Rev. Mod. Phys.*, 71:1253–1266, Oct 1999. doi: 10.1103/RevModPhys.71.1253.

[4] W. Kohn and L. J. Sham. Self-consistent equations including exchange and correlation effects. *Phys. Rev.*, 140:A1133–A1138, Nov 1965. doi: 10.1103/PhysRev.140.A1133.

[5] J. P. Perdew and Y. Wang. Pair-distribution function and its coupling-constant average for the spin-polarized electron gas. *Phys. Rev. B*, 46:12947–12954, Nov 1992. doi: 10.1103/PhysRevB.46.12947.

[6] J. P. Perdew, K. Burke, and M. Ernzerhof. Generalized gradient approximation made simple. *Phys. Rev. Lett.*, 77:3865–3868, Oct 1996. doi: 10.1103/PhysRevLett.77.3865.

[7] L. Sham. Approximations of the exchange and correlation potentials. In *Computational Methods in Band Theory*, pages 458–468. Springer, 1971.

# Chapter 3

# Thermodynamic origin of instability in hybrid halide perovskites

**Author contributions:**

Eric Tenuta performed the majority of DFT calculations. I performed DFT calculations of $CH_3NH_3I$ and performed the analysis of the finite temperature effect on the reaction enthalpy for the phase separation of $CH_3NH_3PbI_3$ using the experimental data combined with DFT results. Dr. Oleg Rubel wrote the main manuscript text and prepared figures. All authors reviewed the manuscript. This chapter was published in *Scientific Report*, 2016.

## 3.1 Introduction

The search for cost-effective solar cell absorber materials that can compete with the performance of crystalline silicon and thin-film (GaAs, CdTe and Cu(In,Ga)$Se_2$) solar cells remains the priority for renewable energy material research. A recently emerged class of hybrid halide perovskite materials holds a promise to lead the way towards low-cost photovoltaic devices as they combine an energy conversion efficiency of nearly 20% with a low-temperature solution processing technology[20,25,35,52]. The structure of hybrid perovskites $XMZ_3$ is formed by a combination of various organic cations $X^+ = (CH_3NH_3, NH_4, CH_5N_2)$, metallic cations $M^{2+} = (Pb, Sn)$, and halide anions $Z^- = (Cl, Br, I)$ with $CH_3NH_3PbI_3$ being a prominent example. Perovskite materials possess a unique combination of characteristics that make them useful in photovoltaic applications including a favourable band gap of about $1.5 - 1.6$ eV, efficient optical adsorption, long lifetime of optical excitations, and high level of mobility for charge carriers of both polarities[7,41,48,55].

A major weakness of perovskite solar cells is the degradation of the power conversion efficiency in a moist environment[6,46]. This degradation can be observed in $CH_3NH_3PbI_3$ cells through the colour changing from black to yellow accompanied by a noted decrease in absorption and deterioration of the overall cell performance over time[37,51]. The absorbance at 410 nm has been reported to decrease by 50% after 4 hours of exposure to an environment with the relative humidity of 98%[51]. The same study linearly extrapolated from the previous result concluded that the identical degradation would take approximately one year at the relative humidity of 20%[51].

Frost et al.[10] proposed an acid-base chemistry mechanism to explain the role of water in the degradation process. In this process the decomposition is driven by protic properties of the $[CH_3NH_3]^+$ ion, thus suggesting that aprotic hybrid perovskites (e.g., $(CH_3)_4NPbI_3$) could potentially be more stable[10]. However, this strategy was not confirmed experimentally to the best of our knowledge.

Density functional theory (DFT) simulations of the perovskite-water interface[31,56] provided further insight to the kinetics of the degradation mechanism at the atomic scale. Mosconi et al.[31] observed dissolution of iodine cage and subsequent release of methylammonium ions as well as incorporation of water molecules in the perovskite structure at the interface. The simulation results reported by Zhang and Sit[56] indicate the deprotonation of methylammonium as an initial step in dissolution of the perovskite. Furthermore, the first principle calculations performed without taking into account solvent effects suggest that hybrid halide perovskites may be intrinsically unstable[57]. This conclusion is based on a nearly zero enthalpy of reaction associated with the decomposition of the perovskite structure, which is evaluated based on the total energy of reactant and products. Frost et al.[10] attributed the intrinsic instability of halide perovskites $XMZ_3$ to its relatively low Madelung lattice energy as compared to oxide perovskites that belong to $ABO_3$ family. This result implies that the environmental factors (such as moisture, UV radiation, and elevated temperatures) may only accelerate the decomposition process. Therefore, the effectiveness of encapsulation as a strategy to prevent moisture damage may not guarantee long-term stability of perovskite solar cells as evidenced by Han et al.[15].

Here we utilize DFT to explore the stability of perovskite structures from a thermodynamic perspective. We will show that the finite temperature effects, that are omitted in former calculation of the stability of $CH_3NH_3PbI_3$[16,53], can play a decisive role when the decomposition reaction takes place in the presence of a solvent and yields a water-soluble product. We will also examine properties of several alternatives, $NH_3OHPbI_3$, $NH_3NH_2PbI_3$, $PH_4PbI_3$, $SbH_4PbI_3$, and $CsPbBr_3$ in a search for perovskite compounds for photovoltaic applications.

## 3.2 Results and discussion

### 3.2.1 Chemical stability of $CH_3NH_3PbI_3$

We begin by examining the chemical stability of $CH_3NH_3PbI_3$ against decomposition. The structural changes in the course of degradation involve disappearance of X-ray diffraction peaks that are characteristic for $CH_3NH_3PbI_3$ and appearance of $PbI_2$ peaks[33], which suggests the following reaction (phases)

$$CH_3NH_3PbI_3 \rightleftharpoons PbI_2 + CH_3NH_3I. \tag{3.2.1}$$

The standard approach for predicting the direction of a chemical reaction involves evaluation of the change in the Gibbs free energy between reactants and products (see Sholl and Steckel[40], Chap. 7), which can be split into two terms for convenience

$$\Delta G^\circ_T = \Delta H^\circ_{0\,\mathrm{K}} + \Delta\tilde{\mu}^\circ_T \ . \tag{3.2.2}$$

Here $\Delta H^\circ_{0\,\mathrm{K}}$ is the standard reaction enthalpy change at zero temperature, and $\Delta\tilde{\mu}^\circ_T$ captures finite temperature effects on the chemical potentials of species involved.

The enthalpy change at zero temperature can be readily evaluated based on the DFT total energy calculations

$$\Delta H^\circ_{0\,\mathrm{K}} \approx \sum_i^{\text{products}} n_i E_{\mathrm{tot}}[i] - \sum_j^{\text{reactants}} n_j E_{\mathrm{tot}}[j] \ , \tag{3.2.3}$$

where $n$ and $E_{\mathrm{tot}}$ are the number and the total energy of the chemical species involved in the reaction. It should be noted that the bare DFT total energies in Eq. (3.2.3) do not fully capture the standard enthalpy changes at zero temperature as they do not include a zero-point vibrational energy and, less importantly, the standard pressure effects on $E_{\mathrm{tot}}$. Therefore, the relation (3.2.3) is approximate. In the case of $CH_3NH_3PbI_3$, the

decomposition reaction yields two products: $PbI_2$ and $CH_3NH_3I$. The corresponding lattice parameters and total energies of the reactant and products are listed in Table 3.1. The values yield the dissociation reaction enthalpy of $\Delta H^{\circ}_{0\,\mathrm{K}} = 0.05$ eV per formula unit (f.u.) for $CH_3NH_3PbI_3$ evaluated using Eq. (3.2.3). The result is within the range of theoretical values reported in the literature, including $\Delta H^{\circ}_{0\,\mathrm{K}} = 0.1$ eV[4] and $-0.06$ eV[57]. The corresponding experimental value is $\Delta H^{\circ}_{300\,\mathrm{K}} = -0.36$ eV[32], which is far too low to explain formability of this perovskite and needs further experimental verifications. The theoretical value of $\Delta H^{\circ}_{0\,\mathrm{K}}$ contrasts sharply with the formation enthalpy of major solar cell compound materials, such as GaAs and CdTe, which is of the order of $0.8 - 1$ eV/f.u.[45,58].

The poor chemical stability of $CH_3NH_3PbI_3$ is often attributed to the nearly vanishing value of $\Delta H$[53,57]. In fact, this only implies that the decomposition does not involve a heat exchange with the environment. It is the finite temperature contribution to the chemical potential difference between reactants and products

$$\Delta\tilde{\mu}^{\circ}_{T} = \sum_{i}^{\text{products}} n_i \tilde{\mu}^{\circ}_{T}[i] - \sum_{j}^{\text{reactants}} n_j \tilde{\mu}^{\circ}_{T}[j] \ . \tag{3.2.4}$$

that remains overlooked in previous stability analysis[16,32,53]. Here $\tilde{\mu}^{\circ}_{T}$ represents the final temperature correction to the chemical potential of spieces

$$\tilde{\mu}^{\circ}_{T} = H^{\circ}_{T} - H^{\circ}_{0\,\mathrm{K}} - TS^{\circ}_{T} \ , \tag{3.2.5}$$

which is not captured in a bare DFT total energy. Although the extension of DFT calculations to finite temperatures is possible[42], it is computationally intensive. Therefore, NIST-JANAF thermochemical tables as well as other experimental resources were used to evaluate the final temperature correction using Eq. (7.3.4) (see Table 3.1 and references therein).

The final temperature correction to the Gibbs free energy of $CH_3NH_3PbI_3$ decomposition

reaction

$$\Delta\tilde{\mu}^{\circ}_{T} = \tilde{\mu}^{\circ}_{T}(\mathrm{PbI_2}) + \tilde{\mu}^{\circ}_{T}(\mathrm{CH_3NH_3I}) - \tilde{\mu}^{\circ}_{T}(\mathrm{CH_3NH_3PbI_3}) \tag{3.2.6}$$

amounts to $\Delta\tilde{\mu}^{\circ}_{300\ \mathrm{K}} = 0.11$ eV/f.u. The resultant Gibbs free energy difference in Eq. (3.2.2) is positive $\Delta G^{\circ}_{300\ \mathrm{K}} = 0.16$ eV/f.u. indicating that the final temperature effects tend to stabilize the perovskite structure against spontaneous decomposition under standard conditions for temperature and pressure. However, the result should be taken with caution, since the uncertainty in reaction energies obtained with Perdew, Burke, and Ernzerhof (PBE)[36] exchange-correlation functional is of the order of $\pm 0.03$ eV/atom[17].

The thermodynamic characteristics of $\mathrm{CH_3NH_3PbI_3}$ perovskites indicate that it is chemical stability is fragile, and the balance can be easily shifted if the environment changes. A possible scenario that will be discussed here involves the presence of a solvent. Unlike $\mathrm{PbI_2}$ that has limited solubility in water, the methylammonium iodide is highly soluble in water, which should be taken into account when calculating its chemical potential (see Wright[47], Chap. 8).

The actual chemical potential of an electrolyte

$$\mu_T \approx E_{\mathrm{total}} + \tilde{\mu}^{\circ}_{T} + k_B T \ln(a_{\pm}) \tag{3.2.7}$$

can be significantly different from its value in the standard state depending on the activity coefficient $a_{\pm}$ of the solute[3]. The mean ionic activity $a_{\pm}$ of $\mathrm{CH_3NH_3I}$ solution

$$a_{\pm} = (\gamma_{\pm} c/c^{\circ})^2 \ , \tag{3.2.8}$$

is determined by its molar concentration $c$ relative to the concentration in standard state $c^{\circ} = 1$ M and the mean ionic activity coefficient $\gamma_{\pm}$, which account for non-ideality of the solution. In a dilute solution limit, $c \ll 1$ M and $\gamma_{\pm} \sim 1$, the chemical potential of aqueous

$CH_3NH_3I$ drops much below its value in the solid phase

$$\mu[CH_3NH_3I\ (aq)] \ll \mu[CH_3NH_3I\ (s)]\ , \tag{3.2.9}$$

which shifts the balance in Eq. (3.2.1) to the right. Accordingly, the aqueous solubility of methylammonium iodide drives the dissociation of $CH_3NH_3PbI_3$ as previously suggested by Niu et al.[33].

The decomposition proceeds as long as the following condition is fulfilled

$$c < \frac{c^\circ}{\gamma_\pm} \exp\left(-\frac{\Delta G_T^\circ}{2k_BT}\right)\ . \tag{3.2.10}$$

Using the value of $\Delta G^\circ_{300\ \mathrm{K}} = 0.16$ eV and assuming $\gamma_\pm \sim 1$, it is possible to estimate the saturation concentration $c_\mathrm{s}$ of $CH_3NH_3I$ dissolved in water at which further decomposition of $CH_3NH_3PbI_3$ is suppressed. Equation (3.2.10) yields $c_\mathrm{s} \sim 50$ mM (or $\sim 8$ g/L). Given the fact that the thickness of the absorbing material in perovskite solar cells is only 0.5 $\mu$m[26], even a droplet of water is sufficient to destroy a device with the area of a several square centimeters.

### 3.2.2 Alternative absorber materials

The stability of hybrid lead halide perovskites can be improved by substituting iodine with more electronegative elements (bromine or chlorine)[32]. However, the associated increase of the band gap that exceeds 2 eV[4] limits the accessible power conversion efficiency when aiming for solar cell absorber materials. Therefore, we focus on perovskite structures of the family $XPbI_3$ and explore several alternatives for the cation $X =$ $[NH_3OH]^+$, $[NH_3NH_2]^+$, $[PH_4]^+$, $[SbH_4]^+$. A solid solution of hydroxylammonium and hydrazinium ions were recently used in hybrid perovskite structures[21]. Phosphonium and particularly stibonium ions

were theoretically predicted to produce more efficient photovoltaic materials when substituted for methylammonium in lead iodide-based perovskites due to the reduced band gap and improved effective mass[8].

Unit cell volumes and band gaps of the corresponding perovskite structures are listed in Table 3.2. The band gaps were calculated without taking into account relativistic effects. This approach allows to minimizing the error by taking advantage of an error cancellation between the band gap reduction due to spin-orbit coupling and its opening introduced by a port-DFT correction[30]. As a result, the values of the band gap are only slightly overestimated (approximately 0.1 eV). The results indicate that small changes in the volume (less than 5%) lead to a sizeable change in the band gap. In contrast to group IV, III-V and II-VI semiconductors, the band gap in perovskite structures *increases* when the unit cell expands as Dittrich[7] noticed.

The chemical stability of perovskite structures in Table 3.2 was initially assessed by computing the decomposition reaction enthalpy $\Delta H^{\circ}_{0\,\mathrm{K}}$. In this calculation, we shall assume that all structures decompose following the pathway similar to Eq. (3.2.1).

Results for the decomposition reaction enthalpy calculated using Eq. (3.2.3) are given in Table 3.2, where the compounds are sorted in the order of increasing $\Delta H^{\circ}_{0\,\mathrm{K}}$ (higher values favour stability of perovskites). All hybrid perovskites with the negative reaction enthalpy can be rendered as unstable, including $SbH_4PbI_3$ with the promising band gap value.

The pseudocubic structures of $CH_3NH_3PbI_3$ perovskite is shown in Fig. 3.1 alongside with the pseudocubic structure of $CH_3NH_3PbI_3$. The band structure of the material calculated taking into account spin-orbit coupling and a meta-GGA band gap correction are presented in Fig. 3.2.

Finally, it will be instructive to discuss the stability of an inorganic $CsPbBr_3$ perovskite. Unlike $CH_3NH_3PbI_3$, the decomposition reaction enthalpy of $CsPbBr_3$ is high (Table 3.2). Assuming that both compounds have the same magnitude of the final temperature contribution $\Delta\tilde{\mu}^{\circ}_{300\ \mathrm{K}}$ to the free energy, one would expect the free energy of $CsPbBr_3$ to be

approximately 0.5 eV/f.u. lower than that for decomposition products ($PbBr_2$ and CsBr) indicating strong chemical stability of $CsPbBr_3$ against spontaneous decomposition. However, it is found experimentally that the performance of $CsPbBr_3$-based solar cells (not encapsulated) decays over time, although slower than $CH_3NH_3PbI_3$-based devices[24]. This observation reveals susceptibility of both perovskite structures to the reaction with moisture, despite of the high reaction enthalpy of $CsPbBr_3$ and lack of proton-donating groups. We believe that the aqueous solubility of CsBr has some significance for explaining this effect. The slow degradation rate of $CsPbBr_3$ can be attributed to the greater value of $\Delta G^{\circ}_{300\ \mathrm{K}}$, which translates into a much lower saturation concentration of CsBr $c_\mathrm{s} \sim 60\ \mu$M as compared to $c_\mathrm{s} \sim 50$ mM for $CH_3NH_3I$ (see discussion in the preceding subsection).

## 3.3 Conclusions

The performance of $CH_3NH_3PbI_3$ perovskites solar cells deteriorates when exposed to environmental factors, such as moisture and sunlight. This remains the main barrier on the way to their commercialization. The ability to assess the stability of solar cell absorber materials using first principle calculations is an important attribute for the design of new materials. We showed that the instability of perovskites can be captured using DFT total energy calculations for reactants and products augmented with additional thermodynamic data to account for finite temperature effects. The finite temperature effects play a minor role in stabilizing the perovskite structure when products of the decomposition reaction are solids. However, the finite temperature contribution to the Gibbs free energy of the degradation reaction becomes crucially important in the case of when products of the decomposition are aqueous solutions or gases.

Our calculations suggest that the $CH_3NH_3PbI_3$ structure can be stable against spontaneous decomposition provided it is isolated from environmental factors. The situation changes drastically in the presence of water. The aqueous solubility of the $CH_3NH_3I$ salt

lowers its chemical potential relative to the solid phase, especially in a dilute limit. This property favours decomposition of $CH_3NH_3PbI_3$ in the moist environment. Therefore, a limited solubility of the decomposition reaction products is anticipated to improve structural stability. Generalizing this result to other perovskites, the aqueous solubility of $HC(NH_2)_2I$, $SbH_4I$, and CsBr undermines stability of the corresponding perovskite structures.

In a search for alternative perovskites, $NH_3OHPbI_3$, $NH_3NH_2PbI_3$, $PH_4PbI_3$, $SbH_4PbI_3$, $CsPbBr_3$ compounds were investigated. $NH_3OHPbI_3$, $NH_3NH_2PbI_3$, $PH_4PbI_3$, and $SbH_4PbI_3$ were concluded unstable due to the low formation enthalpy. The $CsPbBr_3$ structure is prone to degradation in moist conditions, in spite of the favourable formation enthalpy, due to solubility of CsBr.

## 3.4 Computational details

The first-principles electronic structure calculations were carried out using DFT[22]. Two implementations were employed. A projector augmented wave (PAW) method[23,43] implemented in the ABINIT package[12,13,14] was utilized for the structural optimization and calculations of the chemical stability. The band structure calculations were performed in the Wien2k package[2] based on a full potential linear augmented plane wave method.

### 3.4.1 Structure optimization

The $CH_3NH_3PbI_3$ perovskite is known to exist in three different polymorphs[1,41]: orthorhombic, tetragonal, and cubic. A tetragonal $\beta$-phase is stable at room temperature and was used in these calculations. A pseudocubic structure was used to represent $SF_3PbI_3$, $NH_3OHPbI_3$, $NH_3NH_2PbI_3$, $PH_4PbI_3$, and $SbH_4PbI_3$. An orthorhombic (Pnma) structure was chosen to represent $\delta$-$CsPbBr_3$. Optimization of lattice parameters was carried out in conjunction with the relaxation of internal degrees of freedom for all structures studied here. The structure was considered optimized when the magnitude of Hellmann-Feynman forces acting on

atoms dropped below 0.5 mHa/Bohr and components of the stress tensor were less than 1 $\mu$Ha/Bohr$^3$. The Brillouin zone was sampled using an unshifted mesh with the density one k-point per every 0.01 Bohr$^{-1}$ length of each reciprocal lattice vector. The cutoff energy for a plane wave expansion was set at 15 Ha.

Standard structures of solid $PbI_2$ (hexagonal, space group 164 ($P\bar{3}m1$)), $PbF_2$ (cubic, space group 225 ($Fm\bar{3}m$)) and $PbBr_2$ (orthorhombic, space group 62 (Pbnm)) were used to represent possible reactants. The structure of $CH_3NH_3I$ undergoes several phase transitions with increasing temperature[50]. A tetragonal $\alpha'$-phase (space group 129 (P4/nmm)), which is stable at room temperature, resembles a rock-salt ionic structure[19]. The total energy of water was derived from its natural $I_h$ solid structure (hexagonal, space group 194 ($P6_3/mmc$)[9]). Structures of $NH_3OHI$, $NH_3NH_2I$, $PH_4I$, and $SbH_4I$ were derived using CsCl structure as a prototype. All structures were fully optimized as describe in the preceding paragraph (without constrains to the geometry).

Gaseous phases were modelled as an individual molecule surrounded by 30 Bohrs of vacuum. The internal degrees of freedom were relaxed. Only Γ-point was used in the Brillouin zone.

Perdew, Burke, and Ernzerhof[36] version of the generalized gradient approximation was chosen for the exchange–correlation functional due to its superior accuracy in predicting cohesive properties of solids and molecules.

Garrity, Bennett, Rabe, and Vanderbilt[11] GBRV (v1.5) PAW pseudopotentials were employed for all elements. VESTA 3 package was used for visualization of atomic structure[28]. Structure files of all perovskite compounds and non-trivial salts are included in the supplementary information in a cif-format.

### 3.4.2 Band structure

The band structure of pseudocubic $CH_3NH_3PbI_3$ was calculated with the Wien2k package[2] using a full potential linear augmented plane wave method. The Brillouin zone was sampled

using $6 \times 6 \times 6$ Monkhorst and Pack[29] mesh. The muffin-tin radii $R_{\mathrm{MT}}$ where set to 0.62, 1.16, 1.22, 1.38, 2.2, and 2.2 Bohr for H, N, C, S, I, and Pb respectively. The cutoff energy of $-6$ Ry was used to separates valence and core electrons. The product $R_{\mathrm{min}}^{\mathrm{MT}} K_{\mathrm{max}}$, which determines the accuracy of a plane wave expansion of the wave function, was set at the values of 3.5 for $CH_3NH_3PbI_3$ compound. The low $R_{\mathrm{min}}^{\mathrm{MT}} K_{\mathrm{max}}$ for $CH_3NH_3PbI_3$ is due to a small size of the muffin-tin sphere around hydrogen atoms. Optimized lattice parameters and atomic positions from ABINIT calculations were used. The Tran-Blaha modified Becke-Johnson (TBmBJ) potential[44] was applied in order to overcome shortcomings of DFT semilocal exchange–correlation functions in predicting band gaps of insulators.

Table 3.1: Equilibrium lattice parameters, electronic total energy $E_{\text{tot}}$ per formula unit (f.u.), and change in the chemical potential $\tilde{\mu}^{\circ}_{300\text{ K}}$ that accounts for the free energy of the compounds at the finite temperature and pressure not captured in DFT total energy.

| Compound | Lattice parameter (Å) | $E_{\text{tot}}$ (eV/f.u.) | $\tilde{\mu}^{\circ}_{300\text{ K}}$ (eV/f.u.) |
|---|---|---|---|
| $CH_3NH_3PbI_3$ (solid) | $a = 8.92, c/a = 1.48$[1] | −3146.596 | −0.70[34] |
| $PbI_2$ (solid) | $a = 4.668, c/a = 1.63$[2] | −2302.282 | −0.34[5] |
| $CH_3NH_3I$ (solid) | $a = 5.146, c/a = 1.86$[3] | −844.266 | −0.25[49] |

Table 3.2: Dissociation reaction enthalpy $\Delta H^{\circ}_{0\text{ K}}$ of perovskite structures presented together with volume of the unit cell $V_0$ and the band gap energy $E_{\text{g}}^{\text{DFT-GGA}}$ calculated self-consistently without taking into account the spin-orbit coupling. The generalized reaction for chemical decomposition is given by Eq. (3.2.1).

| Compound | $V_0$ (Å$^3$/f.u.) | $E_{\text{g}}^{\text{DFT-GGA}}$ (eV) | $\Delta H^{\circ}_{0\text{ K}}$ (eV/f.u.)[4] |
|---|---|---|---|
| $NH_3OHPbI_3$ | 270 | 1.89 | −0.25 |
| $NH_3NH_2PbI_3$ | 274 | 1.80 | −0.22 |
| $PH_4PbI_3$ | 268 | 1.60 | −0.18 |
| $SbH_4PbI_3$ | 265 | 1.53 | −0.11 |
| $\beta$-$CH_3NH_3PbI_3$ | 263 | 1.67 | +0.05 |
| $\delta$-$CsPbBr_3$ | 208 | 2.10 | +0.37[5] |

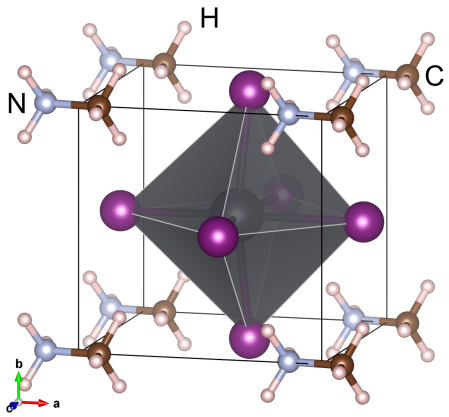


Figure 3.1: Structure of pseudocubic $CH_3NH_3PbI_3$.

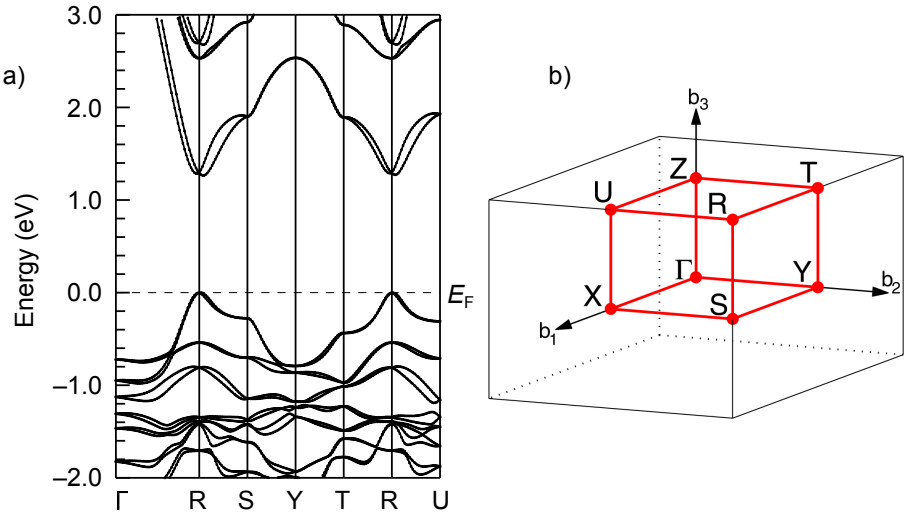


Figure 3.2: Band structure of pseudocubic $CH_3NH_3PbI_3$ (a) calculated along the path between high-symmetry points in the Brillouin zone (b) taking into account spin-orbit coupling and non-local exchange correction. The origin of the energy scale is set at the Fermi energy $E_F$. Labels of the high-symmetry point in the Brillouin zone correspond to an orthorhombic lattice[39].

# Bibliography

[1] T. Baikie, Y. Fang, J. M. Kadro, M. Schreyer, F. Wei, S. G. Mhaisalkar, M. Graetzel, and T. J. White. Synthesis and crystal chemistry of the hybrid perovskite $CH_3NH_3PbI_3$ for solid-state sensitised solar cell applications. *J. Mater. Chem. A.*, 1(18):5628–5641, 2013. doi: 10.1039/C3TA10518K.

[2] P. Blaha, K. Schwarz, G. K. H. Madsen, D. Kvasnicka, and J. Luitz. Wien2k: An augmented plane wave + local orbitals program for calculating crystal properties. pages 1–269, 2001.

[3] M. J. Blandamer, J. B. F. N. Engberts, P. T. Gleeson, and J. C. R. Reis. Activity of water in aqueous systems; a frequently neglected property. *Chem. Soc. Rev.*, 34: 440–458, 2005. doi: 10.1039/B400473F.

[4] A. Buin, R. Comin, J. Xu, A. H. Ip, and E. H. Sargent. Halide-dependent electronic structure of organolead perovskite materials. *Chem. Mater.*, 27(12):4405–4412, 2015. doi: 10.1021/acs.chemmater.5b01909.

[5] M. W. Chase. *NIST-JANAF Thermochemical Tables*. American Inst. of Physics, 1998.

[6] J. A. Christians, P. A. M. Herrera, and P. V. Kamat. Transformation of the excited state and photovoltaic efficiency of $CH_3NH_3PbI_3$ perovskite upon controlled exposure to humidified air. *J. Am. Chem. Soc.*, 137:1530–1538, 2015. doi: 10.1021/ja511132a.

[7] T. Dittrich. Temperature dependence of the band gap of $CH_3NH_3PbI_3$ stabilized with pmma: A modulated surface photovoltage study. *J. Phys. Chem. C*, 119:23968–23972, 2015. doi: 10.1021/acs.jpcc.5b07132.

[8] M. R. Filip, C. Verdi, and F. Giustino. GW band structures and carrier effective masses of $CH_3NH_3PbI_3$ and hypothetical perovskites of the type $APbI_3$: A = $NH_4$, $PH_4$, $AsH_4$, and $SbH_4$. *J. Phys. Chem. C*, 119:25209–25219, 2015. doi: 10.1021/acs.jpcc.5b07891.

[9] A. D. Fortes, I. G. Wood, D. Grigoriev, M. Alfredsson, S. Kipfstuhl, K. S. Knight, and R. Smith. No evidence for large-scale proton ordering in antarctic ice from powder neutron diffraction. *J. Chem. Phys.*, 120:11376–11379, 2004. doi: 10.1063/1.1765099.

[10] J. M. Frost, K. T. Butler, F. Brivio, C. H. Hendon, M. Van Schilfgaarde, and A. Walsh. Atomistic origins of high-performance in hybrid halide perovskite solar cells. *Nano Lett.*, 14(5):2584–2590, 2014. doi: 10.1021/nl500390f.

[11] K. F. Garrity, J. W. Bennett, K. M. Rabe, and D. Vanderbilt. Pseudopotentials for high-throughput DFT calculations. *Comp. Mater. Sci.*, 81:446–452, 2014. doi: 10.1016/j.commatsci.2013.08.053.

[12] X. Gonze. A brief introduction to the abinit software package. *Zeit. Kristallogr.*, 220: 558–, 2005. doi: 10.1524/zkri.220.5.558.65066.

[13] X. Gonze, J.-M. Beuken, R. Caracas, F. Detraux, M. Fuchs, G.-M. Rignanese, L. Sindic, M. Verstraete, G. Zerah, and F. Jollet. First-principles computation of material properties: the abinit software project. *Comp. Mater. Sci.*, 25:478–492, 2002. doi: 10.1016/S0927-0256(02)00325-7.

[14] X. Gonze, B. Amadon, P.-M. Anglade, J.-M. Beuken, F. Bottin, P. Boulanger, F. Bruneval, D. Caliste, R. Caracas, and M. Côté. Abinit: First-principles approach to material and nanosystem properties. *Comput. Phys. Commun.*, 180:2582–2615, 2009. doi: 10.1016/j.cpc.2009.07.007.

[15] Y. Han, S. Meyer, Y. Dkhissi, K. Weber, J. M. Pringle, U. Bach, L. Spiccia, and Y.-B. Cheng. Degradation observations of encapsulated planar $CH_3NH_3PbI_3$ perovskite solar cells at high temperatures and humidity. *J. Mater. Chem. A*, 3(15):8139–8147, 2015. doi: 10.1039/C5TA00358J.

[16] J. Haruyama, K. Sodeyama, L. Han, and Y. Tateyama. Termination dependence of

tetragonal $CH_3NH_3PbI_3$ surfaces for perovskite solar cells. *J. Phys. Chem. Lett.*, 5: 2903–2909, 2014. doi: 10.1021/jz501510v.

[17] G. Hautier, S. P. Ong, A. Jain, C. J. Moore, and G. Ceder. Accuracy of density functional theory in predicting formation energies of ternary oxides from binary oxides and its implication on phase stability. *Phys. Rev. B*, 85:155208, Apr 2012. doi: 10.1103/PhysRevB.85.155208.

[18] S. B. Hendricks. V. the crystal structures of the monomethyl ammonium halides. *Z. Kristallogr. Cryst. Mater.*, 67:106–118, 1928. doi: 10.1524/zkri.1928.67.1.106.

[19] H. Ishida, H. Maeda, A. Hirano, T. Fujimoto, Y. Kubozono, S. Kashino, and S. Emura. Exafs study on the phase transition (phase $\alpha$'–$\delta$) in $CH_3NH_3I$. *Z. Naturforsch. A.*, 50 (9):876–880, 1995. doi: 10.1515/zna-1995-0914.

[20] H. S. Jung and N. G. Park. Perovskite solar cells: From materials to devices. *Small*, 11:10–25, 2014. doi: 10.1002/smll.201402767.

[21] G. Kieslich. Tuneable mechanical and dynamical properties in the ferroelectric perovskite solid solution $NH_3NH_2$(1-x)$NH_3$OHxZn$(HCOO)_3$. *Chem. Sci.*, 7:5108–5112, 2016. doi: 10.1039/C6SC01247G.

[22] W. Kohn and L. J. Sham. Self-consistent equations including exchange and correlation effects. *Phys. Rev.*, 140(4A):A1133, 1965. doi: 10.1103/PhysRev.140.A1133.

[23] G. Kresse and D. Joubert. From ultrasoft pseudopotentials to the projector augmented-wave method. *Phys. Rev. B*, 59(3):1758, 1999.

[24] M. Kulbak, S. Gupta, N. Kedem, I. Levine, T. Bendikov, G. Hodes, and D. Cahen. Caesium enhances long-term stability of lead bromide perovskite-based solar cells. *J. Phys. Chem. Lett.*, 7:167–172, 2015. doi: 10.1021/acs.jpclett.5b02597.

[25] M. M. Lee, J. Teuscher, T. Miyasaka, T. N. Murakami, and H. J. Snaith. Efficient hybrid solar cells based on meso-superstructured organometal halide perovskites. *Science*, 338:643–647, 2012. doi: 10.1126/science.1228604.

[26] D. Liu, M. K. Gangishetty, and T. L. Kelly. Effect of $CH_3NH_3PbI_3$ thickness on device efficiency in planar heterojunction perovskite solar cells. *J. Mater. Chem. A*, 2: 19873–19881, 2014. doi: 10.1039/C4TA02637C.

[27] O. Madelung, U. Rössler, and M. Schulz. *Lead diiodide ($PbI_2$) crystal structure, lattice parameters, thermal expansion.* Springer-Verlag Berlin Heidelberg, 1998.

[28] K. Momma and F. Izumi. Vesta 3 for three-dimensional visualization of crystal, volumetric and morphology data. *J. Appl. Crystallogr.*, 44:1272–1276, 2011. doi: 10.1107/S0021889811038970.

[29] H. J. Monkhorst and J. D. Pack. Special points for brillouin-zone integrations. *Phys. Rev. B*, 13:5188–, 1976. doi: 10.1103/PhysRevB.13.5188.

[30] E. Mosconi, A. Amat, M. K. Nazeeruddin, M. Grtzel, and F. De Angelis. First-principles modeling of mixed halide organometal perovskites for photovoltaic applications. *J. Phys. Chem. C*, 117:13902–13913, 2013. doi: 10.1021/jp4048659.

[31] E. Mosconi, J. M. Azpiroz, and F. De Angelis. *Ab Initio* molecular dynamics simulations of methylammonium lead iodide perovskite degradation by water. *Chem. Mater.*, 27(13):4885–4892, 2015. doi: 10.1021/acs.chemmater.5b01991.

[32] G. Nagabhushana, R. Shivaramaiah, and A. Navrotsky. Direct calorimetric verification of thermodynamic instability of lead halide hybrid perovskites. *P. Natl. Acad. Sci. USA.*, 113(28):7717–7721, 2016. doi: 10.1016/j.jallcom.2003.10.017.

[33] G. Niu, W. Li, F. Meng, L. Wang, H. Dong, and Y. Qiu. Study on the stability

of $CH_3NH_3PbI_3$ films and the effect of post-modification by aluminum oxide in all-solid-state hybrid solar cells. *J. Mater. Chem. A*, 2(3):705–710, 2014. doi: 10.1039/C3TA13606J.

[34] N. Onoda-Yamamuro, T. Matsuo, and H. Suga. Calorimetric and IR spectroscopic studies of phase transitions in methylammonium trihalogenoplumbates (ii). *J. Phys. Chem. Solids.*, 51(12):1383–1395, 1990. doi: 10.1016/0022-3697(90)90021-7.

[35] N.-G. Park. Organometal perovskite light absorbers toward a 20% efficiency low-cost solid-state mesoscopic solar cell. *J. Phys. Chem. Lett.*, 4:2423–2429, 2013. doi: 10.1021/jz400892a.

[36] J. P. Perdew, K. Burke, and M. Ernzerhof. Generalized gradient approximation made simple. *Phys. Rev. Lett.*, 77:3865, 1996. doi: 10.1103/PhysRevLett.77.3865.

[37] B. Philippe. Chemical and electronic structure characterization of lead halide perovskites and stability behavior under different exposures—a photoelectron spectroscopy investigation. *Chem. Mater.*, 27:1720–1731, 2015. doi: 10.1021/acs.chemmater.5b00348.

[38] A. Poglitsch and D. Weber. Dynamic disorder in methylammoniumtrihalogenoplumbates (ii) observed by millimeter-eave spectroscopy. *J. Chem. Phys.*, 87(11):6373–6378, 1987. doi: doi:10.1063/1.453467.

[39] W. Setyawan and S. Curtarolo. High-throughput electronic band structure calculations: Challenges and tools. *Comp. Mater. Sci.*, 49:299–312, 2010. doi: 10.1016/j.commatsci.2010.05.010.

[40] D. Sholl and J. A. Steckel. *Density Functional Theory: A Practical Introduction*. John Wiley & Sons, Hoboken, New Jersey, 2011.

[41] C. C. Stoumpos, C. D. Malliakas, and M. G. Kanatzidis. Semiconducting tin and lead iodide perovskites with organic cations: Phase transitions, high mobilities, and near-infrared photoluminescent properties. *Inorg. Chem.*, 52(15):9019–9038, 2013. doi: 10.1021/ic401215x.

[42] A. Togo, L. Chaput, I. Tanaka, and G. Hug. First-principles phonon calculations of thermal expansion in $Ti_3SiC_2$, $Ti_3AlC_2$, and $Ti_3GeC_2$. *Phys. Rev. B*, 81:174301–, 2010. doi: 10.1103/PhysRevB.81.174301.

[43] M. Torrent, F. Jollet, F. Bottin, G. Zérah, and X. Gonze. Implementation of the projector augmented-wave method in the abinit code: Application to the study of iron under pressure. *Comp. Mater. Sci.*, 42:337–351, 2008. doi: 10.1016/j.commatsci.2007.07.020.

[44] F. Tran and P. Blaha. Accurate band gaps of semiconductors and insulators with a semilocal exchange-correlation potential. *Phys. Rev. Lett.*, 102:226401–, 2009. doi: 10.1103/PhysRevLett.102.226401.

[45] S. H. Wei and S. B. Zhang. Theoretical study of doping limits of CdTe. *NCPB Program Review Meeting*, pages 14–17, 2001.

[46] S. Wozny. Controlled humidity study on the formation of higher efficiency formamidinium lead triiodide-based solar cells. *Chem. Mater.*, 27:4814–4820, 2015. doi: 10.1021/acs.chemmater.5b01691.

[47] M. R. Wright. *An Introduction To Aqueous Electrolyte Solutions*. John Wiley & Sons, 2007.

[48] Y. Yamada. Near-band-edge optical responses of solution-processed organic-inorganic hybrid perovskite $CH_3NH_3PbI_3$ on mesoporous $TiO_2$ electrodes. *Appl. Phys. Express*, 7:032302–, 2014. doi: 10.7567/APEX.7.032302.

[49] O. Yamamuro, M. Oguni, T. Matsuo, and H. Suga. Calorimetric and dilatometric studies on the phase transitions of crystalline $CH_3NH_3I$. *J. Chem. Thermodynamics*, 18:939–954, 1986. doi: 10.1016/0021-9614(86)90152-7.

[50] O. Yamamuro, M. Oguni, T. Matsuo, and H. Suga. Pt phase relations of methylammonium halides. *Thermochim. Acta*, 98:327–338, 1986. doi: 10.1016/0040-6031(86)87103-9.

[51] J. Yang, B. D. Siempelkamp, D. Liu, and T. L. Kelly. Investigation of $CH_3NH_3PbI_3$ degradation rates and mechanisms in controlled humidity environments using *in Situ* techniques. *Acs Nano*, 9:1955–1963, 2015. doi: 10.1021/nn506864k.

[52] W. S. Yang. High-performance photovoltaic perovskite layers fabricated through intramolecular exchange. *Science*, 348:1234–1237, 2015. doi: 10.1126/science.aaa9272.

[53] W.-J. Yin, T. Shi, and Y. Yan. Unusual defect physics in $CH_3NH_3PbI_3$ perovskite solar cell absorber. *Appl. Phys. Lett.*, 104(6):063903, Feb. 2014. doi: 10.1063/1.4864778.

[54] W.-J. Yin, Y. Yan, and S.-H. Wei. Anomalous alloy properties in mixed halide perovskites. *J. Phys. Chem. Lett.*, 5:3625–3631, 2014. doi: 10.1021/jz501896w.

[55] J. You. Low-temperature solution-processed perovskite solar cells with high efficiency and flexibility. *Acs Nano*, 8:1674–1680, 2014. doi: 10.1021/nn406020d.

[56] L. Zhang and P. H.-L. Sit. Ab initio study of interaction of water, hydroxyl radicals, and hydroxide ions with $CH_3NH_3PbI_3$ and $CH_3NH_3PbBr_3$ surfaces. *J. Phys. Chem. C*, 119(39):22370–22378, 2015. doi: 10.1021/acs.jpcc.5b07000.

[57] Y. Zhang, S. Chen, P. Xu, H. Xiang, X. Gong, A. Walsh, and S. Wei. Intrinsic instability of the hybrid halide perovskite semiconductor $CH_3NH_3PbI_3$. *Chin. Phys. Lett.*, 35(3):036104, 2018. doi: 10.1088/0256-307X/35/3/036104.

[58] G. Zollo and R. M. Nieminen. Small self-interstitial clusters in GaAs. *J. Phys.: Condens. Matter*, 15:843–853, 2003. doi: 10.1088/0953-8984/15/6/311.

# Chapter 4

# Ionization energy as a stability criterion for halide perovskites

**Author contributions:** I conceived the idea to extend the Born-Haber cycle to hybrid halide perovskites to understand the origin of the close-to-zero reaction enthalpy. All calculations and data analysis were conducted by myself with aid from Dr. Oleg Rubel. The manuscript was drafted by myself, and edited by Dr. Oleg Rubel. This chapter was published in *The Journal of Physical Chemistry C*, 2017.

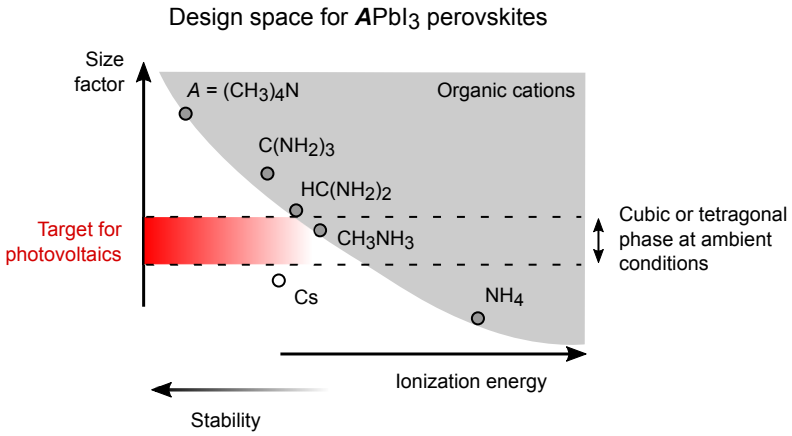

## 4.1 Introduction

The efficiencies of hybrid organic-inorganic perovskite solar cells have already increased to over 20%[30,36,49,65]. Fabrication of hybrid organic perovskite is based on a low-temperature solution method, thus offering a low-cost alternative to crystalline thin-film photovoltaic devices. The main obstacle hindering the commercialization of hybrid organic perovskite solar cells is the instability of the active material. Hybrid perovskites are prone to a phase separation that takes place instantly under the ambient environment (moisture, UV radiation, atmospheric oxygen, etc.)[3,5,64]. The detrimental role of moisture in creating a degradation pathway for halide perovskites was previously discussed from acid-base chemistry[13], molecular dynamic simulations[44,66], hydrolysis reaction[68] and thermodynamic[61] perspectives. Encapsulation of the perovskite cells does not prevent their degradation either. The active layer of encapsulated hybrid organic perovskites eventually decomposes after a period time that ranges from several days to a month[4,23].

Intrinsic instability of hybrid halide perovskite structures can be captured at the level of first-principle calculations[11,15,67] by evaluating the enthalpy of the reaction

$$AX + BX_2 \rightarrow ABX_3 \tag{4.1.1}$$

based on the total energy of the solid compounds involved. Here $A$ represents an organic cation, $B$ and $X$ are the metal and halide elements, respectively. The negative reaction enthalpy $\Delta H_\mathrm{r}$ indicates stable products. The lower the value of $\Delta H_\mathrm{r}$, the more stable the structure is against decomposition. For example, the reaction enthalpy for tetragonal $CH_3NH_3PbI_3$ is within the range of $-0.1 \ldots 0.06$ eV per formula unit[3,61,67], which renders the structure to be at the boundary between weakly stable and unstable agreeing with experimental observations[3]. Despite the success of first-principle calculations in predicting the formability of hybrid halide perovskite structures, the origin of intrinsic instability and

avenues for its improvement remain unclear.

Geometrical factors such as the Goldschmidt's tolerance factor[19] and octahedral factor successfully explain formability of various inorganic perovskite structures[37]. The tolerance factor $t$ measures compactness of the perovskite structure. The value of the tolerance factor for $CH_3NH_3PbI_3$ is $t = 0.91$[45], which is within the range of acceptable values $t = 0.8{-}0.95$[37]. Li et al.[37] pointed out that the tolerance factor alone does not fully capture formability of perovskite structures and proposed to add Pauling's octahedral factor[50] $r_B/r_X$ ($r_B$ and $r_X$ are the ionic radii of cation $B$ and anion $X$, respectively) as an additional geometrical criterion. In the case of $CH_3NH_3PbI_3$ the octahedral factor $r_{\mathrm{Pb}}/r_{\mathrm{I}} = 0.54$ is within the allowable range of $0.414 - 0.732$[50]. This analysis suggests that geometrical factors are not sufficient to explain the instability of hybrid halide perovskites.

Frost et al.[13] attributed the instability of hybrid organic halide perovskites to a relatively low electrostatic lattice energy of their ionic structure as compared to non-halide perovskite compounds. For instance, traditional inorganic perovskites of the $\mathrm{II}{-}\mathrm{IV}{-}\mathrm{VI}_3$ family, e.g. $PbTiO_3$, have the lattice energy of $-119$ eV. This value is much lower than the lattice energy of $-28$ eV for $CH_3NH_3PbI_3$ perovskite, which belongs to the $\mathrm{I}{-}\mathrm{II}{-}\mathrm{VII}_3$ family. This argument suggests that $\mathrm{I}{-}\mathrm{II}{-}\mathrm{VII}_3$ perovskites have intrinsically lower electrostatic energy and thus weaker chemical stability. On the other hand, the experimental reaction enthalpy for $PbTiO_3$ is only $-0.38$ eV[53], which is orders of magnitude less than its lattice energy. It is also known that $CsPbI_3$ perovskite structure is indeed stable up to the temperature of 460°C[56], above which the material melts without decomposition, despite of its higher lattice energy of $-27$ eV. These observations indicate that the lattice energy alone cannot be used as a criterion for the stability of ionic structures.

The Born-Haber cycle is traditionally used for the analysis of formation enthalpies. It allows to break the formation energy into the following components: atomization enthalpy, ionization enthalpy, and lattice enthalpy[62]. In this paper, we extend the Born-Haber cycle to the analysis of energy components of the reaction enthalpies for various perovskite

structures using the density functional theory (DFT). It will be shown that in I−II−$VII_3$ organic and inorganic perovskites the lattice energy contribution is largely cancelled by the molecularization energy leaving the ionization enthalpy to determine the direction of the reaction. The instability of hybrid organic lead-iodine perovskites can be attributed to the high energy associated with ionization of organic molecules and $[PbI_3]^-$.

## 4.2 Methods

### 4.2.1 Basic concepts

The Born-Haber cycle was originally proposed by Max Born and Fritz Haber as a way to measure formation energies of ionic structures[62]. The cycle also provides a method to determine the lattice energy of the structures, which otherwise cannot be directly measured experimentally. Here we will explain the essence of the Born-Haber cycle and its utilization for analysis of reaction enthalpy components using the $CH_3NH_3PbI_3$ perovskite structure as an example.

The formation process of $CH_3NH_3PbI_3$ from solid $CH_3NH_3I$ and $PbI_2$ compounds can be subdivided into several consecutive steps illustrated in Fig. 4.1. The initial step—molecularization (similar to the atomization in the original Born-Haber cycle)—involves breaking the $CH_3NH_3I$ and $PbI_2$ lattice structures and formation of $CH_3NH_3$ and $PbI_3$ molecules

$$CH_3NH_3I(s) + PbI_2(s) \xrightarrow{\Delta H_{mo}} CH_3NH_3(g) + PbI_3(g) \ . \tag{4.2.1}$$

The rational for using $CH_3NH_3$ and $PbI_3$ radicals as the smallest units in the Born-Haber cycle is justified by the existence of the corresponding free standing ions[6,28,35,39], and will be discussed in the next section.

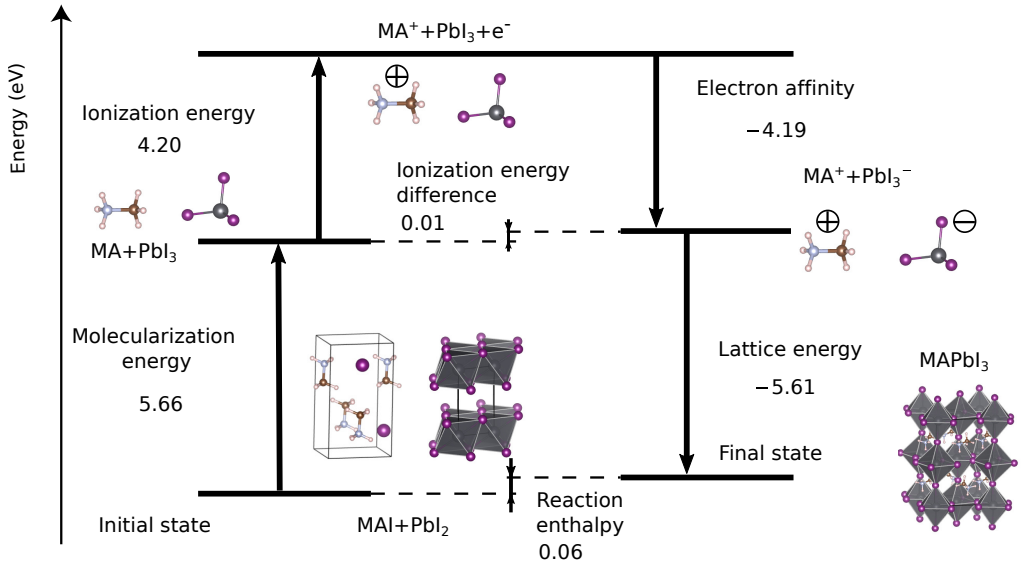


Figure 4.1: Born-Haber cycle of methylammonium (MA) lead iodide obtained with $[CH_3NH_3]^+$ and $[PbI_3]^-$ ions as elementary species.

The next step is the ionization of $CH_3NH_3$ molecule

$$CH_3NH_3(g) + PbI_3(g) \xrightarrow{\Delta H_{\text{ion},1}} CH_3NH_3^+(g) + PbI_3(g) + e^- \ , \tag{4.2.2}$$

followed by the ionization of $PbI_3$

$$CH_3NH_3^+(g) + PbI_3(g) + e^- \xrightarrow{\Delta H_{\text{ion},2}} CH_3NH_3^+(g) + PbI_3^-(g) \ . \tag{4.2.3}$$

It can be seen from the diagram in Fig. 4.1 that the formation of $[CH_3NH_3]^+$ ion is an endothermic process, whereas the ionization of $PbI_3$ is an exothermic process. The resultant ionization energy is an additive of two enthalphies

$$\Delta H_{\text{ion}} = \Delta H_{\text{ion},1} + \Delta H_{\text{ion},2} \ . \tag{4.2.4}$$

Finally, electrically charged $[CH_3NH_3]^+$ and $[PbI_3]^-$ complex ions are combined to form

$CH_3NH_3PbI_3$ crystalline structure

$$CH_3NH_3^+(g) + PbI_3^-(g) \xrightarrow{\Delta H_{\text{latt}}} CH_3NH_3PbI_3(s) \ . \tag{4.2.5}$$

The amount of energy $\Delta H_{\text{latt}}$ released in this reaction is called the lattice energy of the hybrid organic perovskite structure. This concludes the Born-Haber cycle of $CH_3NH_3PbI_3$. The total reaction enthalpy is compiled from enthalpies of individual steps of the cycle

$$\Delta H_{\text{r}} = \Delta H_{\text{mo}} + \Delta H_{\text{ion}} + \Delta H_{\text{latt}} \ . \tag{4.2.6}$$

### 4.2.2 Computational details

Electronic structure calculations have been performed in the framework of DFT[32] and Perdew-Burke-Ernzerhof generalized gradient approximation[51] (PBE-GGA) for the exchange-correlation functional. Total energies of all compounds were obtained using the Vienna *ab initio* simulation program (VASP) and projector augmented-wave (PAW) potentials[2,33,34].

All crystal structures of compounds studied here are taken at their most stable polymorph at ambient conditions. Among perovskite structures, $CH_3NH_3PbI_3$ adopts a tetragonal $\beta$-phase at the ambient temperature, $CH_3NH_3PbBr_3$ and $CH_3NH_3PbCl_3$ have a cubic phase[47,52], $C(NH_2)_3PbI_3$ and $(CH_3)_4NPbI_3$ favour hexagonal structures[9,18,38]. $HC(NH_2)_2PbI_3$ adopts a hexagonal $\delta$-phase[57]. $CsPbI_3$, $CsPbBr_3$, and $CsPbCl_3$ prefer an orthorhombic (Pnma) $\delta$-phase[24,56]. The crystal structure of $CH_3NH_3I$, $CH_3NH_3Br$, and $CH_3NH_3Cl$ organic salts correspond to $\alpha'$-tetragonal (P4/nmm) phase at room temperature[14,25,27]. Szafrański and Jarek[60] reported the structures of guanidinium iodide $C(NH_2)_3I$, and the structure of tetramethylammonium iodine $(CH_3)_4NI$ was obtained using $(CH_3)_4NAu$[7] as a parent structure followed by full relaxation of their structural parameters. The structure of $HC(NH_2)_2I$ was obtained from orthorhombic (Pbca) $C(NH_2)_3Cl$[22] with full relaxation of the structural parameters. Cubic crystal structures of CsI, CsBr, CsCl and NaCl as

well as hexagonal $PbI_2$ and orthorhombic $PbBr_2$ were taken from Gerlach[17], Graystone and Wyckoff[21]. The crystal structure of orthorhombic $PbCl_2$ was derived from the structure of $PbBr_2$.

For reciprocal space integration, $4 \times 4 \times 4$ Monkhorst-Pack grid[43] was used for cubic phases, $3 \times 3 \times 2$ were used for tetragonal phases, $4 \times 4 \times 3$ for hexagonal phases and $3 \times 6 \times 2$ for orthorhombic $CsPbX_3$ phases and $4 \times 8 \times 4$ for orthorhombic $PbBr_2$ and $PbCl_2$. The convergence of reaction enthalpies with respect to the k-mesh density is better than 5 meV, which was tested by doubling the density for several perovskite structures and their parent compounds. The cutoff energy for a plane wave expansion was set at 400 eV. The lattice constant and atomic positions were optimized such that residual forces acting on atoms did not exceed 2 meV/Å, and the residual hydrostatic pressure was less than 50 MPa.

Gaseous phases, such as Cs, $[CH_3NH_3]^+$, $[PbI_3]^-$, were modelled as an individual atom/molecule surrounded by 20 Å of vacuum. All calculations related to gaseous phases were performed in conjunction with the optimization of internal degrees of freedom. Only Γ-point was used in the Brillouin zone. The ionization energy of positively charged ions was calculated by subtracting the total energy of cations (e.g. $Cs^+$, $[CH_3NH_3]^+$, $[C(NH_2)_3]^+$) from the energy of neutral atoms or molecules (e.g. Cs, $CH_3NH_3$, $C(NH_2)_3$). Similarly, the electron affinity of negatively charged ions was modelled by adding one electron to $PbCl_3$, $PbBr_3$, or $PbI_3$ molecules to form $[PbCl_3]^-$, $[PbBr_3]^-$, and $[PbI_3]^-$ anions. The electron affinity of these ions was represented as an energy difference between negatively charged complex ions and neutral species. Monopole, dipole and quadrupole corrections implemented in VASP[40,46] were used for eliminating leading errors and acquiring accurate total energies of all charged ions.

VESTA 3 package[42] was used to visualize crystal structures and for computing the Madelung electrostatic energy using an oxidation state as formal charges. In these calculations, the radius of the ionic sphere and the reciprocal-space range were set at 1 Å and 4 $Å^{-1}$, respectively.

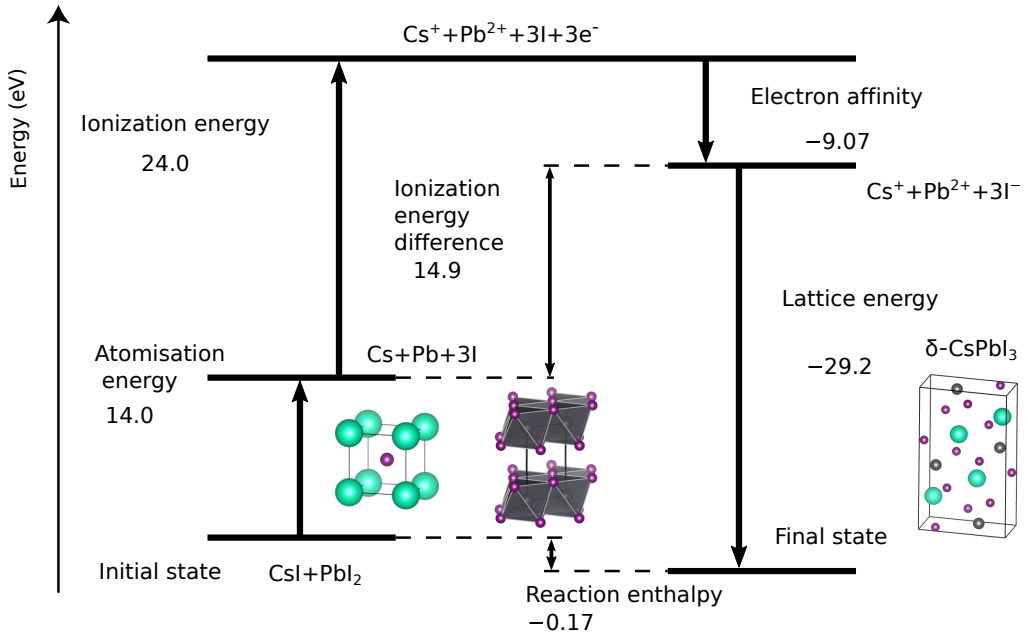


Figure 4.2: Born-Haber cycle of caesium lead iodide obtained with $Cs^+$, $Pb^{2+}$, and $I^-$ ions as elementary species.

## 4.3 Results and discussion

### 4.3.1 Lattice energies of halide perovskites

Calculation of individual energies associated with various steps in the Born-Haber cycle requires subdivision of the ionic solid in question into elementary species. In the case of alkali halides (such as NaCl, CsCl, etc.), the atomization is an apparent choice. Following the same strategy, $Cs^+$, $Pb^{2+}$, and $I^-$ ions can be used to calculate the lattice energy, which yields $\Delta H_{\text{latt}} \simeq -29$ eV (Fig. 4.2).

This value agrees well with the Madelung energy of $-27$ eV obtained from the point charge model. Gopal[20] noticed existence of a trend between the lattice energy $\Delta H_{\text{latt}}$ and the melting point $T_m$ of alkali halides with the proportionality factor of $-\Delta H_{\text{latt}}/T_m \approx 7.4 \cdot 10^{-3}$ eV/K. Assuming that the same proportionality holds for perovskite structures, the melting point of $\text{I}-\text{II}-\text{VII}_3$ perovskites would be near 3900 K, which is an order of

magnitude greater than the actual values of $733-888$ K for group-I lead halide perovskites ($CsPbI_3$, $CsPbBr_3$, and $CsPbCl_3$)[12,58].

Alternatively, we can separate $CsPbI_3$ perovskite structure into two ions $Cs^+$ and $[PbI_3]^-$. The existence of the corresponding free-standing ions was verified experimentally[6,35]. Using this approach we re-evaluated the lattice energy of $CsPbI_3$ as $-5.55$ eV using the Born-Haber cycle similar to that shown in Fig. 4.1. This result translates into a substantially lower melting point of approximately 750 K, which is remarkably close to the experimental value of 749 K.

Similar calculations of the lattice energy were performed for other inorganic $I-II-VII_3$ and $II-IV-VI_3$ perovskites. Results are summarized in Table 4.1. NaCl was used as a benchmark for comparison between calculated and experimental components of the formation enthalpy. The agreement with experimental values gives confidence in the approach used. The discrepancy in $\Delta H_{\mathrm{mo}}$ can be attributed to the use of non-spin-polarized calculations for individual atoms and ions. The plot of the melting point *vs* the lattice energy of those compounds is shown in Fig. 4.3. From this figure, we can see that the melting point of different ionic structures including alkali halides follows a linear trend line. The finding suggests that the formation of $A^+$ cations and $[BX_3]^-$ complex anions is a plausible scenario during melting of the perovskite structures.

### 4.3.2 Stability analysis of hybrid organic halide perovskites

Now we will utilize the Born-Haber cycle in order to evaluate components of the reaction enthalpy of hybrid halide perovskites. The lattice energies of $CH_3NH_3PbCl_3$, $CH_3NH_3PbBr_3$ and $\beta$-$CH_3NH_3PbI_3$ perovskites are listed in Table 4.1. All three compounds have similar values of the lattice energies ($\sim$10% max-min difference). However, their stability characteristics are quite different. Buin et al.[3] demonstrated that under ambient conditions $CH_3NH_3PbCl_3$ and $CH_3NH_3PbBr_3$ do not undergo a spontaneous phase separation, unlike

Table 4.1: Components (eV) of the reaction enthalpies extracted from Born-Haber cycle as well as the melting temperature and stability against spontaneous decomposition for halide perovskites and other ionic structures.

| Compounds | $\Delta H_{\mathrm{mo}}$ | $\Delta H_{\mathrm{latt}}$ | $\Delta H_{\mathrm{ion}}$ | $\Delta H_{\mathrm{r}}$ | $T_{\mathrm{m}}$ (K) | Stability[a] |
|---|---|---|---|---|---|---|
| $\delta$-$CsPbCl_3$ | 6.23 | −5.95 | −0.67 | −0.39 | 888[12] | Y[56] |
| $\delta$-$CsPbBr_3$ | 5.80 | −5.72 | −0.46 | −0.39 | 840[58] | Y[56] |
| $\delta$-$CsPbI_3$ | 5.72 | −5.55 | −0.34 | −0.17 | 749[56] | Y[56] |
| $CH_3NH_3PbCl_3$ | 6.20 | −6.03 | −0.32 | −0.15 | ··· | Y[3] |
| $CH_3NH_3PbBr_3$ | 5.80 | −5.81 | −0.11 | −0.11 | ··· | Y[3] |
| $\beta$-$CH_3NH_3PbI_3$ | 5.66 | −5.61 | 0.01 | 0.06 | ··· | N[3] |
| $\delta$-$HC(NH_2)_2PbI_3$ | 5.40 | −5.39 | −0.23 | −0.21 | ··· | Y[57] |
| $C(NH_2)_3PbI_3$ | 5.43 | −5.43 | −0.38 | −0.39 | ··· | Y[9] |
| $(CH_3)_4NPbI_3$ | 5.47 | −4.79 | −1.05 | −0.37 | ··· | Y[38] |
| CsCl | 2.59 | −6.64 | 0.14 | −3.91 | 918[29] | Y |
| NaCl[b] | 3.01 | −8.22 | 1.46 | −3.76 | 1077[26] | Y |

[a] Stability data here are from experiments: "Y" refers to materials that do not undergo spontaneous phase separation at the room temperature (excluding environmental factors, such as moisture water, oxygen, UV light); [b] Experimental values for NaCl[62]: $\Delta H_{\mathrm{mo}} = 2.37$ eV, $\Delta H_{\mathrm{latt}} = -8.15$ eV, $\Delta H_{\mathrm{ion}} = 1.52$ eV, $\Delta H_{\mathrm{r}} = -4.26$ eV.

$\beta$-$CH_3NH_3PbI_3$. Both $CH_3NH_3PbCl_3$ and $CH_3NH_3PbBr_3$ remain stable up to the temperature of approximately 520 K, above which they decompose[45]. Lattice energies of the corresponding inorganic perovskites ($CsPbI_3$, $CsPbBr_3$ and $CsPbCl_3$) are very similar to their organic counterparts. In fact, these inorganic perovskites are chemically stable under the ambient environment. Remarkably, the lattice energy of $\beta$-$CH_3NH_3PbI_3$ and $\delta$-$CsPbCl_3$ structures are identical, in spite of the distinct stability characteristics. Therefore, we can conclude that the lattice energy cannot be used as a criteria to predict the chemical stability of compounds.

The analysis of various contributions to the reaction enthalpies of hybrid halide perovskites (Table 4.1) shows that the molecularization and lattice energies largely cancel each other. The molecularization energy in reaction (4.2.1) is largely governed by the methylammonium iodide bond strength as evident from Fig. 4.4. The energy consumed to separate $PbI_2$(s) to $PbI_2$(g) and the energy gained from adding I-atom to $PbI_2$(g) to form $PbI_3$(g) roughly cancel each other. We estimated the Madelung energy of $CH_3NH_3I$ to be

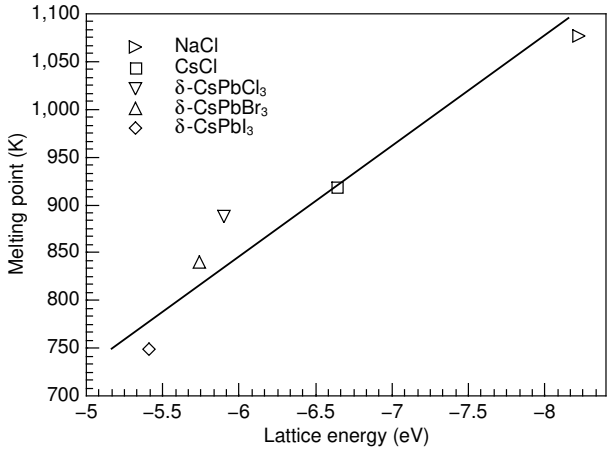


Figure 4.3: Correlation between the lattice energy and melting temperature of ionic compounds. The line is a guide to the eye.

$-6.8$ eV/f.u. by placing $+1e$ and $-1e$ on the nitrogen and iodine atoms, respectively. This lattice energy of $CH_3NH_3I$ includes $-1$ eV/f.u. associated with the ionization energy of $I^-$ and $[CH_3NH_3]^+$. Therefore, the lattice energy of $CH_3NH_3PbI_3$ $-5.61$ eV/f.u. is inherited from the lattice energy of the parent salt, $CH_3NH_3I$.

The ionization energy of $[CH_3NH_3]^+$ and $[PbI_3]^-$ is the remaining contribution to the reaction enthalpy in Eq. (4.2.6) that ultimately controls the balance of the reaction. The lower $\Delta H_{\text{ion}}$ is, the more stable the compound.

Let us examine the chemical trends in ionization energy of various perovskites. The total ionization energy (Eq. 4.2.4) comprises of two components: the ionization energy for the cation ($Cs^+$ or $[CH_3NH_3]^+$) and that for the complex ion ($[PbI_3]^-$, $[PbBr_3]^-$, or $[PbCl_3]^-$). Caesium has a lower ionization energy than $CH_3NH_3$ (Table 4.2), which explains trends in the higher chemical stability of Cs-based perovskites as compared to their $CH_3NH_3$-based counterparts.

Switching halides in the complex ions from $PbI_3$ to $PbCl_3$ lowers their electron affinity (Table 4.2) and, thus, leads to the lower total ionization energy. This explains increase of the chemical stability when changing the inorganic cage from $PbI_3$ to $PbBr_3$ and $PbCl_3$ as

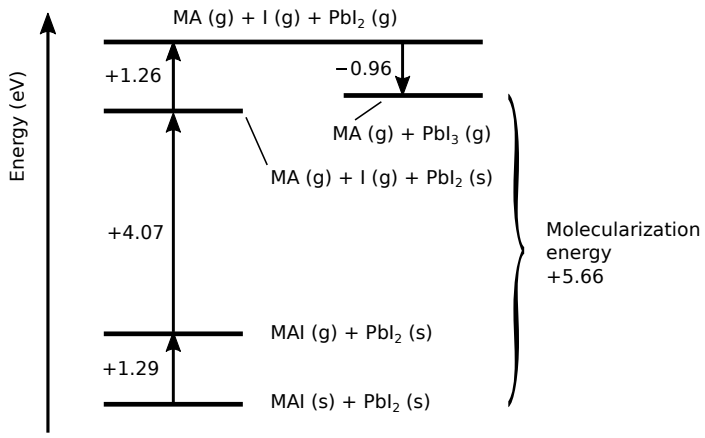


Figure 4.4: Components of the molecularization energy in the reaction (4.2.1).

illustrated in Fig. 4.5.

In order to achieve a chemically stable hybrid halide perovskite structures, the requirements are favourable geometrical factors (t-factor and octahedral factor) in conjunction with the low ionization energy ($\Delta H_{\text{ion}} \lesssim 0$ eV). Two strategies can be used to achieve this goal: (i) find a cation with the low ionization energy or (ii) select an inorganic cage with the low electron affinity. The second avenue is not very promising, since the band gap of $PbBr_3$- and $PbCl_3$-based hybrid perovskites (2.3 eV[55] and 2.9 eV[8], respectively) is outside of the favourable range for single-junction solar cells.

Since caesium has the lowest ionization energy in the periodic table, it is a challenging task to find molecules with smaller or similar ionization energy. Among the variety of organic cations listed in the Table 4.2, $[C(NH_2)_3]^+$, $[HC(NH_2)_2]^+$, and $[(CH_3)_4N]^+$ have the ionization energies lower than that for $[CH_3NH_3]^+$ cation making them favourable candidates for perovskites with improved stability. However, the size of $C(NH_2)_3$, $HC(NH_2)_2$, and $(CH_3)_4N$ molecules is significantly greater than $CH_3NH_3$, which raises the tolerance factor above the upper formability limit of 0.95 (Table 4.3).

The structures $C(NH_2)_3PbI_3$, $HC(NH_2)_2PbI_3$, and $(CH_3)_4NPbI_3$ show favourable reaction enthalpies of $-0.39$ eV, $-0.21$ ev, and $-0.37$ eV, respectively (Table 4.1). A large

Table 4.2: Ionization energies (eV) of atoms and molecules calculated with DFT. Lower values favour formability of perovskites.

| Ions | $\Delta H_{\mathrm{ion},1/2}$ |
|---|---|
| $[(CH_3)_4N]^+$ | 3.15 |
| $[C(NH_2)_3]^+$ | 3.81 |
| $Cs^+$ | 3.85 |
| $[HC(NH_2)_2]^+$ | 3.97 |
| $[CH_3NH_3]^+$ | 4.20 |
| $[NH_4]^+$ | 4.78 |
| $Na^+$ | 5.17[a] |
| $[CH_3PH_3]^+$ | 5.20 |
| $[CH_3SH_2]^+$ | 5.30 |
| $[PH_4]^+$ | 5.36 |
| $[HCNH_2PH_2]^+$ | 8.36 |
| $[CH_3]^+$ | 10.0[b] |
| $[PbCl_3]^-$ | −4.52 |
| $[PbBr_3]^-$ | −4.31 |
| $[PbI_3]^-$ | −4.19 |

[a] 5.20 eV experimental ionization energy[62]. [b] 9.84 eV experimental ionization energy[1,54].

Table 4.3: Size of organic cations, the tolerance factor, volume of the unit cell and the band gap of selected perovskites.

| Perovskite | Cation radius (pm) | Tolerance factor[31,38] | Volume ($Å^3$/f.u.) | Band gap (eV) |
|---|---|---|---|---|
| $\beta$-$CH_3NH_3PbI_3$ | 217[31,38] | 0.91 | 262 | 1.62 |
| $\delta$-$HC(NH_2)_2PbI_3$ | 253[38] | 0.99 | 264 | 2.87 |
| $C(NH_2)_3PbI_3$ | 278[31,38] | 1.04 | 326 | 3.38 |
| $(CH_3)_4NPbI_3$ | 320[16,48] | 1.15 | 361 | 3.30 |

size of the organic molecule hinders formability of $C(NH_2)_3PbI_3$, $HC(NH_2)_2PbI_3$, and $(CH_3)_4NPbI_3$ perovskite structures on the cubic or tetragonal phases. They all adopt a hexagonal structure at ambient temperature[9,38,57]. However, this phase tends to have a wider band gap, which impairs its prospects for use in photovoltaic applications. Nevertheless, we discuss the link between our calculations and experimental evidences for stability of $C(NH_2)_3PbI_3$, $HC(NH_2)_2PbI_3$, and $(CH_3)_4NPbI_3$compounds.

Marco et al.[41] successfully synthesized and characterized $C(NH_2)_3PbI_3$ perovskite solar

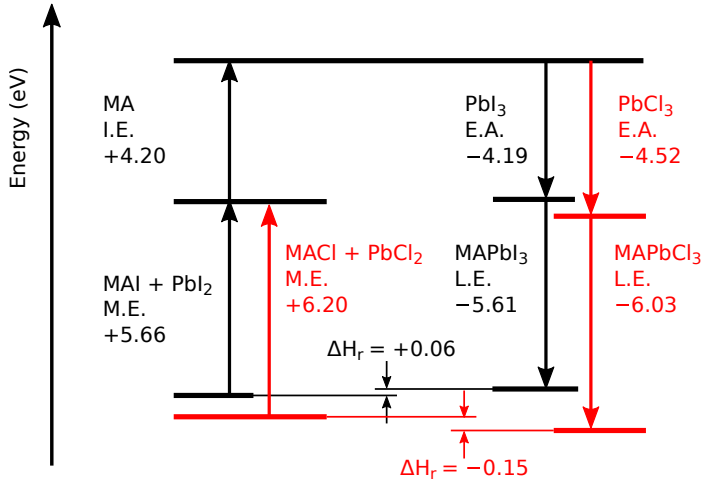


Figure 4.5: The influence of halide element on the Born-Haber cycle of hybrid halide perovskites. A comparison between $CH_3NH_3PbI_3$ and $CH_3NH_3PbCl_3$. The following components are shown: the molecularization energy (M.E.), the ionization energy (I.E.), the electron affinity (E.A.), and the lattice energy (L.E.).

cells. It was found that the power conversion efficiency of $C(NH_2)_3PbI_3$ solar cell degrades over time. Interestingly, the rate of the efficiency decay is slower for $C(NH_2)_3PbI_3$ as compared to $CH_3NH_3PbI_3$. Szafrański[59] observed that $C(NH_2)_3PbI_3$ crystals transform from the orange-reddish phase to the yellow phase after several hours at ambient pressure and temperature. The optical bleaching is associated with a phase transformation that yields the hexagonal phase rather than the phase separation[59]. $HC(NH_2)_2PbI_3$ prefers a cubic phase at the high temperature (160°C), and takes a hexagonal phase at the ambient temperature[57,63].

The question is if there are any organic cations of the suitable size that fulfill the requirements on the low ionization energy? The ionization energies of onium ions in Table 4.2 correlate with the proton affinity of the corresponding molecules[10]. Molecules with the low ionization energy exhibit strong proton affinity and *vice versa*. For instance, the proton affinity of $PH_3$ is 785 kJ/mol, which is much lower than 901 kJ/mol for $CH_3NH_2$. It turns out that methylamine has one of the strongest proton affinity among organic compounds. There very few organic molecules (including $(CH_3)_2NH$ studied here) with stronger proton

affinity than $CH_3NH_2$, but none of them have a size compatible with the $PbI_3$ cage.

## 4.4 Conclusions

The Goldschmidt's tolerance and octahedral geometrical factors do not fully capture prerequisites for the formability of hybrid halide perovskites. Here we used DFT calculations in conjunction with a Born-Haber cycle to evaluate contributions of the lattice, ionization and molecularization energies to the decomposition reaction enthalpy of hybrid halide perovskites. It was previously assumed that the instability of halide perovskite is due to lower lattice energy of their ionic structure. We observe a correlation between the lattice energies and melting temperatures, but not with reaction enthalpies that are ultimately linked to the chemical instability of the perovskites. Analysis of Born-Haber cycle components suggests that the reaction enthalpy of hybrid halide perovskites is governed by the sum of ionization energies of a cation, e.g., $[CH_3NH_3]^+$, and an anion, e.g., $[PbI_3]^-$. The lower total ionization energy, the more stable is the structure, provided the geometrical conditions are fulfilled (the tolerance and octahedral factors). This explains chemical trends in stability of hybrid and inorganic halide perovskites. For instance, the relatively high stability of $CH_3NH_3PbCl_3$ is attributed to a lower ionization energy of $[PbCl_3]^-$ complex ion, whereas the stability of $CsPbI_3$ is due to the lower ionization energy of $Cs^+$. The ionization energy of organic cations correlates with their proton affinity. In the search for hybrid perovskite with improved chemical stability and the band gap suitable for photovoltaic applications, several cations were investigated. The promising candidates are $[C(NH_2)_3]^+$, $[HC(NH_2)_2]^+$, and $[(CH_3)_4N]^+$ with the ionization energies even lower than $Cs^+$. The corresponding $C(NH_2)_3PbI_3$, $HC(NH_2)_2PbI_3$, and $(CH_3)_4NPbI_3$ structures have the decomposition reaction enthalpy of at least 0.27 eV more favourable than $CH_3NH_3PbI_3$. However, these ions have a prohibitively large size and thus prefer a hexagonal structure that translates into a large band gap. It is the fact that $CH_3NH_2$ has the highest proton affinity among molecules

of comparable size that makes it challenging to find a cation suitable for the $PbI_3$ cage.

Our calculations do not include environmental factors, such as degradation in water or oxidation in air. However, the reaction enthalpy determines a saturation concentration of $[CH_3NH_3]^+$ ions during dissolution of $CH_3NH_3PbI_3$ in water[61]. Therefore, improvement in the reaction enthalpy will also enhance the stability of perovskite structures in the moist environment.

# Bibliography

[1] J. Berkowitz, G. B. Ellison, and D. Gutman. Three methods to measure RH bond energies. *J. Phys. Chem.*, 98(11):2744–2765, 1994.

[2] P. Blöchl. Projector augmented-wave method. *Phys. Rev. B*, 50(24):17953, 1994.

[3] A. Buin, R. Comin, J. Xu, A. H. Ip, and E. H. Sargent. Halide-dependent electronic structure of organolead perovskite materials. *Chem. Mater.*, 27(12):4405–4412, 2015. doi: 10.1021/acs.chemmater.5b01909.

[4] J. Burschka, N. Pellet, S.-J. Moon, R. Humphry-Baker, P. Gao, M. K. Nazeeruddin, and M. Grätzel. Sequential deposition as a route to high-performance perovskite-sensitized solar cells. *Nature*, 499(7458):316–319, 2013. doi: 10.1038/nature12340.

[5] J. A. Christians, P. A. M. Herrera, and P. V. Kamat. Transformation of the excited state and photovoltaic efficiency of $CH_3NH_3PbI_3$ perovskite upon controlled exposure to humidified air. *J. Am. Chem. Soc.*, 137(4):1530–1538, 2015. doi: 10.1021/ja511132a.

[6] P. Cremaschi and M. Simonetta. Barmer to internal rotation in the methylammonium ion. *J. Mol. Struct.*, 29(1):39–45, 1975. doi: 10.1016/0022-2860(75)88005-7.

[7] P. D. Dietzel and M. Jansen. Synthesis and crystal structure determination of tetramethylammonium auride. *Chem. Commun.*, (21):2208–2209, 2001. doi: 10.1039/B105648B.

[8] L. Dimesso, M. Dimamay, M. Hamburger, and W. Jaegermann. Properties of $CH_3NH_3PbX_3$ (X= I, Br, Cl) powders as precursors for organic/inorganic solar cells. *Chem. Mater.*, 26(23):6762–6770, 2014. doi: 10.1021/cm503240k.

[9] L. Dimesso, A. Quintilla, Y.-M. Kim, U. Lemmer, and W. Jaegermann. Investigation of formamidinium and guanidinium lead tri-iodide powders as precursors for solar cells.

*Materials Science and Engineering: B*, 204:27–33, 2016. doi: 10.1016/j.mseb.2015.11.006.

[10] A. L. East, B. J. Smith, and L. Radom. Entropies and free energies of protonation and proton-transfer reactions. *J. Am. Chem. Soc.*, 119(38):9014–9020, 1997. doi: 10.1021/ja970891j.

[11] F. El-Mellouhi, E. T. Bentria, S. N. Rashkeev, S. Kais, and F. H. Alharbi. Enhancing intrinsic stability of hybrid perovskite solar cell by strong, yet balanced, electronic coupling. *Sci. Rep.*, 6:30305, 2016. doi: 10.1038/srep30305.

[12] F. Fayon, Y. Vaills, P. Simon, P. Echegut, C. Bessada, J. Emery, and J.-Y. Buzare. Study of $CsPbCl_3$ between T= 47°C and the melting point by the $^{133}Cs$ NMR and [$Gd_3{}^+$] EPR measurements. *Ferroelectrics*, 185(1):201–204, 1996.

[13] J. M. Frost, K. T. Butler, F. Brivio, C. H. Hendon, M. Van Schilfgaarde, and A. Walsh. Atomistic origins of high-performance in hybrid halide perovskite solar cells. *Nano Lett.*, 14(5):2584–2590, 2014. doi: 10.1021/nl500390f.

[14] E. J. Gabe. The crystal structure of methylammonium chloride. *Acta Cryst.*, 14(10): 1296–1296, 1961. doi: 10.1021/ja01214a029.

[15] A. M. Ganose, C. N. Savory, and D. O. Scanlon. $(CH_3NH_3)_2Pb(SCN)_2I_2$: A more stable structural motif for hybrid halide photovoltaics? *J. Phys. Chem. Lett.*, 6(22): 4594–4598, 2015. doi: 10.1021/acs.jpclett.5b02177.

[16] S. Garde, G. Hummer, and M. E. Paulaitis. Free energy of hydration of a molecular ionic solute: Tetramethylammonium ion. *J. Chem. Phys.*, 108(4):1552–1561, 1998. doi: 10.1063/1.475526.

[17] W. Gerlach. Die gitterstruktur der erdalkalioxyde. *Z. Phys. A-Hadron. Nucl.*, 9(1): 184–192, 1922.

[18] G. Giorgi, J.-I. Fujisawa, H. Segawa, and K. Yamashita. Organic–inorganic hybrid lead iodide perovskite featuring zero dipole moment guanidinium cations: a theoretical analysis. *J. Phys. Chem. C*, 119(9):4694–4701, 2015. doi: 10.1021/acs.jpcc.5b00051.

[19] V. M. Goldschmidt. Die gesetze der krystallochemie. *Naturwissenschaften*, 14(21): 477–485, 1926. doi: 10.1007/BF01507527.

[20] R. Gopal. Relation between the lattice energy, melting point, and boiling point of some crystalline substances. I. alkali halides. *J. Indian Chem. Soc.*, 30(55):55–58, 1953.

[21] R. W. Graystone and Wyckoff. *Crystal Structures*, volume 2. Interscience New York, 1960.

[22] D. Haas, D. Harris, and H. Mills. The crystal structure of guanidinium chloride. *Acta Cryst.*, 19(4):676–679, 1965. doi: 10.1107/S0365110X65004085.

[23] Y. Han, S. Meyer, Y. Dkhissi, K. Weber, J. M. Pringle, U. Bach, L. Spiccia, and Y.-B. Cheng. Degradation observations of encapsulated planar $CH_3NH_3PbI_3$ perovskite solar cells at high temperatures and humidity. *J. Mater. Chem. A*, 3(15):8139–8147, 2015. doi: 10.1039/C5TA00358J.

[24] M. Hidaka, Y. Okamoto, and Y. Zikumaru. Structural phase transition of $CsPbCl_3$ below room temperature. *Phys. Status. Solidi. A*, 79(1):263–269, 1983. doi: 10.1002/pssa.2210790129.

[25] E. W. Hughes and W. N. Lipscomb. The crystal structure of methylammonium chloride. *J. Am. Chem. Soc.*, 68(10):1970–1975, 1946. doi: 10.1021/ja01214a029.

[26] L. Hunter. The variation with temperature of the principal elastic moduli of NaCl near the melting point. *Phys. Rev.*, 61(1-2):84, 1942. doi: 10.1103/PhysRev.61.84.

[27] H. Ishida, H. Maeda, A. Hirano, T. Fujimoto, Y. Kubozono, S. Kashino, and S. Emura. Exafs study on the phase transition (phase $\alpha$'–$\delta$) in $CH_3NH_3I$. *Z. Naturforsch. A.*, 50 (9):876–880, 1995.

[28] S.-J. JEON, A. B. Raksit, G. I. Gellene, and R. F. Porter. Formation of hypervalent ammoniated radicals by neutralized ion beam techniques. *Journal of the American Chemical Society*, 107(14):4129–4133, 1985. doi: 10.1021/ja00300a006.

[29] J. Johnson, P. Agron, and M. Bredig. Molar volume and structure of solid and molten caesium halides. *J. Am. Chem. Soc.*, 77(10):2734–2737, 1955. doi: 10.1021/ja01615a015.

[30] H. S. Jung and N.-G. Park. Perovskite solar cells: From materials to devices. *Small*, 11(1):10–25, 2015. doi: 10.1002/smll.201402767.

[31] G. Kieslich, S. Sun, and A. K. Cheetham. Solid-state principles applied to organic–inorganic perovskites: New tricks for an old dog. *Chem. Sci.*, 5(12):4712–4715, 2014. doi: 10.1039/C4SC02211D.

[32] W. Kohn and L. J. Sham. Self-consistent equations including exchange and correlation effects. *Phys. Rev.*, 140(4A):A1133, 1965. doi: 10.1103/PhysRev.140.A1133.

[33] G. Kresse and J. Furthmüller. Efficient iterative schemes for ab initio total-energy calculations using a plane-wave basis set. *Phys. Rev. B*, 54(16):11169, 1996.

[34] G. Kresse and D. Joubert. From ultrasoft pseudopotentials to the projector augmented-wave method. *Phys. Rev. B*, 59(3):1758, 1999.

[35] O. E. Lanford and S. J. Kiehl. The solubility of lead iodide in solutions of potassium iodide-complex lead iodide ions. *J. Am. Chem. Soc.*, 63(3):667–669, 1941. doi: 110.1021/ja01848a010.

[36] M. M. Lee, J. Teuscher, T. Miyasaka, T. N. Murakami, and H. J. Snaith. Efficient hybrid solar cells based on meso-superstructured organometal halide perovskites. *Science*, 338(6107):643–647, 2012. doi: 10.1126/science.1228604.

[37] C. Li, K. C. K. Soh, and P. Wu. Formability of $ABO_3$ perovskites. *J. Alloy. Compd.*, 372(1):40–48, 2004. doi: 10.1016/j.jallcom.2003.10.017.

[38] G. Liu, J. Liu, Z. Sun, Z. Zhang, L. Chang, J. Wang, X. Tao, and Q. Zhang. Thermally induced reversible double phase transitions in an organic–inorganic hybrid iodoplumbate $C_4H_{12}NPbI_3$ with symmetry breaking. *Inorg. Chem.*, 55(16):8025–8030, 2016. doi: 10.1021/acs.inorgchem.6b01143.

[39] Y.-R. Luo. *Comprehensive handbook of chemical bond energies*. CRC press, 2007.

[40] G. Makov and M. C. Payne. Periodic boundary conditions in *Ab Initio* calculations. *Phys. Rev. B*, 51:4014–4022, Feb 1995. doi: 10.1103/PhysRevB.51.4014.

[41] N. D. Marco, H. Zhou, Q. Chen, P. Sun, Z. Liu, L. Meng, E.-P. Yao, Y. Liu, A. Schiffer, and Y. Yang. Guanidinium: a route to enhanced carrier lifetime and open-circuit voltage in hybrid perovskite solar cells. *Nano Lett.*, 16(2):1009–1016, 2016. doi: 10.1021/acs.nanolett.5b04060.

[42] K. Momma and F. Izumi. Vesta 3 for three-dimensional visualization of crystal, volumetric and morphology data. *J. Appl. Crystallogr.*, 44(6):1272–1276, 2011. doi: 10.1107/S0021889811038970.

[43] H. J. Monkhorst and J. D. Pack. Special points for brillouin-zone integrations. *Phys. Rev. B*, 13:5188, 1976. doi: 10.1103/PhysRevB.13.5188.

[44] E. Mosconi, J. M. Azpiroz, and F. De Angelis. *Ab Initio* molecular dynamics simulations of methylammonium lead iodide perovskite degradation by water. *Chem. Mater.*, 27(13):4885–4892, 2015.

[45] G. Nagabhushana, R. Shivaramaiah, and A. Navrotsky. Direct calorimetric verification of thermodynamic instability of lead halide hybrid perovskites. *P. Natl. Acad. Sci. USA.*, 113(28):7717–7721, 2016. doi: 10.1016/j.jallcom.2003.10.017.

[46] J. Neugebauer and M. Scheffler. Adsorbate-substrate and adsorbate-adsorbate interactions of Na and K adlayers on Al(111). *Phys. Rev. B*, 46:16067–16080, Dec 1992. doi: 10.1103/PhysRevB.46.16067.

[47] N. Onoda-Yamamuro, T. Matsuo, and H. Suga. Calorimetric and IR spectroscopic studies of phase transitions in methylammonium trihalogenoplumbates (ii). *J. Phys. Chem. Solids.*, 51(12):1383–1395, 1990. doi: 10.1016/0022-3697(90)90021-7.

[48] J. Palomo and P. N. Pintauro. Competitive absorption of quaternary ammonium and alkali metal cations into a nafion cation-exchange membrane. *J Membrane. Sci.*, 215 (1):103–114, 2003.

[49] N.-G. Park. Organometal perovskite light absorbers toward a 20% efficiency low-cost solid-state mesoscopic solar cell. *J. Phys. Chem. Lett.*, 4(15):2423–2429, 2013. doi: 10.1021/jz400892a.

[50] L. Pauling. The principles determining the structure of complex ionic crystals. *J. Am. Chem. Soc.*, 51(4):1010–1026, 1929. doi: 10.1021/ja01379a006.

[51] J. P. Perdew, K. Burke, and M. Ernzerhof. Generalized gradient approximation made simple. *Phys. Rev. Lett.*, 77:3865, 1996. doi: 10.1103/PhysRevLett.77.3865.

[52] A. Poglitsch and D. Weber. Dynamic disorder in methylammoniumtrihalogenoplumbates (ii) observed by millimeter-wave spectroscopy. *J. Chem. Phys.*, 87(11): 6373–6378, 1987. doi: doi:10.1063/1.453467.

[53] M. V. Rane, A. Navrotsky, and G. A. Rossetti. Enthalpies of formation of lead zirconate

titanate (PZT) solid solutions. *J. Solid. State. Chem.*, 161(2):402–409, 2001. doi: 10.1006/jssc.2001.9355.

[54] J. R. Reeher, G. D. Flesch, and H. J. Svec. The mass spectra and ionization potentials of the neutral fragments produced during the electron bombardment of aromatic compounds. *Org. Mass Spectrom.*, 11(2):154–166, 1976. doi: 10.1002/oms.1210110210.

[55] S. Ryu, J. H. Noh, N. J. Jeon, Y. C. Kim, W. S. Yang, J. Seo, and S. I. Seok. Voltage output of dfficient perovskite solar cells with high open-circuit voltage and fill factor. *Energy Environ. Sci.*, 7(8):2614–2618, 2014. doi: 10.1039/C4EE00762J.

[56] S. Sharma, N. Weiden, and A. Weiss. Phase diagrams of quasibinary systems of the type: $ABX_3$–$A'BX_3$; $ABX_3$–$AB'X_3$, and $ABX_3$–$ABX'_3$; X= halogen. *Z. Phys. Chem.*, 175(Part_1):63–80, 1992. doi: 10.1524/zpch.1992.175.Part_1.063.

[57] C. C. Stoumpos, C. D. Malliakas, and M. G. Kanatzidis. Semiconducting tin and lead iodide perovskites with organic cations: Phase transitions, high mobilities, and near-infrared photoluminescent properties. *Inorg. Chem.*, 52(15):9019–9038, 2013. doi: 10.1021/ic401215x.

[58] C. C. Stoumpos, C. D. Malliakas, J. A. Peters, Z. Liu, M. Sebastian, J. Im, T. C. Chasapis, A. C. Wibowo, D. Y. Chung, and e. a. Freeman, Arthur J. Crystal growth of the perovskite semiconductor $CsPbBr_3$: A new material for high-energy radiation detection. *Cryst. Growth Des.*, 13(7):2722–2727, 2013. doi: 10.1021/cg400645t.

[59] M. Szafrański. Investigation of phase instabilities in guanidinium halogenoplumbates (ii). *Thermochim. Acta*, 307(2):177–183, 1997. doi: 10.1016/S0040-6031(97)00408-5.

[60] M. Szafrański and M. Jarek. Origin of spontaneous polarization and reconstructive phase transition in guanidinium iodide. *CrystEngComm*, 15(23):4617–4623, 2013. doi: 10.1039/C3CE26979E.

[61] E. Tenuta, C. Zheng, and O. Rubel. Thermodynamic origin of instability in hybrid halide perovskites. *Sci. Rep.*, 6:37654, 2016. doi: 10.1038/srep37654.

[62] R. S. Treptow. Determination of $\delta$H for reactions of the Born-Haber cycle. *J. Chem. Educ.*, 74(8):919, 1997. doi: 10.1021/ed074p919.

[63] M. T. Weller, O. J. Weber, J. M. Frost, and A. Walsh. Cubic perovskite structure of black formamidinium lead iodide, $\alpha$-$HC(NH_2)_2PbI_3$, at 298 k. *J. Phys. Chem. Lett.*, 6 (16):3209–3212, 2015. doi: 10.1021/acs.jpclett.5b01432.

[64] S. Wozny, M. Yang, A. M. Nardes, C. C. Mercado, S. Ferrere, M. O. Reese, W. Zhou, and K. Zhu. Controlled humidity study on the formation of higher efficiency formamidinium lead triiodide-based solar cells. *Chem. Mater.*, 27(13):4814–4820, 2015. doi: 10.1021/ja511132a.

[65] W. S. Yang, J. H. Noh, N. J. Jeon, Y. C. Kim, S. Ryu, J. Seo, and S. I. Seok. High-performance photovoltaic perovskite layers fabricated through intramolecular exchange. *Science*, 348(6240):1234–1237, 2015. doi: 10.1126/science.aaa9272.

[66] L. Zhang and P. H.-L. Sit. *Ab Initio* study of interaction of water, hydroxyl radicals, and hydroxide ions with $CH_3NH_3PbI_3$ and $CH_3NH_3PbBr_3$ surfaces. *J. Phys. Chem. C*, 119(39):22370–22378, 2015.

[67] Y.-Y. Zhang, S. Chen, P. Xu, H. Xiang, X.-G. Gong, A. Walsh, and S.-H. Wei. Intrinsic instability of the hybrid halide perovskite semiconductor ch3nh3pbi3. *Chin. Phys. Lett.*, 35(3):036104, 2018.

[68] J. Zhao, B. Cai, Z. Luo, Y. Dong, Y. Zhang, H. Xu, B. Hong, Y. Yang, L. Li, and W. Zhang. Investigation of the hydrolysis of perovskite organometallic halide $CH_3NH_3PbI_3$ in humidity environment. *Sci. Rep.*, 6:21976, 2016.

# Chapter 5

# Aziridinium lead iodide: a stable, low bandgap hybrid halide perovskite for photovoltaics

**Author contributions:** I conceived this project based on the criteria of the formability of hybrid halide perovskites. All the calculations and analyses were done by myself with the guidance of Dr. Oleg Rubel. I wrote the manuscript and Dr. Oleg Rubel edited the manuscript. This chapter is published in *The Journal of Physical Chemistry Letters*, 2018.

Note that thanks to Dr. Yurij Mozharivskyj and Dr. Ayse Turak for valuable comments on this project. They questioned the instability of the three-membered ring. The instability of the three-membered ring is further discussed in Chapter 6.

## 5.1 Introduction

During the past ten years, hybrid halide perovskites have increasingly caught researchers' attention as the absorber layers in photovoltaics[14,31,34,37,70]. Favourable electronic properties and a low-cost fabrication method give halide hybrid perovskites an advantage over

the traditional silicon. One drawback of halide hybrid perovskites is their instability. The halide hybrid perovskites easily decompose under the influence of high temperature, oxygen, water, and even UV light[8,12,69]. Zhang et al.[71] pointed out that the instability of methylammonium (MA) lead iodide is intrinsic due to the similar total energies of the reactant and products obtained from the density-functional theory (DFT) calculation. To commercialize the hybrid halide perovskite photovoltaics, the stability issue should be resolved.

The impovements of device architectures are proposed to stabilize the perovskite photovoltaics[20,26,37,74]. However, the power conversion efficiencies still decrease by 60 % of the initial value after 1100 hours[9] which is far from silicon solar panels that come on today's market with a 25-year long performance warranty. The nature of the instability of hybrid halide perovskite cannot be eliminated. In this paper, we propose a new perovskite material with a highly unfavourable decomposition reaction enthalpy, which should stabilize it against degradation.

Hybrid halide perovskite structures discussed here are considered in the form of $A\mathrm{PbI_3}$. Here $A$ stands for an organic radical in the lead iodide framework. Based on our recent paper, the ionization energy of the molecule in the $A$ site (in addition to its size) can be an important factor which determines the stability of perovskites[72]. Lower ionization energy of the cation favours a more stable structure.

Kieslich et al.[30] proposed nitrogen-based cations, which were not used in perovskites before. From this group, an azetidinium radical $(\mathrm{CH_2})_3\mathrm{NH_2}$ is promising due to its compact structure. This four-membered ring cation is larger than MA radical but slightly smaller than the formamidinium radical $\mathrm{HC(NH_2)_2}$. Recently, the azetidinium lead iodide $(\mathrm{CH_2})_3\mathrm{NH_2PbI_3}$ was successfully synthesized[53]. The crystal structure of quasicubic $(\mathrm{CH_2})_3\mathrm{NH_2PbI_3}$ is shown in Fig. 5.1b. Pering et al.[53] reported that $(\mathrm{CH_2})_3\mathrm{NH_2PbI_3}$ demonstrates a very good stability when soaked in water in contrast to the MA lead iodide $\mathrm{CH_3NH_3PbI_3}$. This observation correlates with the ionization energy of the $(\mathrm{CH_2})_3\mathrm{NH_2}$ radical being 0.4 eV below that of MA. However, the wide band gap of 2.15 eV for

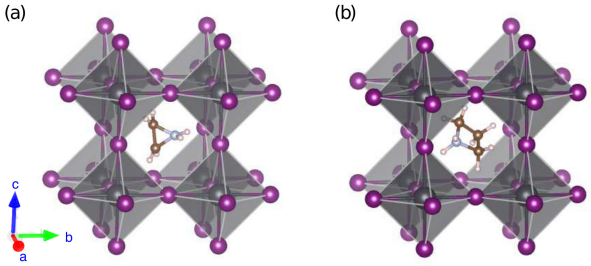


Figure 5.1: The quasicubic crystal structures of cyclic ring-based perovskites: (a) aziridinium lead iodide$(CH_2)_2NH_2PbI_3$ and (b) azetidinium lead iodide $(CH_2)_3NH_2PbI_3$.

$(CH_2)_3NH_2PbI_3$ is not promising for photovoltaics[53].

Interestingly, there are also three-membered rings[59], of which the aziridinium radical $(CH_2)_2NH_2$ is a promising candidate to be used as the organic cation at $A$ site of hybrid halide perovskites. Figure 5.1a illustrates a proposed quasicubic phase of $(CH_2)_2NH_2PbI_3$. This three-membered ring cation is only slightly larger than MA. As we will show below, the ionization energy of $(CH_2)_2NH_2$ is also much lower than that of MA. This fact implies that aziridinium lead iodide $(CH_2)_2NH_2PbI_3$ might be stable and suitable for photovoltaic applications. Here we discuss the structural stability and electronic properties of the new perovskite $(CH_2)_2NH_2PbI_3$. We also compare relevant electronic properties between $(CH_2)_2NH_2PbI_3$, $CH_3NH_3PbI_3$, and $(CH_2)_3NH_2PbI_3$.

## 5.2 Computational methods

An experimental structure of formamidinium iodide $HC(NH_2)_2I$[54] was used as a parent structure for $(CH_2)_2NH_2I$ (Fig. 5.2) and $(CH_2)_3NH_2I$ salts. The hexagonal structures of $CH_3NH_3PbI_3$, $(CH_2)_2NH_2PbI_3$ and $(CH_2)_3NH_2PbI_3$ are adopted from the hexagonal $HC(NH_2)_2PbI_3$[62]. The crystal structures of $CH_3NH_3PbBr_3$ and $CH_3NH_3PbCl_3$ are obtained from Swainson et al.[64] and Chi et al.[11], respectively. The crystal structures of MA halides are obtained from Gabe[18], Hughes and Lipscomb[24], Ishida et al.[27]. Crystallographic information files (CIF) with atomic structures used in calculations can be accessed through

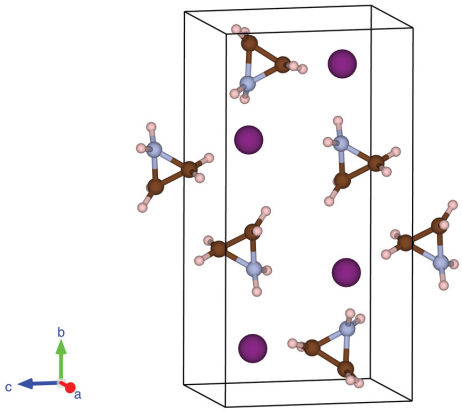


Figure 5.2: The crystal structure of aziridinium iodide $(CH_2)_2NH_2I$.

the Cambridge crystallographic data centre (CCDC deposition numbers 1584308−1584327).

All calculations are based on DFT method[33]. Perdew-Burke-Ernzerhof generalized gradient approximation (PBE-GGA)[51] is used for the exchange-correlation functional. Dispersion interactions are included at the DFT-D3 level[22]. To predict the bandgaps of perovskites, a many body perturbation theory, within the *GW* approach[23,25], is utilized including the spin-orbit coupling (SOC). Vienna *ab initio* simulation program (VASP) and projector augmented-wave potentials are used to perform all the calculations[3,35,36]. Monopole, dipole and quadrupole corrections implemented in VASP[40,47] were used to eliminate leading errors and acquiring accurate total energies of all charged ions.

For reciprocal space integration, $4 \times 4 \times 4$ Monkhorst-Pack grid[44] was used for cubic perovskite phases, $5 \times 5 \times 3$ for tetragonal perovskite phases, $4 \times 4 \times 4$ for hexagonal phases, $5 \times 5 \times 3$ for orthorhombic perovskite phases, and $6 \times 2 \times 4$ for the triclinic phases of $(CH_2)_2NH_2I$ and $(CH_2)_3NH_2I$. The convergence of reaction enthalpies with respect to the k-mesh density is achieved better than 5 meV, which was tested by doubling the density for several perovskite structures and their reactants. The cutoff energy for a plane wave expansion was set at 500 eV. The lattice constant and atomic positions were optimized such that residual forces acting on atoms did not exceed 2 meV/Å, and the residual hydrostatic

Table 5.1: Lattice constants prediction of orthorhombic $CH_3NH_3PbI_3$ with different exchange-correlation functionals

| Functionals | Lattice constants (Å) | | | Error(%) | | | Volume (Å$^3$) | Error(%) |
|---|---|---|---|---|---|---|---|---|
| | a | b | c | a | b | c | | |
| Exp.[68] | 8.81 | 12.59 | 8.56 | – | – | – | 949 | – |
| PBE | 9.23 | 12.86 | 8.63 | 4.8 | 2.2 | 0.8 | 1025 | 7.9 |
| PBE+vdW(D3) | 8.92 | 12.72 | 8.51 | 1.2 | 1.1 | −0.5 | 966 | 1.7 |
| PBEsol | 8.96 | 12.61 | 8.43 | 1.7 | 0.2 | −1.5 | 953 | 0.4 |
| SCAN | 8.93 | 12.69 | 8.53 | −0.4 | −0.3 | −0.4 | 974 | 2.6 |

pressure was less than 50 MPa.

The choice of a suitable exchange-correlation functional is determined by its ability to accurately predict the lattice parameters. Since bare DFT calculations are limited to 0 K, we compare the lattice parameters calculated with different exchange-correlation functionals considering the low-temperature orthorhombic phase of $CH_3NH_3PbI_3$. Results for PBE, PBE+vdW(D3), PBEsol and SCAN functionals are listed in Table 5.1.

## 5.3 Results and discussion

The formability of inorganic perovskite structures can be rationalized via geometrical factors such as the Goldschmidt's tolerance factor[21] and Pauling's octahedral factor[50]. To calculate the geometrical factors of hybrid halide perovskites, the effective organic cation radii are estimated as proposed by Kieslich et al.[30]. The effective radii of three- and four-membered ring cations are listed in Table 5.2 along the side with the representative organic and inorganic cations. The size of cyclic cations is between that of $CH_3NH_3$ and $HC(NH_2)_2$. The cation effective radii are used to evaluate the Goldschmidt's tolerance factor $t$ for $A$PbI$_3$ perovskite structures (Table 5.2). The tolerance factor of $(CH_2)_3NH_2PbI_3$ is too large to form a cubic or tetragonal structure ($t > 0.96$[17]), whereas the tolerance factor for $(CH_2)_2NH_2PbI_3$ is within the perovskite formability limits.

According to our earlier study[72], the radical ionization energy at $A$ site has an effect on

Table 5.2: Geometrical factors of selected perovskites and calculated ionization energies of corresponding $A$ site cations

| Radical $A$ | $A^+$ cation radius (pm) | Tolerance factor for $A\mathrm{PbI_3}$ | Ionization energy (eV) | |
|---|---|---|---|---|
| | | | DFT[a] | Exp. |
| Cs | 181 | 0.81 | 3.85 | 3.89[45] |
| $CH_3NH_3$ | 215 | 0.91 | 4.36 | 4.30±0.1[28] |
| $(CH_2)_2NH_2$ | 227 | 0.93 | 4.07 | ··· |
| $(CH_2)_3NH_2$ | 250 | 0.98 | 3.96 | ··· |
| $HC(NH_2)_2$ | 264 | 1.01 | 4.18 | ··· |

[a] The ionization energies are obtained from the PBE total energy difference of cations and neutral radicals including the vibrational zero-point energy.

the final reaction enthalpy of hybrid halide perovskites. The lower ionization energy, the more stable is the structure. See in Table. 5.2, both radicals $(CH_2)_2NH_2$ and $(CH_2)_3NH_2$ have lower ionization energies than MA. Their values are close to the ionization energy of Cs which is the lowest one in the periodic table. This result suggests that $(CH_2)_2NH_2PbI_3$ and $(CH_2)_3NH_2PbI_3$ should be more stable than $CH_3NH_3PbI_3$.

To further investigate the stability of $(CH_2)_2NH_2PbI_3$, we use the following decomposition reaction equation

$$(CH_2)_2NH_2PbI_3 \rightarrow (CH_2)_2NH_2I + PbI_2 \tag{5.3.1}$$

and the corresponding enthalpy

$$\Delta H_\mathrm{r} = E_\mathrm{tot}[(CH_2)_2NH_2PbI_3] - E_\mathrm{tot}[(CH_2)_2NH_2I] - E_\mathrm{tot}[PbI_2] \ . \tag{5.3.2}$$

The total energies $E_\mathrm{tot}$ of products and the reactant are evaluated using DFT. If the total energy of the products is lower than the total energy of the reactant, the perovskite structure is deemed unstable[71]. This approach ignores finite temperature components of the free energy, which is of the order of $-0.1$ eV for $CH_3NH_3PbI_3$[65].

As a benchmark, we analyzed the stability and polymorphism of $CH_3NH_3PbI_3$. Among

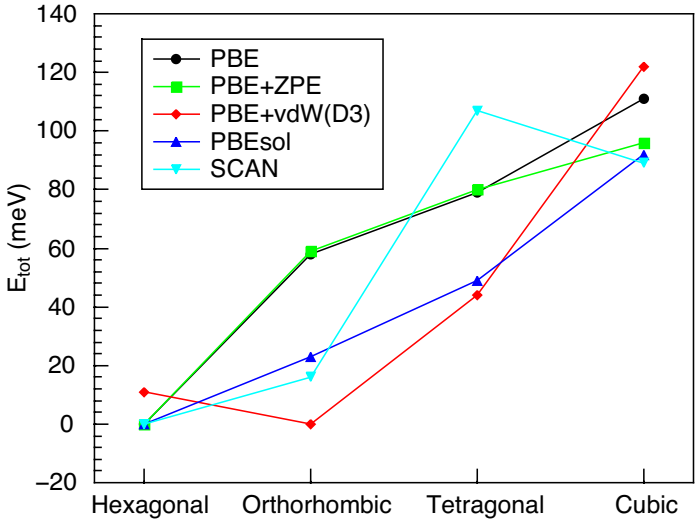


Figure 5.3: Polymorphism of $CH_3NH_3PbI_3$ with different exchange-correlation functionals. The origin of the energy scale is set at the lowest energy structure for each computational technique used.

various polymorphs, we include a possibility for a hexagonal phase, since perovskite structures with large cations ($t > 0.96$) have a tendency to adopt a hexagonal phase. PBE is first used as the exchange-correlation functional. Results listed in Table 5.3 suggest that the hexagonal structure of $CH_3NH_3PbI_3$ has the lowest total energy at 0 K. This finding contradicts experimental data,[48,55,68] according to which $CH_3NH_3PbI_3$ adopts the orthorhombic structure below 162.2 K. Recently, a theory-based study reported similar controversial results on the hexagonal $CH_3NH_3PbI_3$ to have the lowest total energy and predicted it is the stable low-temperature phase[66]. However, we are inclined to think that the hexagonal phase of $CH_3NH_3PbI_3$ is probably a metastable phase. It is the choice of the exchange-correlation functional that is a possible reason for DFT failure to accurately predict the correct polymorphism transformation order of $CH_3NH_3PbI_3$. Thus, different exchange-correlation functionals are employed to evaluate the polymorphism transformation of $CH_3NH_3PbI_3$ (see in Fig. 5.3).

Figure 5.3 illustrates the total energies of different phases of $CH_3NH_3PbI_3$ obtained

Table 5.3: Polymorphism of hybrid halide perovskites predicted using DFT with and without the van der Waals correction.

| Compound | Phase | PBE | | PBE+vdW(D3) | |
|---|---|---|---|---|---|
| | | $E_{\text{tot}}$ (meV) | $\Delta H_{\text{r}}$ (meV) | $E_{\text{tot}}$ (meV) | $\Delta H_{\text{r}}$ (meV) |
| $CH_3NH_3PbI_3$ | Cubic | 111 | 71 | 122 | 160 |
| | Tetragonal | 79 | 39 | 44 | 82 |
| | Orthorhombic | 58 | 18 | 0 | 38 |
| | Hexagonal | 0 | -40 | 11 | 49 |
| $(CH_2)_2NH_2PbI_3$ | Cubic | 107 | -44 | 67 | -81 |
| | Tetragonal | 141 | -10 | 54 | -93 |
| | Orthorhombic | 140 | -12 | 63 | -84 |
| | Hexagonal | 0 | -151 | 0 | -147 |
| $(CH_2)_3NH_2PbI_3$ | Cubic | 174 | -51 | 73 | -199 |
| | Tetragonal | 194 | -31 | 99 | -173 |
| | Orthorhombic | 171 | -54 | 71 | -201 |
| | Hexagonal | 0 | -225 | 0 | -272 |
| $HC(NH_2)_2PbI_3$ | Cubic | 296 | 179 | 238 | 266 |
| | Tetragonal | 142 | 25 | 50 | 79 |
| | Orthorhombic | 113 | -4 | 32 | 61 |
| | Hexagonal | 0 | -117 | 0 | 29 |
| $CH_3NH_3PbBr_3$ | Cubic | ··· | ··· | 71 | 13 |
| | Orthorhombic | ··· | ··· | 0 | -58 |
| $CH_3NH_3PbCl_3$ | Cubic | ··· | ··· | 68 | -41 |
| | Orthorhombic | ··· | ··· | 0 | -109 |

using PBE, PBE+ZPE (zero point energy correction), PBE+vdW(D3)[22], PBEsol[13,52] and SCAN[63] exchange-correlation functionals. Bokdam et al.[6] proposed SCAN as the superior exchange-correlation functional for structural simulations of hybrid halide perovskites. However, all methods except for the PBE+vdW(D3) favour the hexagonal structure at low temperature. The result indicates the importance of dispersion interactions to stabilize the low-temperature orthorhombic $CH_3NH_3PbI_3$. Li and Rinke[38] pointed out that the van der Waals (vdW) correction is also essential to obtain an accurate lattice constant of hybrid halide perovskites. It should be noted that Thind et al.[66] performed similar calculations including vdW-correction, and their results showed that the hexagonal phase still has the lowest total energy among all the phases, which contradicts our results. We suspect that

the reason for discrepancy can be a suboptimal structure of the orthorhombic phase used by Thind et al.[66]. Although the initial structure was adopted from experimental data, the choice of exchange–correlation functional and optimization criteria might lead to this suboptimal structure.

Since van der Waals effects are important for the polymorphism of $CH_3NH_3PbI_3$, the same can be extended for other types of hybrid halide perovskites. Thus we focus on results obtained with PBE+vdW(D3) exchange-correlation functional in the remaining part of the paper. Table 5.3 lists the results of polymorphism prediction and corresponding decomposition reaction enthalpies for the perovskites of interest here. It is noticed that except $CH_3NH_3PbI_3$, all the other perovskites favour the hexagonal structures as the low-temperature stable phase. This trend can be attributed to a greater size of organic cations involved. For $CH_3NH_3PbI_3$ and $HC(NH_2)_2PbI_3$ $\Delta H_\mathrm{r}$ values are weakly positive, which contradicts formability of those compounds. The final temperature contribution will lower the free energy down by approximately 0.1 eV[65] making their formability feasible.

Recent comparative studies of stability among $CH_3NH_3Pb\mathit{X}_3$ perovskites with $X$ =Cl, Br, and I reported that a higher stability can be achieved by switching halide from I, to Br and Cl[8,29,39,41,46,71]. Our calculated stability trend of $CH_3NH_3Pb\mathit{X}_3$ is consistent with those observations. The lower reaction enthalpies of $(CH_2)_2NH_2PbI_3$ suggest that the stability of $(CH_2)_2NH_2PbI_3$ will be superior to $CH_3NH_3PbCl_3$ (Table 5.3).

Moreover, Tenuta et al.[65] indicated that the degradation of $A\mathrm{PbI}_3$ perovskites in the moist environment is governed by the solubility of a $A$I salt. The saturation concentration $c_\mathrm{s}$ of $A$I in the solvent exponentially depends on the reaction enthalpy given by Eq. (5.3.2). Considering a low reaction enthalpy of $(CH_2)_3NH_2PbI_3$, its decomposition via solvation of $(CH_2)_3NH_2I$ in water will be hindered. This prediction is consistent with the exceptional moisture stability of $(CH_2)_3NH_2PbI_3$[53].

The solvation of $A\mathrm{I}_m$ salts can be captured by evaluating an enthalpy of the following

Table 5.4: Solvation enthalpy $\Delta H$ of iodide salts in water.

| Salt | $\Delta H$ (eV) |
|---|---|
| $CH_3NH_3I$ | 0.45 |
| $(CH_2)_2NH_2I$ | 0.45 |
| $(CH_2)_3NH_2I$ | 0.39 |
| $HC(NH_2)_2I$ | 0.35 |
| $PbI_2$ | 2.38 |

reaction

$$AI_m(s) \rightarrow A^{m+}(aq) + mI^-(aq) \tag{5.3.3}$$

Energies of the corresponding products are evaluated using an implicit solvation model of VASPsol[42,43] and the solvation enthalpies are presented in Table 5.4. The lower enthalpy favours solubility of the salt. The high solubility of $CH_3NH_3I$ in water and the low solubility of $PbI_2$ correlate with the enthalpy values listed in Table 5.4. The four discussed $A$I salts have similar solvation enthalpies ranging from 0.35 to 0.45 eV. It suggests a similar solubility of the $A$I salts. Therefore, the proposed perovskite $(CH_2)_2NH_2PbI_3$ should be less prone to decomposition via dissolution in water due to its higher decomposition reaction enthalpy (Table 5.3) rather than differences in solubility of the salt.

We compared the stability of the proposed cation with other mainstream cations using the following decomposition pathway taking $(CH_2)_2NH_2{}^+$ as an example

$$(CH_2)_2NH_2{}^+(aq) + I^-(aq) \rightarrow (CH_2)_2NH(g) + HI(g). \tag{5.3.4}$$

The corresponding enthalpies are listed in Table 5.5. Positive enthalpies indicate the discussed four cations are stable in an aqueous solution.

For the photovoltaic application of $(CH_2)_2NH_2PbI_3$, it is crucial that its structure adopts a cubic phase at room temperature. The Goldschmidt's tolerance factors of $(CH_2)_2NH_2PbI_3$ and $CH_3NH_3PbBr_3$ are the same, 0.93[46]. Since $CH_3NH_3PbBr_3$ prefers a cubic structure at

Table 5.5: Decomposition enthalpy of cations via a proton exchange reaction (Eq. 5.3.4).

| Cation $A^+$ | $\Delta H$ (eV) |
|---|---|
| $CH_3NH_3^+$ | 1.47 |
| $(CH_2)_2NH_2^+$ | 1.25 |
| $(CH_2)_3NH_2^+$ | 1.42 |
| $HC(NH_2)_2^+$ | 1.89 |

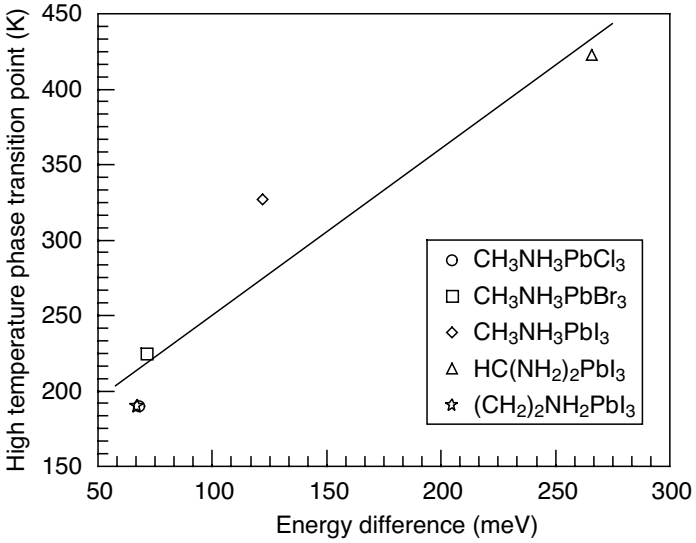


Figure 5.4: Correlation between the high-temperature phase transition point and the energy difference between the low-temperature phase and high-temperature phase. The linear line is a guide to the eye. High-temperature transition temperatures are taken form Refs. Koh et al.[32], Onoda-Yamamuro et al.[48], Poglitsch and Weber[55].

room temperature[48,55], we can expect that $(CH_2)_2NH_2PbI_3$ will exhibit a similar polymorphism as a function of temperature. Besides, we found that the high-temperature phase transition point *vs* the energy difference between the low-temperature and high-temperature phases follows a linear trend (see Fig. 5.4). From Fig. 5.4, the energy difference between cubic and hexagonal structures of $(CH_2)_2NH_2PbI_3$ is 67 meV, which is close to the energy difference of 68 meV between cubic and orthorhombic structures of $CH_3NH_3PbCl_3$. The tetragonal $CH_3NH_3PbCl_3$ transitions to a cubic phase at 190 K. We expect $(CH_2)_2NH_2PbI_3$ to have a similar transition behavior and to adopt the cubic phase above 190 K.

Till now, we found that the $(CH_2)_2NH_2PbI_3$ perovskite solar cells should be more stable

Table 5.6: Bandgaps (eV) of hybrid halide perovskites prediction with PBE+vdW(D3) and PBE+vdW(D3)+SOC

| Compound | Phase | PBE+vdW(D3) | PBE+vdW(D3)+SOC |
|---|---|---|---|
| $CH_3NH_3PbI_3$ | Cubic | 1.44 | 0.38 |
| | Tetragonal | 1.51 | 0.76 |
| | Orthorhombic | 1.72 | 0.86 |
| | Hexagonal | 2.53 | 2.20 |
| $(CH_2)_2NH_2PbI_3$ | Cubic | 1.35 | 0.36 |
| | Tetragonal | 1.58 | 0.62 |
| | Orthorhombic | 1.53 | 0.58 |
| | Hexagonal | 2.74 | 2.35 |
| $(CH_2)_3NH_2PbI_3$ | Cubic | 1.56 | 0.54 |
| | Tetragonal | 1.61 | 0.64 |
| | Orthorhombic | 1.71 | 0.67 |
| | Hexagonal | 2.69 | 2.31 |
| $HC(NH_2)_2PbI_3$ | Cubic | 1.34 | 0.33 |
| | Tetragonal | 1.60 | 0.67 |
| | Orthorhombic | 1.66 | 0.67 |
| | Hexagonal | 2.52 | 2.20 |

than $CH_3NH_3PbI_3$ and $HC(NH_2)_2PbI_3$. [*Note that this conclusion is updated in the next Chapter due to neglect of instability of aziridinium.] The key question remained unanswered is whether the proposed perovskite structure can serve as a solar cell absorber material? Here we report the band gap for the hypothetical $(CH_2)_2NH_2PbI_3$ obtained in the framework of *GW* approximation taking into account relativistic effects. It is known that bandgap is sensitive to structural properties. We found that the PBE+vdW(D3), PBEsol, and SCAN exchange-correlation functionals can provide an accurate prediction for the lattice constants (see Supporting information). Here, we continue to use PBE+vdW(D3) optimized perovskite structures in order to remain consistent with the section on stability calculations. Results for bandgaps obtained using PBE+vdW(D3) exchange-correlation functional with and without SOC effect are shown in Table 5.6.

It is well known that DFT calculations with SOC grossly underestimates the bandgap of perovskites[67]. In Table 5.6, the calculated bandgaps with PBE+vdW(D3)+SOC are

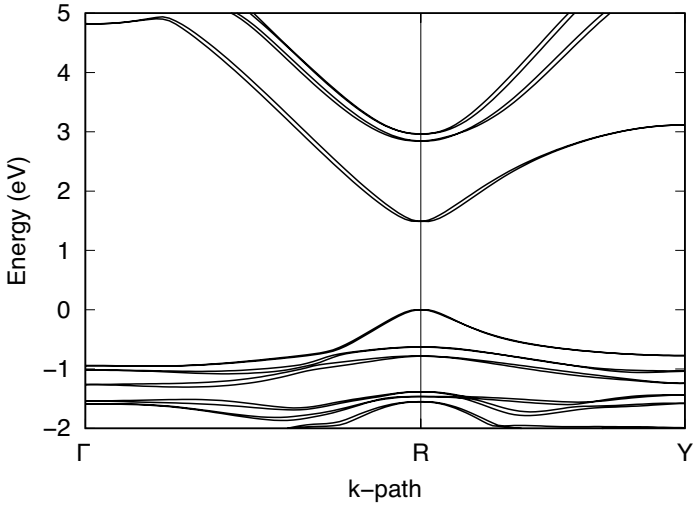


Figure 5.5: Electronic band structure of $(CH_2)_2NH_2PbI_3$ calculated at the PBE+SOC level with the band gap adjusted to match the $G_0W_0$+SOC result in Table 5.7. The $k$-path includes the following high-symmetry points: $\Gamma(0,0,0)$, $\mathrm{R}(0.5,0.5,0.5)$, and $\mathrm{Y}(0,0.5,0)$.

approximately 1 eV lower than the result without SOC. Bandgaps increase from the cubic phase to the hexagonal phase. Polymorphs of $(CH_2)_3NH_2PbI_3$ demonstrate the largest bandgaps among the four perovskites studied here. Bandgaps of different phases of $(CH_2)_2NH_2PbI_3$ lies between $CH_3NH_3PbI_3$ and $HC(NH_2)_2PbI_3$. It is obvious that hexagonal phases show much larger bandgaps than perovskite phases. Thus, the hexagonal phase around room temperature is not desirable when aiming at photovoltaic applications.

Figure 5.5 shows a relativistic band structure of quasicubic $(CH_2)_2NH_2PbI_3$. The fundamental band gap is near R-point of the Brillouin zone. The presence of a Rashba splitting is noticeable at the vicinity of the band extrema, however, its magnitude is heavily reduced when compared with the Rashba splitting at the $CH_3NH_3PbI_3$ band edges[7,16,57,73]. The Rashba splitting in halide hybrid perovskites originates from the strong spin-orbit interaction and distortions in the Pb-centred octahedron[57,73]. A more centrosymmetric $PbI_3$ cage of the quasicubic structure and its larger volume can be a reason for the reduced Rashba splitting in $(CH_2)_2NH_2PbI_3$.

The Rashba splitting in hybrid halide perovskites introduces an effectively indirect

bandgap, which prolongs the carrier lifetime[60,73]. We expect the reduced Rashba splitting in $(CH_2)_2NH_2PbI_3$ not to impede its power conversion efficiency for photovoltaic applications, since a similar weaker splitting can be found in the band structures of $HC(NH_2)_2PbI_3$[10]. Recently, Yang et al.[70] fabricated formamidinium-lead-halide-based perovskite solar cells with a certified 22.1% power conversion efficiency.

It is well known that a first-principle $GW$ approximation with SOC can accurately predict the bandgaps of hybrid halide perovskites[7,67]. First, we used a single-shot $G_0W_0$ approximation with SOC to evaluate the bandgaps of quasicubic phases for perovskites of interest (Table 5.7). Next, we carried out a partially self-consistent calculation by performing 4 iterations of $G$ only (referred to as $GW_0$). The single-shot $G_0W_0$ method gave the best match of bandgaps with the experimental values (Table 5.7). Based on this table, we found that the bandgap of quasicubic $(CH_2)_2NH_2PbI_3$ is 0.17 eV lower than quasicubic $CH_3NH_3PbI_3$ and 0.09 eV higher than quasicubic $HC(NH_2)_2PbI_3$.

The Shockley-Queisser limit[58] states that the ultimate efficiency for a single-junction solar cell can be estimated via

$$\eta(x_g) = \frac{x_g \int_{x_g}^{\infty} x^2/(e^x - 1)\ dx}{\int_0^{\infty} x^3/(e^x - 1)\ dx} \tag{5.3.5}$$

$$x_g = E_g/kT_s. \tag{5.3.6}$$

The symbol $E_g$ in Eq. (5.3.6) is the corresponding bandgap, $k$ is the Boltzmann's constant and $T_s$ is the temperature of the sun. The numerator in Eq. (5.3.5) is finite and vanishes when $x_g$ approaches zero and approaches infinity[4,58]. When $E_g = 1.1\ eV$, $\eta(x_g)$ has a maximum value[58]. Hence, compared with bandgap of $CH_3NH_3PbI_3$, lower bandgap of $(CH_2)_2NH_2PbI_3$ is closer to the optimal $E_g = 1.1\ eV$. This discussion suggests that $(CH_2)_2NH_2PbI_3$ may render a higher efficiency than $CH_3NH_3PbI_3$.

Table 5.7: Quasiparticle bandgaps (eV) of various perovskites in the quasicubic phase.

| Perovskites | $G_0W_0$+SOC | $GW_0$+SOC | Exp. | Reported $GW$+SOC |
|---|---|---|---|---|
| $CH_3NH_3PbI_3$ | 1.66 | 1.76 | 1.69[56] | 1.27−1.67[1,5,7,19,56] |
| $(CH_2)_2NH_2PbI_3$ | 1.49 | 1.53 | ··· | ··· |
| $(CH_2)_3NH_2PbI_3$ | 1.84 | 1.99 | ··· | ··· |
| $HC(NH_2)_2PbI_3$ | 1.40 | 1.44 | 1.43−1.48[15,32,49,61] | 1.46[2] |

## 5.4 Conclusion

To summarize, we used first-principle calculations to predict the structure and characterize the stability and electronic properties of hybrid halide perovskites. The PBE exchange-correlation functional was used to evaluate the ionization energy of different cations. The polymorphism of perovskites is best captured when van der Waals correction is included at the PBE+vdW(D3) level to accurately predict the order of phases. An implicit solvation model was used to describe the interaction between a solute and solvent (water) when evaluating the solubility of perovskite decomposition products. The electronic band structure and Rashba splitting effect are captured through a relativistic calculation at the PBE level. To estimate the bandgaps of perovskites, we used a quasiparticle $GW$ approximation considering the spin-orbit interaction, which gives the most accurate results compared with experimental data. As a result, we proposed a three-membered cyclic organic cation based halide hybrid perovskite $(CH_2)_2NH_2PbI_3$ which has the potential to be used as the absorber material for photovoltaics. The low ionization energy of organic radical $(CH_2)_2NH_2$ decreases the reaction enthalpy of forming the corresponding perovskite. It suggests that this lower reaction enthalpy renders a much better stability of $(CH_2)_2NH_2PbI_3$ than $CH_3NH_3PbI_3$ and $HC(NH_2)_2PbI_3$.[*Note that this conclusion is updated in the next Chapter due to neglect of instability of aziridinium.] The appropriate cation radius of $(CH_2)_2NH_2$ for the $PbI_3$ framework and a low energy difference between high-temperature and low-temperature phases make $(CH_2)_2NH_2PbI_3$ transfer to a cubic phase feasible below room temperature. Relativistic band structure plot demonstrates the existence of a Rashba

splitting in $(CH_2)_2NH_2PbI_3$, albeit less prominent than in $CH_3NH_3PbI_3$. The Rashba splitting will allow $(CH_2)_2NH_2PbI_3$ to form an indirect bandgap near R-point in the Brillouin zone and benefit from an enhanced charge carrier lifetime. *GW* calculations suggest that the cubic phase of $(CH_2)_2NH_2PbI_3$ has an even lower bandgap of 1.49 eV than $CH_3NH_3PbI_3$ thereby making the former perovskite a suitable absorber material for solar cells.

# Bibliography

[1] T. Ahmed, T. Salim, C. La-o vorakiat, Y. Lam, E. E. Chia, J. X. Zhu, and et al. Optical properties of organometallic perovskite: An *Ab Initio* study using relativistic GW correction and bethe-salpeter equation. *EPL*, 108(6):67015, 2015. doi: 10.1209/0295-5075/108/67015.

[2] N. Arora, S. Orlandi, M. I. Dar, S. Aghazada, G. Jacopin, M. Cavazzini, E. Mosconi, P. Gratia, F. De Angelis, G. Pozzi, and et al. High open-circuit voltage: Fabrication of formamidinium lead bromide perovskite solar cells using fluorene-dithiophene derivatives as hole-transporting materials. *ACS Energy Lett.*, 1(1):107–112, 2016. doi: 10.1021/acsenergylett.6b00077.

[3] P. Blöchl. Projector augmented-wave method. *Phys. Rev. B*, 50(24):17953, 1994.

[4] K.-H. Böhm and B. Schlender. Tabelle von integralen über die kirchhoff-planck-funktion. *Z. Astrophys.*, 43:95, 1957.

[5] M. Bokdam, T. Sander, A. Stroppa, S. Picozzi, D. Sarma, C. Franchini, and G. Kresse. Role of polar phonons in the photo excited state of metal halide perovskites. *Sci. Rep.*, 6:28618, 2016. doi: 10.1038/srep28618.

[6] M. Bokdam, J. Lahnsteiner, B. Ramberger, T. Schäfer, and G. Kresse. Assessing density functionals using many body theory for hybrid perovskites. *Phys. Rev. Lett.*, 119:145501, Oct 2017. doi: 10.1103/PhysRevLett.119.145501.

[7] F. Brivio, K. T. Butler, A. Walsh, and M. van Schilfgaarde. Relativistic quasiparticle self-consistent electronic structure of hybrid halide perovskite photovoltaic absorbers. *Phys. Rev. B*, 89:155204, Apr 2014. doi: 10.1103/PhysRevB.89.155204.

[8] A. Buin, R. Comin, J. Xu, A. H. Ip, and E. H. Sargent. Halide-dependent electronic

structure of organolead perovskite materials. *Chem. Mater.*, 27(12):4405–4412, 2015. doi: 10.1021/acs.chemmater.5b01909.

[9] A. Chauhan and P. Kumar. Degradation in perovskite solar cells stored in different environmental conditions. *J. Phys. D*, 50(32):325105–325116, 2017. doi: 10.1088/1361-6463/aa7905.

[10] T. Chen, W. L. Chen, B. J. Foley, J. Lee, J. P. Ruff, J. P. Ko, C. M. Brown, L. W. Harriger, D. Zhang, C. Park, and et al. Origin of long lifetime of band-edge charge carriers in organic-inorganic lead iodide perovskites. *Proc. Natl. Acad. Sci. U.S.A.*, 114 (29):7519–7524, 2017. doi: 10.1073/pnas.1704421114.

[11] L. Chi, I. Swainson, L. Cranswick, J. H. Her, P. Stephens, and O. Knop. The ordered phase of methylammonium lead chloride $CH_3ND_3PbCl_3$. *J. Solid State Chem.*, 178(5): 1376–1385, 2005. doi: doi.org/10.1016/j.jssc.2004.12.037.

[12] J. A. Christians, P. A. M. Herrera, and P. V. Kamat. Transformation of the excited state and photovoltaic efficiency of $CH_3NH_3PbI_3$ perovskite upon controlled exposure to humidified air. *J. Am. Chem. Soc.*, 137(4):1530–1538, 2015. doi: 10.1021/ja511132a.

[13] G. I. Csonka, J. P. Perdew, A. Ruzsinszky, P. H. T. Philipsen, S. Lebègue, J. Paier, O. A. Vydrov, and J. G. Ángyán. Assessing the performance of recent density functionals for bulk solids. *Phys. Rev. B*, 79:155107, Apr 2009. doi: 10.1103/PhysRevB.79.155107.

[14] G. E. Eperon, V. M. Burlakov, P. Docampo, A. Goriely, and H. J. Snaith. Morphological control for high performance, solution-processed planar heterojunction perovskite solar cells. *Adv. Funct. Mater.*, 24(1):151–157, 2014. doi: 10.1002/adfm.201302090.

[15] G. E. Eperon, S. D. Stranks, C. Menelaou, M. B. Johnston, L. M. Herz, and H. J.

Snaith. Formamidinium lead trihalide: A broadly tunable perovskite for efficient planar heterojunction solar cells. *Energy Environ. Sci.*, 7(3):982–988, 2014.

[16] J. Even, L. Pedesseau, J. M. Jancu, and C. Katan. Importance of spin-orbit coupling in hybrid organic/inorganic perovskites for photovoltaic applications. *J. Phys. Chem. Lett.*, 4(17):2999–3005, 2013. doi: 10.1021/jz401532q.

[17] L. Feng, L. Jiang, M. Zhu, H. Liu, X. Zhou, and C. Li. Formability of $ABO_3$ cubic perovskites. *J. Phys. Chem. Solids*, 69(4):967–974, 2008. doi: 10.1016/j.jpcs.2007.11.007.

[18] E. Gabe. The crystal structure of methylammonium bromide. *Acta Cryst.*, 14(12):1296–1296, 1961. doi: 10.1107/S0365110X6100382X.

[19] W. Gao, X. Gao, T. A. Abtew, Y. Y. Sun, S. Zhang, and P. Zhang. Quasiparticle band gap of organic-inorganic hybrid perovskites: Crystal structure, spin-orbit coupling, and self-energy effects. *Phys. Rev. B*, 93:085202, Feb 2016. doi: 10.1103/PhysRevB.93.085202.

[20] S. A. Gevorgyan, M. V. Madsen, H. F. Dam, M. Jørgensen, C. J. Fell, K. F. Anderson, B. C. Duck, A. Mescheloff, E. A. Katz, A. Elschner, and et al. Interlaboratory outdoor stability studies of flexible roll-to-roll coated organic photovoltaic modules: Stability over 10,000 h. *Sol. Energ. Mat. Sol. Cells*, 116:187–196, 2013.

[21] V. M. Goldschmidt. Die gesetze der krystallochemie. *Naturwissenschaften*, 14(21):477–485, 1926. doi: 10.1007/BF01507527.

[22] S. Grimme, J. Antony, S. Ehrlich, and H. Krieg. A consistent and accurate *Ab Initio* parametrization of density functional dispersion correction (DFT-D) for the 94 elements h-pu. *J. Chem. Phys.*, 132(15):154104, 2010. doi: 10.1063/1.3382344.

[23] L. Hedin. New method for calculating the one-particle Green's function with application to the electron-gas problem. *Phys. Rev.*, 139:A796–A823, 1965. doi: 10.1103/PhysRev.139.A796.

[24] E. W. Hughes and W. N. Lipscomb. The crystal structure of methylammonium chloride. *J. Am. Chem. Soc.*, 68(10):1970–1975, 1946. doi: 10.1021/ja01214a029.

[25] M. S. Hybertsen and S. G. Louie. Electron correlation in semiconductors and insulators: Band gaps and quasiparticle energies. *Phys. Rev. B*, 34:5390–5413, Oct 1986. doi: 10.1103/PhysRevB.34.5390.

[26] J. H. Im, C. R. Lee, J. W. Lee, S. W. Park, and N. G. Park. 6.5% efficient perovskite quantum-qot-sensitized solar cell. *Nanoscale*, 3(10):4088–4093, 2011. doi: 10.1039/C1NR10867K.

[27] H. Ishida, H. Maeda, A. Hirano, T. Fujimoto, Y. Kubozono, S. Kashino, and S. Emura. Exafs study on the phase transition (phase $\alpha$'–$\delta$) in $CH_3NH_3I$. *Z. Naturforsch. A.*, 50 (9):876–880, 1995.

[28] S. J. Jeon, A. B. Raksit, G. I. Gellene, and R. F. Porter. Formation of hypervalent ammoniated radicals by neutralized ion beam techniques. *J. Am. Chem. Soc.*, 107(14): 4129–4133, 1985. doi: 10.1021/ja00300a006.

[29] U. G. Jong, C. J. Yu, J. S. Ri, N. H. Kim, and G. C. Ri. Influence of halide composition on the structural, electronic, and optical properties of mixed $CH_3NH_3Pb(I_{1-x}Br_x)_3$ perovskites calculated using the virtual crystal approximation method. *Phys. Rev. B*, 94:125139, Sep 2016. doi: 10.1103/PhysRevB.94.125139.

[30] G. Kieslich, S. Sun, and A. K. Cheetham. Solid-state principles applied to organic-inorganic perovskites: New tricks for an old dog. *Chem. Sci.*, 5(12):4712–4715, 2014. doi: 10.1039/C4SC02211D.

[31] H. S. Kim, C. R. Lee, J. H. Im, K. B. Lee, T. Moehl, A. Marchioro, S. J. Moon, R. Humphry Baker, J. H. Yum, J. E. Moser, and et al. Lead iodide perovskite sensitized all-solid-state submicron thin film mesoscopic solar cell with efficiency exceeding 9%. *Sci. Rep.*, 2:591, 2012. doi: 10.1038/srep00591.

[32] T. M. Koh, K. Fu, Y. Fang, S. Chen, T. Sum, N. Mathews, S. G. Mhaisalkar, P. P. Boix, and T. Baikie. Formamidinium-containing metal-halide: An alternative material for near-IR absorption perovskite solar cells. *J. Phys. Chem. C*, 118(30):16458–16462, 2013. doi: 10.1021/jp411112k.

[33] W. Kohn and L. J. Sham. Self-consistent equations including exchange and correlation effects. *Phys. Rev.*, 140(4A):A1133, 1965. doi: 10.1103/PhysRev.140.A1133.

[34] A. Kojima, K. Teshima, Y. Shirai, and T. Miyasaka. Organometal halide perovskites as visible-light sensitizers for photovoltaic cells. *J. Am. Chem. Soc.*, 131(17):6050–6051, 2009. doi: 10.1021/ja809598r.

[35] G. Kresse and J. Furthmüller. Efficient iterative schemes for *Ab Initio* total-energy calculations using a plane-wave basis set. *Phys. Rev. B*, 54(16):11169, 1996.

[36] G. Kresse and D. Joubert. From ultrasoft pseudopotentials to the projector augmented-wave method. *Phys. Rev. B*, 59(3):1758, 1999.

[37] M. M. Lee, J. Teuscher, T. Miyasaka, T. N. Murakami, and H. J. Snaith. Efficient hybrid solar cells based on meso-superstructured organometal halide perovskites. *Science*, 338(6107):643–647, 2012. doi: 10.1126/science.1228604.

[38] J. Li and P. Rinke. Atomic structure of metal-halide perovskites from first-principles: The chicken-and-egg paradox of the organic-inorganic interaction. *Phys. Rev. B*, 94: 045201, Jul 2016. doi: 10.1103/PhysRevB.94.045201.

[39] G. Maculan, A. D. Sheikh, A. L. Abdelhady, M. I. Saidaminov, M. A. Haque, B. Murali, E. Alarousu, O. F. Mohammed, T. Wu, and O. M. Bakr. $CH_3NH_3PbCl_3$ single crystals: Inverse temperature crystallization and visible-blind UV-photodetector. *J. Phys. Chem. Lett.*, 6(19):3781–3786, 2015. doi: 10.1021/acs.jpclett.5b01666.

[40] G. Makov and M. C. Payne. Periodic boundary conditions in *Ab Initio* calculations. *Phys. Rev. B*, 51:4014–4022, Feb 1995. doi: 10.1103/PhysRevB.51.4014.

[41] S. S. Mali, C. S. Shim, and C. K. Hong. Highly stable and efficient solid-state solar cells based on methylammonium lead bromide ($CH_3NH_3PbBr_3$) perovskite quantum dots. *NPG Asia Mater.*, 7(8):e208, 2015.

[42] K. Mathew and R. G. Hennig. Implicit self-consistent description of electrolyte in plane-wave density-functional theory. *arXiv preprint arXiv:1601.03346*, 2016.

[43] K. Mathew, R. Sundararaman, K. Letchworth-Weaver, T. Arias, and R. G. Hennig. Implicit solvation model for density-functional study of nanocrystal surfaces and reaction pathways. *J. Chem. Phys.*, 140(8):084106, 2014. doi: 10.1063/1.4865107.

[44] H. J. Monkhorst and J. D. Pack. Special points for brillouin-zone integrations. *Phys. Rev. B*, 13:5188–5192, Jun 1976. doi: 10.1103/PhysRevB.13.5188. URL `https://link.aps.org/doi/10.1103/PhysRevB.13.5188`.

[45] C. E. Moore. *Ionization Potentials and Ionization Limits Derived from the Analyses of Optical Spectra*. United States. Government Printing Office., Washington D.C., 1970.

[46] G. Nagabhushana, R. Shivaramaiah, and A. Navrotsky. Direct calorimetric verification of thermodynamic instability of lead halide hybrid perovskites. *P. Natl. Acad. Sci. USA.*, 113(28):7717–7721, 2016. doi: 10.1016/j.jallcom.2003.10.017.

[47] J. Neugebauer and M. Scheffler. Adsorbate-substrate and adsorbate-adsorbate interactions of Na and K adlayers on Al(111). *Phys. Rev. B*, 46:16067–16080, Dec 1992. doi: 10.1103/PhysRevB.46.16067.

[48] N. Onoda-Yamamuro, T. Matsuo, and H. Suga. Calorimetric and IR spectroscopic studies of phase transitions in methylammonium trihalogenoplumbates (ii). *J. Phys. Chem. Solids.*, 51(12):1383–1395, 1990. doi: 10.1016/0022-3697(90)90021-7.

[49] S. Pang, H. Hu, J. Zhang, S. Lv, Y. Yu, F. Wei, T. Qin, H. Xu, Z. Liu, and G. Cui. $NH_2CH{=}NH_2PbI_3$: An alternative organolead iodide perovskite sensitizer for mesoscopic solar cells. *Chem. Mater.*, 26(3):1485–1491, 2014. doi: 10.1021/cm404006p.

[50] L. Pauling. The principles determining the structure of complex ionic crystals. *J. Am. Chem. Soc.*, 51(4):1010–1026, 1929. doi: 10.1021/ja01379a006.

[51] J. P. Perdew, K. Burke, and M. Ernzerhof. Generalized gradient approximation made simple. *Phys. Rev. Lett.*, 77:3865–3868, Oct 1996. doi: 10.1103/PhysRevLett.77.3865.

[52] J. P. Perdew, A. Ruzsinszky, G. I. Csonka, O. A. Vydrov, G. E. Scuseria, L. A. Constantin, X. Zhou, and K. Burke. Restoring the density-gradient expansion for exchange in solids and surfaces. *Phys. Rev. Lett.*, 100:136406, Apr 2008. doi: 10.1103/PhysRevLett.100.136406.

[53] S. R. Pering, W. Deng, J. R. Troughton, P. S. Kubiak, D. Ghosh, R. G. Niemann, F. Brivio, F. E. Jeffrey, A. B. Walker, M. S. Islam, and et al. Azetidinium lead iodide for perovskite solar cells. *J. Mater. Chem. A*, 5:20658–20665, 2017. doi: 10.1039/C7TA07545F.

[54] A. A. Petrov, E. A. Goodilin, A. B. Tarasov, V. A. Lazarenko, P. V. Dorovatovskii, and V. N. Khrustalev. Formamidinium iodide: Crystal structure and phase transitions. *Acta Crystallogr. Sect. E*, 73(4):569–572, 2017. doi: 10.1107/S205698901700425X.

[55] A. Poglitsch and D. Weber. Dynamic disorder in methylammoniumtrihalogenoplumbates (ii) observed by millimeter-wave spectroscopy. *J. Chem. Phys.*, 87(11): 6373–6378, 1987. doi: doi:10.1063/1.453467.

[56] C. Quarti, E. Mosconi, J. M. Ball, V. D'Innocenzo, C. Tao, S. Pathak, H. J. Snaith, A. Petrozza, and F. De Angelis. Structural and optical properties of methylammonium lead iodide across the tetragonal to cubic phase transition: Implications for perovskite solar cells. *Energy Environ. Sci.*, 9(1):155–163, 2016. doi: 10.1039/C5EE02925B.

[57] O. Rubel and A. Bokhanchuk. Robust bloch character at the band edges of hybrid halide perovskites. *arXiv preprint arXiv:1508.03612*, 2015.

[58] W. Shockley and H. J. Queisser. Detailed balance limit of efficiency of p-n junction solar cells. *J. Appl. Phys.*, 32(3):510–519, 1961. doi: 10.1063/1.1736034.

[59] B. Solka and M. Russell. Energetics of formation of some structural isomers of gaseous $[C_2H_5O]^+$ and $[C_2H_6N]^+$ ions. *J. Phys. Chem.*, 78(13):1268–1273, 1974. doi: 10.1021/j100606a007.

[60] A. V. Stier, K. M. McCreary, B. T. Jonker, J. Kono, and S. A. Crooker. Exciton diamagnetic shifts and valley zeeman effects in monolayer $WS_2$ and $MoS_2$ to 65 Tesla. *Nat. Commun.*, 7:10643, 2016. doi: 10.1038/ncomms2972.

[61] C. C. Stoumpos and M. G. Kanatzidis. The renaissance of halide perovskites and their evolution as emerging semiconductors. *Acc. Chem. Res.*, 48(10):2791–2802, 2015. doi: 10.1021/acs.accounts.5b00229.

[62] C. C. Stoumpos, C. D. Malliakas, and M. G. Kanatzidis. Semiconducting tin and lead iodide perovskites with organic cations: Phase transitions, high mobilities, and near-infrared photoluminescent properties. *Inorg. Chem.*, 52(15):9019–9038, 2013. doi: 10.1021/ic401215x.

[63] J. Sun, A. Ruzsinszky, and J. P. Perdew. Strongly constrained and appropriately normed semilocal density functional. *Phys. Rev. Lett.*, 115:036402, Jul 2015. doi: 10.1103/PhysRevLett.115.036402.

[64] I. Swainson, R. Hammond, C. Soulliere, O. Knop, and W. Massa. Phase transitions in the perovskite methylammonium lead bromide, $CH_3ND_3PbBr_3$. *J. Solid State Chem.*, 176(1):97–104, 2003. doi: 10.1016/S0022-4596(03)00352-9.

[65] E. Tenuta, C. Zheng, and O. Rubel. Thermodynamic origin of instability in hybrid halide perovskites. *Sci. Rep.*, 6:37654, 2016. doi: 10.1038/srep37654.

[66] A. S. Thind, X. Huang, J. Sun, and R. Mishra. First-principles prediction of a stable hexagonal phase of $CH_3NH_3PbI_3$. *Chem. Mater.*, 29(14):6003–6011, 2017. doi: 10.1021/acs.chemmater.7b01781.

[67] P. Umari, E. Mosconi, and F. De Angelis. Relativistic GW calculations on $CH_3NH_3PbI_3$ and $CH_3NH_3SnI_3$ perovskites for solar cell applications. *Sci. Rep.*, 4:4467, 2014. doi: 10.1038/srep04467.

[68] P. Whitfield, N. Herron, W. Guise, K. Page, Y. Cheng, I. Milas, and M. Crawford. Structures, phase transitions and tricritical behavior of the hybrid perovskite methyl ammonium lead iodide. *Sci. Rep.*, 6:35685, 2016. doi: 10.1038/srep35685.

[69] S. Wozny, M. Yang, A. M. Nardes, C. C. Mercado, S. Ferrere, M. O. Reese, W. Zhou, and K. Zhu. Controlled humidity study on the formation of higher efficiency formamidinium lead triiodide-based solar cells. *Chem. Mater.*, 27(13):4814–4820, 2015. doi: 10.1021/ja511132a.

[70] W. S. Yang, B.-W. Park, E. H. Jung, N. J. Jeon, Y. C. Kim, D. U. Lee, S. S. Shin,

J. Seo, E. K. Kim, J. H. Noh, and et al. Iodide management in formamidinium-lead-halide-based perovskite layers for efficient solar cells. *Science*, 356(6345):1376–1379, 2017. doi: 10.1126/science.aan2301.

[71] Y.-Y. Zhang, S. Chen, P. Xu, H. Xiang, X.-G. Gong, A. Walsh, and S.-H. Wei. Intrinsic instability of the hybrid halide perovskite semiconductor $CH_3NH_3PbI_3$. *Chin. Phys. Lett.*, 35(3):036104, 2018.

[72] C. Zheng and O. Rubel. Ionization energy as a stability criterion for halide perovskites. *J. Phys. Chem. C*, 121(22):11977–11984, 2017. doi: 10.1021/acs.jpcc.7b00333.

[73] F. Zheng, L. Z. Tan, S. Liu, and A. M. Rappe. Rashba spin-orbit coupling enhanced carrier lifetime in $CH_3NH_3PbI_3$. *Nano Lett.*, 15(12):7794–7800, 2015. doi: 10.1021/acs.nanolett.5b01854.

[74] H. Zhou, Q. Chen, G. Li, S. Luo, T. B. Song, H. S. Duan, Z. Hong, J. You, Y. Liu, and Y. Yang. Interface engineering of highly efficient perovskite solar cells. *Science*, 345(6196):542–546, 2014.

# Chapter 6

# Instability study on Aziridinium lead iodide perovskite

**Author contributions:** Kangze Ren, I and Dr. Oleg Rubel together conceived this project with valuable guidance from Dr. Michael A. Brook. The calculations and data analysis were conducted by Kangze Ren and me. Kangze Ren, Dr. Oleg Rubel and I wrote the manuscript. All authors reviewed the manuscript. This Chapter is submitted to a peer-reviewed journal.

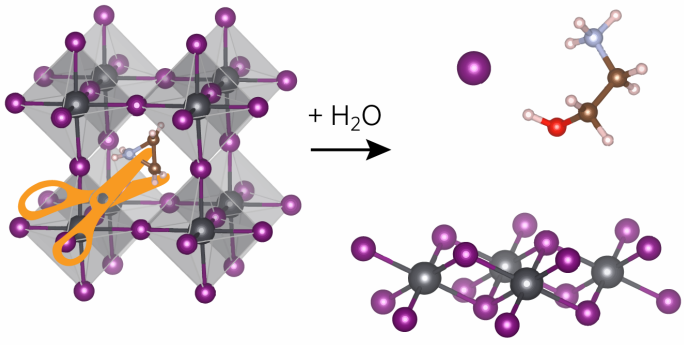

## 6.1 Introduction

The power conversion efficiency of perovskite solar cells surpassed 24%[29] only a decade after the first report of a perovskite solar cell[16]. However, the lifetime of perovskite solar cells is still constrained by instability issues[24]. Environmental factors such as moisture[28], ultraviolet light[39], oxygen[4], and thermal stress[25] are believed to be the major causes for degradation of perovskite solar cells. The vulnerability of perovskites is related to the intrinsic instability of lead halide perovskites[41,44] and $CH_3NH_3PbI_3$ in particular. This challenge inspired a search for intrinsically stable perovskite materials with promising photovoltaic properties.

The ionization energy of the cation on site $A$ in a general perovskite structure $AMX_3$ can be used as one of the indicators for predicting stability of hybrid halide perovskites[45]. Cations with a lower ionization energy tend to form more stable perovskite structures. Zheng and Rubel[46] proposed a new perovskite material that features a three-membered ring cation, aziridinium $CH_2CH_2N^+H_2$ ($Azr^+$) shown in Fig. 6.1(a), with the ionization energy lower than methylammonium (MA). According to first-principle calculations[40,46], the decomposition reaction

$$AzrPbI_3 \rightarrow AzrI + PbI_2 \tag{6.1.1}$$

is energetically unfavourable. Thus, $AzrPbI_3$ was proclaimed to be more stable than $MAPbI_3$[46], which inspired follow up theoretical studies[20,21,22,40].

Although, on the theoretical level the perovskite structure of $AzrPbI_3$ seems to be stable, the $Azr^+$ ring itself is very volatile[3], which raises a concern about feasibility of $AzrPbI_3$ synthesis. In addition to volatility, according to Rycke et al.[35], a three-membered $Azr^+$ ring is 17,000 times more reactive than a four-membered azetidinium ring. The high reactivity of $Azr^+$ can be attributed to its high ring strain energy. Aziridine ring has a ring strain of 26.7 kcal/mol[7], which was measured with reference to the piperidine structure. A reason for the high strain energy in $Azr^+$ is similar to that in cyclopropane. In the case of cyclopropane,

the C−C−C bond angle of 60° is far from the ideal 109.5° for bonds between atoms with $sp^3$ hybridized atomic orbitals. A reduced hybridization between orbitals weakens the C−C bonds making three-membered rings prone to opening[32]. In the case of aziridine, the ring opening reaction is even more favourable because amide anions are better leaving groups[33].

The neglect of the $Azr^+$ ring-open effect in our previous study[46] puts in question the feasibility of the proposed $AzrPbI_3$ structure as a potential photovoltaic material. Here we use a density-functional theory (DFT) to further investigate stability of the $Azr^+$ perovskite. We show that the $Azr^+$ ring opening and its reaction with water hinder the synthesis of the previously proposed perovskite structure of $AzrPbI_3$.

## 6.2 Method

The perovskite structure $AzrPbI_3$ discussed in the current work is the same structure which was reported earlier[46]. The previously reported structure of the AzrI salt[46] was created from the parent structure of formamidinium iodide[31]. The organic compound $CH_3CHNH_2$ inside the open-ring $AzrPbI_3$ was adopted from the most stable $(C_2H_6N)^+$ isomorph[1]. The hexagonal structure of $AzrPbI_3$ is inspired by the structure of $\delta$-$HC(NH_2)_2PbI_3$[38]. The crystal structure of 2-hydroxyethylammonium iodide was taken from Ref.[15]. The crystallographic information files (CIF files) with the atomic structure of solids and molecules used in this work can be accessed through the Cambridge crystallographic data center (CCDC). $AzrPbI_3$ closed-ring cubic, open-ring cubic, and open-ring hexagonal phases correspond to CCDC deposition numbers 1948430, 1947458, and 1947836, respectively. The structures of 2-iodoethanamine, a linear chain polyethylenimine, and 2-hydroxyethylammonium iodide can be found under CCDC deposition numbers 1948318, 1947839, and 1948421, respectively.

All of the electronic properties, as well as the total energy calculations have been accomplished in the framework of DFT[13,14] with the Perdew-Burke-Ernzerhof[30] (PBE) exchange-correlation functional. Dispersion interactions were incorporated at the DFT-D3 level[11].

Calculations were performed with Vienna ab initio simulation program (VASP) and projector augmented-wave potentials[2,17,18]. A conjugate-gradient algorithm was used to achieve ion relaxation by minimizing forces below 2 meV/Å together with the cell shape and cell volume relaxation. Monopole, dipole and quadrupole corrections implemented in VASP were used to eliminate leading errors and acquiring accurate total energies of all charged ions[23,27]. The cut-off energy for a plane wave expansion was set at 500 eV. The total energy convergence was set at 0.1 $\mu$eV.

For reciprocal space integration, a $4 \times 2 \times 2$ Monkhorst-Pack grid[26] was applied for 2-hydroxyethylammonium iodide solid, $4 \times 4 \times 4$ for cubic $AzrPbI_3$ perovskite structures, $3 \times 3 \times 3$ for hexagonal open-ring phase of $AzrPbI_3$,$2 \times 3 \times 3$ for $NH_2(CH_2)_2I$(s), $3 \times 3 \times 2$ for $PbI_2$, $3 \times 3 \times 6$ for AzrI, and a single $\Gamma$ point for all gas phase molecules.

## 6.3 Results and discussion

### 6.3.1 Aziridinium ring opening inside the $PbI_3$ framework

First we investigate the $Azr^+$ ring stability within the $PbI_3$ cage. It is assumed that the $PbI_3$ cage deforms but remains intact as the $Azr^+$ cation undergoes the ring opening transformation. There are multiple possible open-ring $Azr^+$ structures. Barone et al.[1] reported seven isomers as candidates for the $Azr^+$ ring opening. Among those seven alternative structures, $CH_3CHNH_2{}^+$ (shown in Fig. 6.1b) possessed lowest total energy based on molecular electronic structure calculations and was selected as the open-ring $Azr^+$ structure in our study.

The $Azr^+$ ring strain within $PbI_3$ framework was evaluated as the total energy difference

$$\Delta E = E(\text{c-AzrPbI}_3) - E(\text{o-AzrPbI}_3), \tag{6.3.1}$$

where $E$(c-$AzrPbI_3$) and $E$(o-$AzrPbI_3$) refer to the closed-ring and open-ring structures,

respectively. The resultant $\Delta E$ is 0.7 eV per formula unit (f.u.) for the cubic phase. (The cubic structure corresponds to a high temperature stable phase for hybrid halide perovskites[34,43].) Although the lattice energies of different crystal structures, e.g. cubic, orthorhombic, hexagonal are not calculated, it is still reasonable to estimate that the lattice energies decrease from cubic phase to hexagonal phase due to smaller lattice constants. Our result is less than the aziridine ring strain of 26.7 kcal/mol (1 eV/f.u.) reported in Ref.[7] due to an additional chemical strain imposed on the cation by the $PbI_3$ cage. The magnitude of $\Delta E$ is far beyond a PBE chemical uncertainty ($\pm$0.03 eV/atom[12]) and large enough to rule out existence of the closed-ring $AzrPbI_3$ perovskite.

The next question is whether the open-ring perovskite structure of $AzrPbI_3$ is stable and potentially useful for photovoltaics. The size of $Azr^+$ in the open-ring configuration is relatively large. The hexagonal phase better accommodates organic cations of the size greater than MA. Both cubic and hexagonal phases of open-ring $AzrPbI_3$ are shown in Fig. 6.1(d,e). The hexagonal phase has lower total energy by approximately 0.1 eV/f.u., which is within the DFT-PBE uncertainty and is of the same order as the final temperature corrections to the enthalpy and entropy of hybrid halide perovskites[41]. The energy difference is, therefore, not conclusive to establish the room-temperature phase of open-ring $AzrPbI_3$ with certainty.

The band gap of open-ring cubic and hexagonal structures of $AzrPbI_3$ was calculated at the DFT-PBE level without taking spin-orbit coupling into account. This approach yields a reliable estimate for the band gaps of halide perovskites due to cancelation of errors coming from the DFT semilocal exchange-correlation functional and omission of relativistic effects[8]. The open-ring cubic and hexagonal structure have the band gap of 1.6 and 2.1 eV, respectively. The band gap of the hexagonal structure is too far from the optimum range of $1.1 - 1.5$ eV for single-junction solar cells set by the Shockley-Queisser limit[36].

### 6.3.2 Aziridinium ring opening without maintaining the $PbI_3$ framework

Next, we address the stability of an open-ring $AzrPbI_3$ phase. We investigate three decomposition pathways which feature the $Azr^+$ ring opening and rupture of the $PbI_3$ framework. The first structure is a linear polyethylenimine, the product of a suggested polymerization shown in Fig. 6.1(f). The second structure is 2-Iodoethanamine shown in Fig. 6.1(g), generated under a halide nucleophilic ring-opening reaction. The third structure is 2-hydroxyethylammonium shown in Fig. 6.1(h), which is a water-induced product serving as the mean of testing the water resistance. The most favourable product, which features the lowest total energy, shall be determined via DFT calculations.

#### Aziridinium polymerization

Aziridine in acid medium generates $Azr^+$ which undergoes polymerization thanks to its minimum steric hindrance[10]. Interactions between $Azr^+$ and aziridine result in a polymerization reaction with a branched polyethylenimine as a product[9]. Due to the high similarity in chemical structure and similar thermodynamic/kinetic feasibility for polymerization with aziridine, we assume polymerized product of $Azr^+$ is similar to the polymerized product of aziridine, a branched linear polyethylenimine.

Here, we choose to calculate the total energy of linear polyethylenimine shown in Fig. 6.1(f) due to its simple structure and compatibility with periodic boundary conditions imposed by VASP. The linear polyethylenimine shares a similar chemical structure as branch polyethylenimine. The decomposition pathway is

$$AzrPbI_3(s) \rightarrow (C_2H_5N)_n(s) + HI(g) + PbI_2(s), \tag{6.3.2}$$

where $AzrPbI_3(s)$ refer to the hexagonal open-ring phase. The total energy of products in this reaction is 1.6 eV above the total energy of $AzrPbI_3(s)$. This result rules out the polymer chain as a viable decomposition product.

**Halide nucleophilic attack**

The $Azr^+$ ion can be considered as an activated aziridine, which easily undergoes ring opening reaction depending on the nature of nucleophiles[33]. Cerichelli and Luchetti[5] suggest that the protonation of nitrogen is potentially accountable for ring opening. Nucleophilic reactions with hydrogen protonated $Azr^+$ were studied in Refs.[3,6] that feature a halide ion attacking on the C and liberating $ICH_2H_2CNH_2$ from the ring. The resultant product iodoethylamine ($NH_2(CH_2)_2I$) is inspired by structures presented in Refs.[3,6]. Several alternative arrangements of solid iodoethylamine were studied, and the lowest energy structure is shown in Fig. 6.1(g).

The corresponding decomposition pathway can be expressed as

$$AzrPbI_3(s) \rightarrow NH_2(CH_2)_2I(s) + PbI_2(s). \tag{6.3.3}$$

The total energy difference of products in this reaction is 0.9 eV above the $AzrPbI_3$ hexagonal open-ring phase. This result shows iodoethylamine is not a favourable product for the decomposition reaction. Silva and Goodman[37] has done a similar study on halide induced $Azr^+$ ring opening. In Silva and Goodman's study, the energy difference between the threememebered ring and halide open-ring structure is very close. One group of data from Silva also shows that the closed-ring $Azr^+$ halide is more stable than the open-ring $Azr^+$ halide. In other words, Silva and Goodman's finding further confirms that the structure induced by nucleophilic ring opening reaction is not as favourable as the ring rupturing in the $PbI_3$ framework.

**Reaction with water**

It is critical to analyze degradation mechanisms that involve water for determining the stability of halide perovskites. There are some ambiguities regarding the product of $Azr^+$ reaction with water. Bouyacoub et al.[3] proposed $H_2N^+(CH_2)_2OH_2$, whereas Kohrt et al.[15]

suggested $H_3N^+(CH_2)_2OH$. The two structures differ by the location of a hydrogen atom. Our total energy calculations suggest the second structure as the most favourable product [Fig. 6.1(h)]. Hydroxyethylammonium ($H_3N^+(CH_2)_2OH$) is known to the perovskites community as a precursor for deficient perovskites[19,42]. This cation is too large to form stoichiometric perovskite structures, but it can fill in for a $(Pb{-}I)^+$ vacancy in perovskites.

The reaction with water can be expressed as

$$AzrPbI_3(s) + H_2O(g) \rightarrow NH_3(CH_2)_2OHI(s) + PbI_2(s). \tag{6.3.4}$$

The total energy difference for this reaction is 0.7 eV in favour of the right hand side. This result indicates that the open-ring $AzrPbI_3$ is unstable in the moist environment.

## 6.4 Conclusion

The stability of a recently-proposed aziridinium lead iodide perovskite was investigated using density functional theory. The work was motivated by a high ring strain associated with the three-membered aziridinium cation. We show that opening the aziridinium ring within the $PbI_3$ cage liberates the energy of about $0.7 - 0.8$ eV per formula unit. This result rules out the possibility of an experimental synthesis of the aziridinium lead iodide perovskite material. In an open-ring configuration, the aziridinium lead iodide would likely adopt a hexagonal structure rather than a perovskite structure. (The stable hexagonal structure shows that both [$PbI_6$] octahedral and all-corner sharing 3D network do not exist.) However, the difference in the total energy of 0.1 eV between the two alternative structures is within the chemical uncertainty of an exchange-correlation functional used. The open-ring aziridinium cation is unstable in moist environments. It can readily react with water forming a hydroxyethylammonium ion. Even though this cation is stable, it is too large for stoichiometric lead halide perovskite structures.

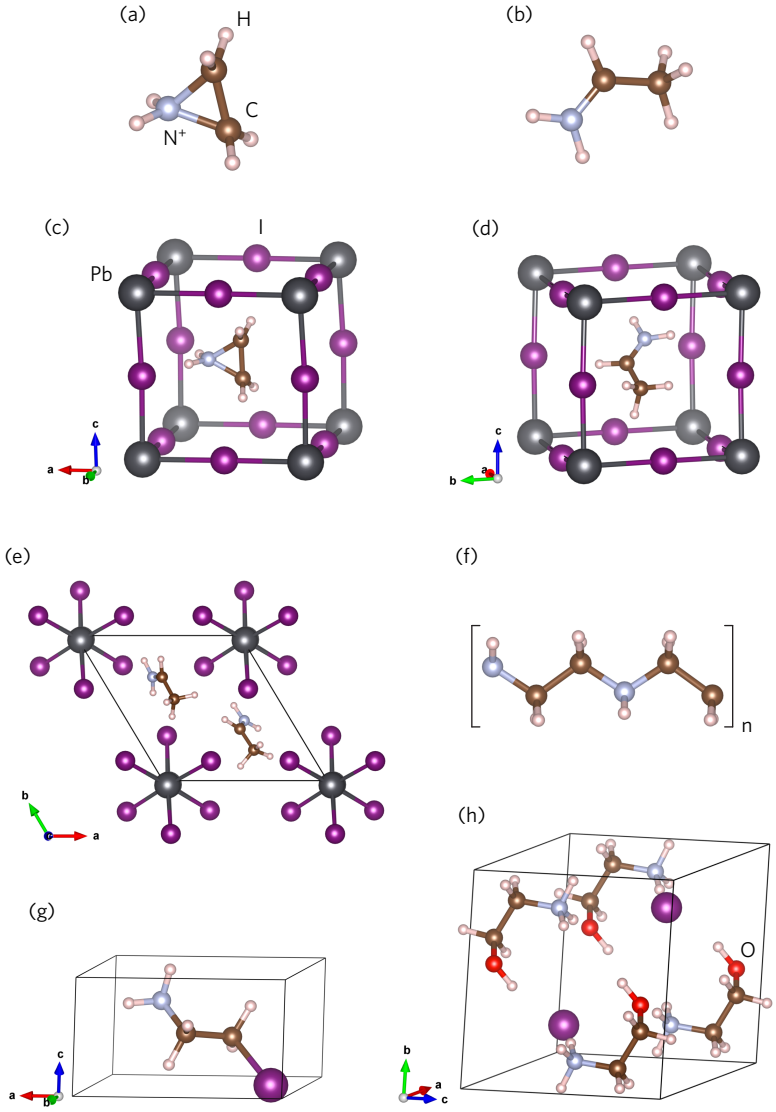


Figure 6.1: Structures used in total energy DFT calculations. (a) Three-membered ring $Azr^+$. (b) Most stable open-ring configuration for $Azr^+$ (The charge is adopted by extracting one electron from the neutral molecule during the calculations which is not shown in figure.) (c) Crystal structure of $AzrPbI_3$ in a closed-ring cubic phase. (d) Open-ring cubic phase of $AzrPbI_3$. (e) Open-ring hexagonal phase of $AzrPbI_3$. (f) Linear chain polyethylenimine $(C_2H_5N)_n$. (g) 2-Iodoethanamine (ArzI, open-ring configuration). (h) 2-Hydroxyethylammonium iodide.

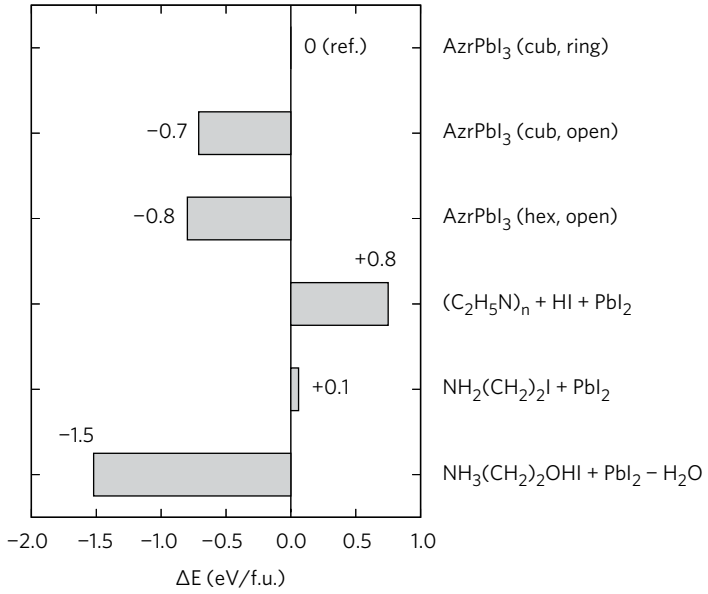


Figure 6.2: DFT total energies of various products associated with decomposition of $AzrPbI_3$ taken relative to the closed-ring cubic phase. Negative values correspond to stable products. The chemical accuracy of DFT-PBE is about $\pm 0.15$ eV/f.u.

# Bibliography

[1] V. Barone, F. Lelj, P. Grande, and N. Russo. Structures and relative stabilities of $[C_2H_6N]^+$ ions: A non-empirical and MNDO study. *J. Mol. Struct.-Theochem.*, 124 (3-4):319–324, 1985. doi: 10.1016/0166-1280(85)80019-1.

[2] P. E. Blöchl. Projector augmented-wave method. *Phys. Rev. B*, 50(24):17953–17979, 1994. doi: 10.1103/physrevb.50.17953.

[3] A. Bouyacoub, Y. Jean, and F. Volatron. Hydrolysis of unsubstituted and alkyl-substituted aziridinium cations: selectivity and reaction mechanism (SN1 vs. SN2). *J. Mol. Struct.-Theochem.*, 371:51–57, Nov. 1996. doi: 10.1016/s0166-1280(96)04738-0.

[4] D. Bryant, N. Aristidou, S. Pont, I. Sanchez-Molina, T. Chotchunangatchaval, S. Wheeler, J. R. Durrant, and S. A. Haque. Light and oxygen induced degradation limits the operational stability of methylammonium lead triiodide perovskite solar cells. *Energy Environ. Sci.*, 9(5):1655–1660, 2016. doi: 10.1039/c6ee00409a.

[5] G. Cerichelli and L. Luchetti. Ring-opening reactions. stability and reactivity of aziridinum and azetidinium ions in solution. *J. Chem. Soc., Chem. Commun.*, (6):339, 1985. doi: 10.1039/c39850000339.

[6] M. D'hooghe, S. Catak, S. Stanković, M. Waroquier, Y. Kim, H.-J. Ha, V. V. Speybroeck, and N. D. Kimpe. Systematic study of halide-induced ring opening of 2-substituted aziridinium salts and theoretical rationalization of the reaction pathways. *Eur. J. Org. Chem.*, 2010(25):4920–4931, July 2010. doi: 10.1002/ejoc.201000486.

[7] T. Dudev and C. Lim. Ring strain energies from ab initio calculations. *J. Am. Chem. Soc.*, 120(18):4450–4458, May 1998. doi: 10.1021/ja973895x.

[8] J. Even, L. Pedesseau, J.-M. Jancu, and C. Katan. Importance of spin–orbit coupling

in hybrid organic/inorganic perovskites for photovoltaic applications. *J. Phys. Chem. Lett.*, 4(17):2999–3005, 2013. doi: 10.1021/jz401532q.

[9] T. Gleede, L. Reisman, E. Rieger, P. C. Mbarushimana, P. A. Rupar, and F. R. Wurm. Aziridines and azetidines: building blocks for polyamines by anionic and cationic ring-opening polymerization. *Polym. Chem.*, 10(24):3257–3283, 2019. doi: 10.1039/c9py00278b.

[10] E. J. Goethals, M. van de Velde, G. Eckhaut, and G. Bouquet. Polymerization and copolymerization of N-alkylaziridines. In *ACS Symposium Series*, volume 286, chapter 17, pages 219–229. American Chemical Society, 1985. doi: 10.1021/bk-1985-0286.ch017.

[11] S. Grimme, J. Antony, S. Ehrlich, and H. Krieg. A consistent and accurate ab initio parametrization of density functional dispersion correction (DFT-D) for the 94 elements H-Pu. *J. Chem. Phys.*, 132(15):154104, 2010. doi: 10.1063/1.3382344.

[12] G. Hautier, S. P. Ong, A. Jain, C. J. Moore, and G. Ceder. Accuracy of density functional theory in predicting formation energies of ternary oxides from binary oxides and its implication on phase stability. *Phys. Rev. B*, 85(15):155208, 2012. doi: 10.1103/PhysRevB.85.155208.

[13] P. Hohenberg and W. Kohn. Inhomogeneous electron gas. *Phys. Rev.*, 136:B864–B871, 1964. doi: 10.1103/PhysRev.136.B864.

[14] W. Kohn and L. J. Sham. Self-consistent equations including exchange and correlation effects. *Phys. Rev.*, 140(4A):A1133–A1138, 1965. doi: 10.1103/physrev.140.a1133.

[15] C. Kohrt, A. Spannenberg, and T. Werner. 2-hydroxyethylammonium iodide. *Acta Crystallogr. E*, 70(6):o628–o628, 2014. doi: 10.1107/s1600536814009581.

[16] A. Kojima, K. Teshima, Y. Shirai, and T. Miyasaka. Organometal halide perovskites as visible-light sensitizers for photovoltaic cells. *J. Am. Chem. Soc.*, 131(17):6050–6051, 2009.

[17] G. Kresse and J. Furthmüller. Efficient iterative schemes forab initiototal-energy calculations using a plane-wave basis set. *Phys. Rev. B*, 54(16):11169–11186, 1996. doi: 10.1103/physrevb.54.11169.

[18] G. Kresse and D. Joubert. From ultrasoft pseudopotentials to the projector augmented-wave method. *Phys. Rev. B*, 59(3):1758–1775, 1999. doi: 10.1103/physrevb.59.1758.

[19] A. Leblanc, N. Mercier, M. Allain, J. Dittmer, V. Fernandez, and T. Pauporté. Lead- and iodide-deficient $(CH_3NH_3)PbI_3$ (d-MAPI): The bridge between 2D and 3D hybrid perovskites. *Angew. Chem. Int. Ed.*, 56(50):16067–16072, 2017. doi: 10.1002/anie.201710021.

[20] Y. Li and K. Yang. High-throughput computational design of organic–inorganic hybrid halide semiconductors beyond perovskites for optoelectronics. *Energy Environ. Sci.*, 12(7):2233–2243, 2019. doi: 10.1039/c9ee01371g.

[21] D. Liu, Q. Li, J. Hu, H. Jing, and K. Wu. Predicted photovoltaic performance of lead-based hybrid perovskites under the influence of a mixed-cation approach: theoretical insights. *J. Mater. Chem. C*, 7(2):371–379, 2019. doi: 10.1039/c8tc04065f.

[22] D. Liu, Q. Li, J. Hu, R. Sa, and K. Wu. Photovoltaic performance of lead-less hybrid perovskites from theoretical study. *J. Phys. Chem. C*, 123(20):12638–12646, 2019. doi: 10.1021/acs.jpcc.9b02705.

[23] G. Makov and M. C. Payne. Periodic boundary conditions inab initiocalculations. *Phys. Rev. B*, 51(7):4014–4022, 1995. doi: 10.1103/physrevb.51.4014.

[24] L. Meng, J. You, and Y. Yang. Addressing the stability issue of perovskite solar cells for commercial applications. *Nat. Commun.*, 9(1):5265, 2018. doi: 10.1038/s41467-018-07255-1.

[25] I. Mesquita, L. Andrade, and A. Mendes. Temperature impact on perovskite solar cells under operation. *ChemSusChem*, 12(10):2186–2194, Apr. 2019. doi: 10.1002/cssc.201802899.

[26] H. J. Monkhorst and J. D. Pack. Special points for brillouin-zone integrations. *Phys. Rev. B*, 13(12):5188–5192, 1976. doi: 10.1103/physrevb.13.5188.

[27] J. Neugebauer and M. Scheffler. Adsorbate-substrate and adsorbate-adsorbate interactions of Na and K adlayers on al(111). *Phys. Rev. B*, 46(24):16067–16080, 1992. doi: 10.1103/physrevb.46.16067.

[28] G. Niu, W. Li, F. Meng, L. Wang, H. Dong, and Y. Qiu. Study on the stability of $CH_3NH_3PbI_3$ films and the effect of post-modification by aluminum oxide in all-solid-state hybrid solar cells. *J. Mater. Chem. A*, 2(3):705–710, 2014. doi: 10.1039/c3ta13606j.

[29] NREL. Best research-cell efficiency chart, 2019.

[30] J. P. Perdew, K. Burke, and M. Ernzerhof. Generalized gradient approximation made simple. *Phys. Rev. Lett.*, 77(18):3865–3868, 1996. doi: 10.1103/physrevlett.77.3865.

[31] A. A. Petrov, E. A. Goodilin, A. B. Tarasov, V. A. Lazarenko, P. V. Dorovatovskii, and V. N. Khrustalev. Formamidinium iodide: crystal structure and phase transitions. *Acta Crystallogr. E*, 73(4):569–572, 2017. doi: 10.1107/s205698901700425x.

[32] R. H. Petrucci, F. G. Herring, J. D. Madura, and C. Bissonnette. *General Chemistry: Principles and Modern Applications (10th Edition)*. Pearson Prentice Hall, 2010. ISBN 0132064529.

[33] F. D. Proft and P. Geerlings, editors. *Structure, Bonding and Reactivity of Heterocyclic Compounds*. Springer Berlin Heidelberg, 2014. doi: 10.1007/978-3-642-45149-2.

[34] C. Quarti, E. Mosconi, J. M. Ball, V. D'Innocenzo, C. Tao, S. Pathak, H. J. Snaith, A. Petrozza, and F. D. Angelis. Structural and optical properties of methylammonium lead iodide across the tetragonal to cubic phase transition: implications for perovskite solar cells. *Energy Environ. Sci.*, 9(1):155–163, 2016. doi: 10.1039/c5ee02925b.

[35] N. D. Rycke, O. David, and F. Couty. Assessing the rates of ring-opening of aziridinium and azetidinium ions: A dramatic ring size effect. *Org. Lett.*, 13(7):1836–1839, Apr. 2011. doi: 10.1021/ol200348k.

[36] W. Shockley and H. J. Queisser. Detailed balance limit of efficiency of p-n junction solar cells. *J. Appl. Phys.*, 32(3):510–519, 1961. doi: 10.1063/1.1736034.

[37] M. A. Silva and J. M. Goodman. Aziridinium ring opening: a simple ionic reaction pathway with sequential transition states. *Tetrahedron Lett.*, 46(12):2067–2069, 2005. doi: 10.1016/j.tetlet.2005.01.142.

[38] C. C. Stoumpos, C. D. Malliakas, and M. G. Kanatzidis. Semiconducting tin and lead iodide perovskites with organic cations: Phase transitions, high mobilities, and near-infrared photoluminescent properties. *Inorg. Chem.*, 52(15):9019–9038, 2013. doi: 10.1021/ic401215x.

[39] Y. Sun, X. Fang, Z. Ma, L. Xu, Y. Lu, Q. Yu, N. Yuan, and J. Ding. Enhanced UV-light stability of organometal halide perovskite solar cells with interface modification and a UV absorption layer. *J. Mater. Chem. C*, 5(34):8682–8687, 2017. doi: 10.1039/c7tc02603j.

[40] Q. Teng, T. Shi, and Y.-J. Zhao. First-principles study of aziridinium lead iodide perovskite for photovoltaics. *ChemPhysChem*, Dec. 2018. doi: 10.1002/cphc.201801033.

[41] E. Tenuta, C. Zheng, and O. Rubel. Thermodynamic origin of instability in hybrid halide perovskites. *Sci. Rep.*, 6(1):37654, 2016. doi: 10.1038/srep37654.

[42] C.-M. Tsai, Y.-P. Lin, M. K. Pola, S. Narra, E. Jokar, Y.-W. Yang, and E. W.-G. Diau. Control of crystal structures and optical properties with hybrid formamidinium and 2-hydroxyethylammonium cations for mesoscopic carbon-electrode tin-based perovskite solar cells. *ACS Energy Lett.*, 3(9):2077–2085, 2018. doi: 10.1021/acsenergylett.8b01046.

[43] P. S. Whitfield, N. Herron, W. E. Guise, K. Page, Y. Q. Cheng, I. Milas, and M. K. Crawford. Structures, phase transitions and tricritical behavior of the hybrid perovskite methyl ammonium lead iodide. *Sci. Rep.*, 6(1), 2016. doi: 10.1038/srep35685.

[44] Y.-Y. Zhang, S. Chen, P. Xu, H. Xiang, X.-G. Gong, A. Walsh, and S.-H. Wei. Intrinsic instability of the hybrid halide perovskite semiconductor $CH_3NH_3PbI_3$. *Chinese Phys. Lett.*, 35(3):036104, 2018. doi: 10.1088/0256-307X/35/3/036104.

[45] C. Zheng and O. Rubel. Ionization energy as a stability criterion for halide perovskites. *J. Phys. Chem. C*, 121(22):11977–11984, May 2017. doi: 10.1021/acs.jpcc.7b00333.

[46] C. Zheng and O. Rubel. Aziridinium lead iodide: A stable, low-band-gap hybrid halide perovskite for photovoltaics. *J. Phys. Chem. Lett.*, 9(4):874–880, Feb. 2018. doi: 10.1021/acs.jpclett.7b03114.

# Chapter 7

# Unraveling the Water Degradation Mechanism of $CH_3NH_3PbI_3$

**Author contributions:** I conceived this project with discussion with Dr. Oleg Rubel. All calculations and data analysis were conducted by myself with aid from Dr. Oleg Rubel. The manuscript was drafted by myself, and further refined by Dr. Oleg Rubel. During this project, Dr. Oleg Rubel gave valuable suggestions on analyzing $CsPbI_3$ for a comparison. This chapter was published in *The Journal of Physical Chemistry C*, 2019.

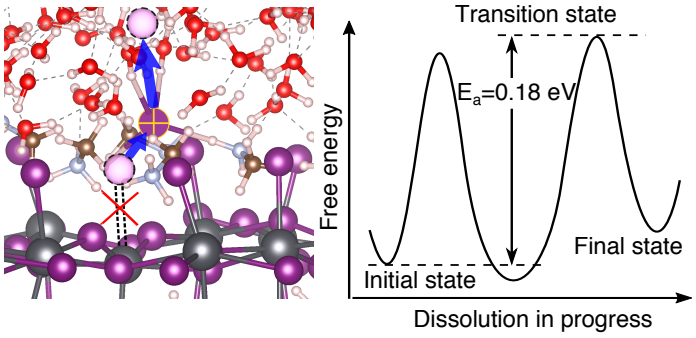

## 7.1 Introduction

The evolution of hybrid halide perovskite solar cells makes a contribution to the goal of replacing fossil fuels. High power conversion efficiency and low fabrication cost allow perovskite photovoltaics to be a tough competitor against traditional silicon solar cells. Since the inception of halide perovskite solar cells with 3.8% power conversion efficiency in 2009 [29], within 10 years of development, the world-record power conversion efficiency of perovskite photovoltaics has reached 25.2% according to the efficiency chart published by the National Renewable Energy Laboratory [1]. However, the poor stability of perovskite photovoltaic absorbers still remains unsolved and hinders the solar cells entering people's daily life.

Among the stimuli caused degradation of hybrid perovskite, water is confirmed to degrade $MAPbI_3$ [18]. Whereas, the role of water incorporation into $MAPbI_3$ remains a topic of debate, with conflicting results reported in the literature. It is found the moisture invasion fractures the connection of C−N in $CH_3NH_3$ (MA) and generate ammonia and hydrogen iodide [26,36]

$$CH_3NH_3PbI_3(s) \xrightarrow{H_2O} (-CH_2-) + NH_3(g) + HI(g) + PbI_2(s) \ . \tag{7.1.1}$$

Kakekhani et al. [24] propose a super-hydrous state of water incorporation in $MAPbI_3$ to explain deterioration of its photovoltaic properties in a moist environment. Besides, Philippe et al. [55] and Niu et al. [47] proposed a decomposition mechanism relating to the presence of $CH_3NH_3I$ (MAI) and $PbI_2$,

$$CH_3NH_3PbI_3(s) \xrightarrow{H_2O} CH_3NH_3I(aq) + PbI_2(s) \ . \tag{7.1.2}$$

In fact, two extreme water content conditions are discussed above: atmospheric moisture and liquid water. Both of the mechanisms are important. For fresh perovskite photovoltaics,

moisture degradation is obviously important for endurance. There are plenty of publications investigating the moisture-induced degradation of $CH_3NH_3PbI_3$ [2,3,16,30,43,57,60,64,67]. As photovoltaics, it has to be considered that different situations the cells will encounter, e.g. after a couple of years, cracks of the photovoltaic modules are inevitable[37]. At this stage, understanding of liquid water degradation mechanism becomes important. There are less investigations about the liquid water degradation pathway[9,10,46]. It is still unclear about the mechanism of $CH_3NH_3PbI_3$ degradation in liquid water, such as the energy barrier, decomposition details.

Key challenges in understanding the degradation mechanism of $MAPbI_3$ are the difficulties in determining the surface chemistry of the first few atomic layers of the pristine material without any exposure to ambient atmospheric conditions, and, conversely, the difficulties in measuring this same surface chemistry in real-time under exposure to realistic environments[26]. Molecular dynamics (MD) make it possible to explore the degradation mechanism at the atomic level. Caddeo et al.[9], Mosconi et al.[46] simulated the heterogeneous interface between water and $MAPbI_3$ to study its water degradation mechanism. Mosconi et al.[46] observed first MAI unit dissolved within 8.5 ps using an *ab initio* molecular dynamics (AIMD). Caddeo et al.[9] observed a fast dissolution of outermost MAI-terminated layers within 10 ps using classical molecular dynamics. Whereas, the details of the initial phase of the degradation process, such as energy barriers of corresponding steps, and the preference of ions leaving the surface are still missing. We performed AIMD simulation for water and $MAPbI_3$ interface aiming to clarify the degradation mechanism of $MAPbI_3$ in water. Contrary to previous reports of a short degradation time, our AIMD simulation of the heterogeneous interface renders no dissolution event happening within 12 ps. This phenomenon questions the immediacy of $MAPbI_3$ degradation in water.[18] During 12 ps standard AIMD simulation, we observed both $I^-$ and $MA^+$ ions trying to detach from the $MAPbI_3$ surface. As time passed by, the ions retrace back to the Pb−I framework cavity. Thus, the dissolution event reported in Mosconi et al.[46] could be an artefact due to a limited

simulation time of about 10 ps.

The ionic nature of $MAPbI_3$ [16,53] allows to draw a parallel to the research on simulation of NaCl dissolution. Intriguingly, Liu et al. [39] and Chen et al. [11] encountered the same situation when dissolving NaCl using MD. A single ionic dissolution is a rare event, which is unlikely to happen on the time scale of an AIMD simulation. Therefore, the dissolution needs to be "driven" artificially [11]. Metadynamics [8,23,34] is a powerful algorithm that can be used both for probing the free energy landscape and for accelerating rare events in systems described by complex Hamiltonians, at the classical or at the quantum level. Since the dissolution of $MAPbI_3$ in water is viewed as a rare event, it needs a much longer simulation time to capture the dissolution, and this finding raises a question about the validity of conclusions drawn from the relatively short 10 ps simulation [9].

In the current research, we propose the water degradation mechanism employing the capability of *ab initio* metadynamics which uses computational sands to fill the initial potential valley and to force the trapped system from the initial basin and explore the energy landscape. And it gives the possibility to describe the heterogeneous interface with a large system from the atomic level, dynamically and considering finite temperature effects. Hence, the method can accelerate and capture the dissolution process of $MAPbI_3$ in water. Here, the free energy surface (FES) of water dissolution $MAPbI_3$ can be reconstructed based on the historical computational sands added to the basin. The obtained FES suggests a relatively low energy barrier of the first step of the dissolution process. In addition, an analysis based on a thermodynamic cycle for dissolution $MAPbI_3$ explains the intrinsic water instability of $MAPbI_3$. The low dissolution energy barrier and spontaneous dissolving trend together unravel the fragile nature of $MAPbI_3$ when encountering water.

## 7.2 Computational method

Electronic structure calculations have been performed in the framework of DFT[28] and Perdew-Burke-Ernzerhof generalized gradient approximation[54] (GGA-PBE) for the exchange-correlation functional. Van der Waals correction is important for halide hybrid perovskite due to bare DFT method cannot provide correct dependence of van der Waals force[63,72]. When considering van der Waals correction for hybrid halide perovskites the predicted lattice parameters are more accurate than bare DFT calculations[63]. Among different van der Waals corrections, Li and Yang[35] employed both optb86B-vdW[27] and PBE+D3 method[17] to optimize structures. The results show that both the vdW functionals can give accurate crystal structure predictions. The PBE+D3 method acts even better than optb86B-vdW when comparing with experimental data. Except for the structural properties, our previous work[72] analyzed the polymorphism of $MAPbI_3$ employing different functionals including PBE+D3. We concluded that the PBE+D3 can accurately predict the trend of polymorphism of $MAPbI_3$. It indicates PBE+D3 can capture the total energy estimation very well. Hence, the PBE+D3 level van der Waals correction is considered for all calculations. Total energies of all compounds were obtained using the Vienna *ab initio* simulation program (VASP) and projector augmented-wave (PAW) potentials[5,31,32].

The phase separation energy difference $\Delta E_{\text{tot}}$ of $MAPbI_3$ and $CsPbI_3$ are adopted from our previous calculations[71]. For reciprocal space integration, $3 \times 3 \times 2$ Monkhorst-Pack grid[45] was used for tetragonal $MAPbI_3$, $4 \times 4 \times 3$ for hexagonal $PbI_2$ and $3 \times 6 \times 2$ for orthorhombic $CsPbI_3$. The convergence of $\Delta E_{\text{tot}}$ with respect to the k-mesh density was tested via doubling the density for investigated perovskite structures and corresponding decomposed structures. The convergence is better than 5 meV. The cutoff energy for a plane wave expansion was set at 400 eV. The lattice constant and atomic positions were optimized such that residual forces acting on atoms did not exceed 2 meV/Å, and the residual hydrostatic pressure was less than 50 MPa.

For AIMD calculations, a semi-empirical scaling method[65,73] is used to achieve a finite-temperature structure of $MAPbI_3$ that is self-consistent with PBE functional with the van der Waals correction. According to scanning tunnelling electron microscopy studies of $MAPbI_3$[49,58], we selected a MAI-terminated (001) surface structure of tetragonal $MAPbI_3$. The $MAPbI_3$ slab was modelled as $2 \times 2$ in plane per-optimized tetragonal supercell with the thickness of 7 atomic layers spaced by 18.6 Å filled by water molecules (see Fig. 7.1). The number of water molecules embedded is 158 which is obtained based on the experimental liquid water density. The dimension of the periodic cell are $a = b = 17.72$ Å which corresponds twice of the size of tetragonal $MAPbI_3$. In total, we have $c = 38.35$ Å for the heterogeneous structure. In order to obtain initial randomization of the atomic positions, we performed a standard AIMD simulation in two stages: pre-heating followed by a fixed temperature relaxation. Pre-heating from 0 to 300 K was performed in 700 steps (step size of 1 fs) using a linear ramp-up function (VASP tag SMASS = $-1$). Velocities were scaled every 20 MD steps. Although the orientations of $MA^+$ cations on the surface are anisotropic after this two-stage relaxation, we noticed the $-NH_3{}^+$ groups of $MA^+$ ions are attracted by oxygen atoms from adjacent water molecules during relaxation. Accuracy of computed Hellmann-Feynman forces was determined by the energy convergence criterion of $10^{-6}$ eV. Only one $k$ point at $\Gamma$ was used to sample the Brillouin zone. Atomic positions and velocities at the end of the preheating stage were taken as the input for the fixed temperature relaxation. The fixed temperature relaxation was conducted at 300 K for $\sim 9.8$ ps (step size of 1 fs). A Nosé–Hoover thermostat[21,48] was used to stabilize the temperature (VASP tag SMASS = 0). Atomic positions during AIMD were stored every 20 steps. Crystallographic information files (CIF) with atomic structures used in calculations can be accessed through the Cambridge crystallographic data centre (CCDC deposition numbers 1919295−1919299).

Metadynamics was applied to accelerates the rare events of the heterogeneous interface (VASP tag MDALGO = 21). It is realized by augmenting the system Hamiltonian $\tilde{H}(t)$ with a time-dependent bias potential $\tilde{V}(t, \xi)$ which acts on selected collective variables

$\xi = \{\xi_1, \xi_2, ..., \xi_m\}$

$$\tilde{H}(t) = H + \tilde{V}(t, \xi) \ , \tag{7.2.1}$$

where $H$ stands for the original Hamiltonian of unbiased system. $\tilde{V}(t, \xi)$ is defined as a sum of Gaussian hills with height $h$ and width $w$,

$$\tilde{V}(t, \xi) = h \sum_{i=1}^{\lfloor t/t_{\mathrm{G}} \rfloor} \exp \left[ -\frac{|\xi^{(t)} - \xi^{(i \cdot t_G)}|^2}{2w^2} \right] \ . \tag{7.2.2}$$

During the metadynamic simulation, $\tilde{V}(t, \xi)$ is updated by adding a new Gaussian with a time increment $t_{\mathrm{G}}$ which is set to 100 fs. A collective variable (CV) is a function of the particle positions. We employed two CVs in the current metadynamics. The first CV ($\xi_1$) is defined as the coordination number

$$\xi_1 = \sum_{i=1}^{M} \frac{1 - (q_i/c_i)^9}{1 - (q_i/c_i)^{14}} \tag{7.2.3}$$

of the departing $I^-$ (or N atom of monitored $MA^+$ during a paralleled $MA^+$ dissolution) with the rest $I^-$ (or N atoms of other $MA^+$) in the topmost complete layer of the surface. $M$ is the number of $I^-$ in the topmost layer except the monitored $I^-$ (or N atom in $MA^+$). $c_i$ is defined as the interatomic distance between the monitored $I^-$ (or N atom in $MA^+$) and each rest of $I^-$ (or N atom in $MA^+$) in the initial state. $q_i$ is the on-the-fly interatomic distance between the monitored $I^-$(or N atom in $MA^+$) and each rest of $I^-$ (or N atom in $MA^+$) during the simulation.

The second CV ($\xi_2$) records the interatomic distance between the monitored $I^-$ and $Pb^{2+}$ underneath it. An estimate of the underlying free energy $A(\xi)$ can be obtained via a sufficiently long time simulation,

$$A(\xi) = \lim_{t \to \infty} \tilde{V}(t, \xi) + \text{const} \ . \tag{7.2.4}$$

The choice of coordination numbers and Pb−I distance as two CVs is because these CVs vary according to different dissolution stages. CV ($\xi_2$) directly indicates the dissolution process of the monitored $I^-$ ion. However, only CV ($\xi_2$) is not sufficient to tell the difference between the states of $I^-$ ion attached on the surface and further dissolution in water. CV ($\xi_1$) is able to reflect the bond breaks accompanying the leaving of $I^-$ ion. Combination with CV ($\xi_1$), it is clear to explore an intermediate state. Liu et al.[39] used different combinations of CVs and determined that the same settings as we used are the best combination to characterize the dissolution event.

After the standard $\sim$ 9.8 ps MD, the width of Gaussian hill is determined from a continuous 1.8 ps metadynamics which monitors the two CVs without adding hills. The amplitudes of these CVs in the reactant well indicate the width of the well[13], and we set $w = 0.11$. Considering our large system (more than 800 atoms) and the complexity of the dissolution procedure, we set $h = 0.026$ eV from IS to IM. After passing the IM state, we increased the Gaussian height to 0.052 eV. To characterize the hydrogen bonds between water molecules and $I^-$, we set the bonding searching range to 3.25 Å[25]. Plumed package[7] and Gnuplot were utilized to reconstruct and plot the FES of dissolution events. VESTA 3 package[44] was used to visualize crystal structures.

## 7.3 Results and discussion

### 7.3.1 Dissolution energy barrier estimation

In this section, it will be shown that $MAPbI_3$ dissolution is a complex multi-step process triggered by the initial departure of $I^-$ ions from the MAI-terminated surface. The choice of the MAI-terminated surface as a starting point is based on the scanning tunnelling microscopy topography observations of halide hybrid perovskite surface[49,58]. An intermediate state is identified as the departing ion is partially hydrated but still remains within proximity from the $MAPbI_3$ surface. Starting with an equilibrated configuration we performed

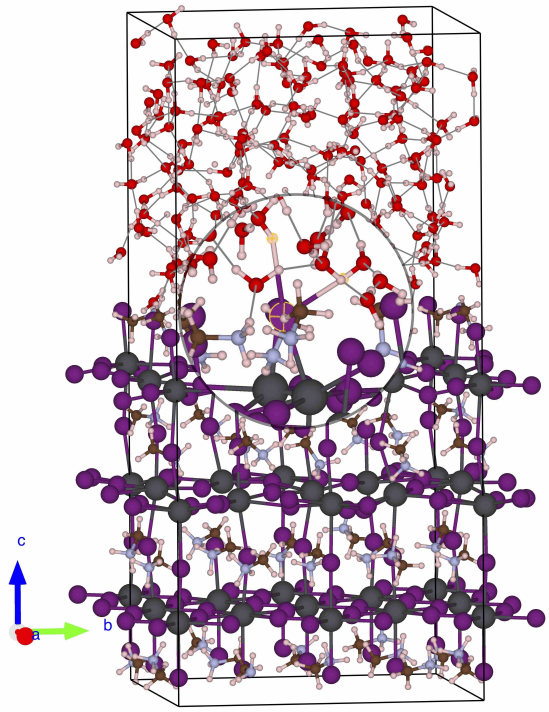


Figure 7.1: The initial state (IS) configuration of water/$MAPbI_3$ interface. Light pink represents hydrogen atoms. Red represents oxygen atoms. Brown represents carbon atoms. Light purple represents nitrogen atoms. Grey represents the lead atoms. Purple represents iodine atoms.

metadynamics using biasing variables (see Method section) aimed at obtaining the lowest free energy pathway for the detachment of $I^-$ from the $MAPbI_3$ surface.

We begin with the discussion of dissolving $I^-$ using the metadynamics. An equilibrated heterogeneous interface is taken as the initial structure for metadynamic simulation of the dissolution process. The observation of $I^-$ or $MA^+$ ion backtracking to Pb−I cavity, as previously discussed, is due to the trapping of the system in the initial FES basin using standard AIMD. The configuration trapped at this basin is named as the initial state (IS) shown in Fig. 7.1. In the IS, the monitored $I^-$ (labelled yellow) forms hydrogen bonds with two water molecules above it and bonds with a lead atom underneath it. Under the action of the metadynamic bias, the system is discouraged to revisit previously explored

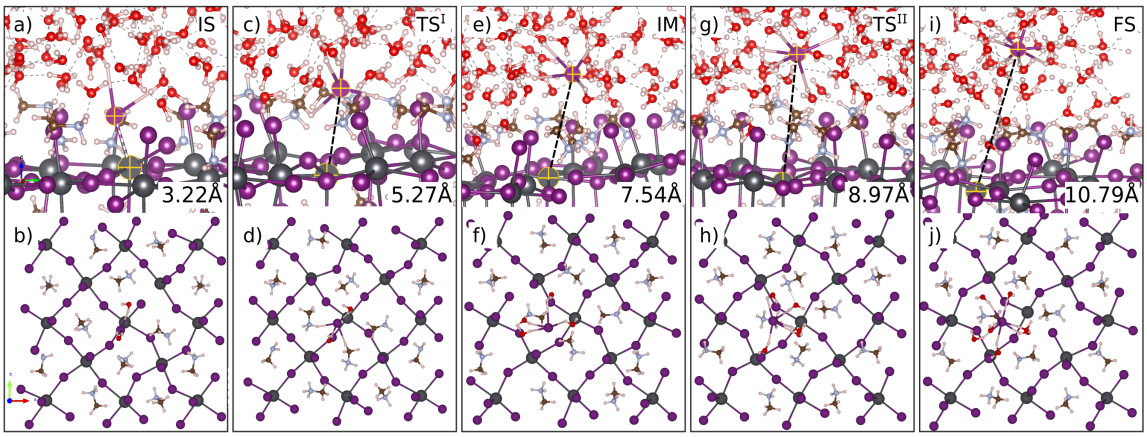


Figure 7.2: The initial state (IS), first transition state ($TS^{I}$), intermediate state (IM), second transition state ($TS^{II}$) and final state (FS) of the initial dissolution of $MAPbI_3$ in water, respectively. I−Pb interaction is marked as dashed line, and the value is shown in each configuration. It is clear to see that the I−Pb bond breaks at $TS^{I}$ and the monitored $I^-$ detaches surface at $TS^{II}$. Lower panel shows the conrresponding topview of each configuration.

spots. With accumulating the computational sands, the initial basin is filled and the system is forced to escape from the local minima. We observe the elongation of the I−Pb bond shown in Fig.7.2a and Fig.7.2b. After around 7 ps of metadynamic simulation, the system arrives at the first transition state ($TS^{I}$) of the dissolution process shown in Fig. 7.2c and Fig. 7.2d, the I−Pb bond breaks. At the transition state, the $I^-$ ion retains two hydrogen bonds with two water molecules. Besides, the $I^-$ forms bonds with a hydrogen atom on $-NH_3{}^+$ group of one $MA^+$, and with a hydrogen atom on $-CH_3$ group of the another $MA^+$. The interatomic distance of the monitored I−Pb bond streches from 3.22 Å at IS to 5.27 Å at $TS^{I}$. We continued the metadynamic simulation after conquering the $TS^{I}$. The lifted $I^-$ drifts away from the underneath $Pb^{2+}$. Meanwhile, neighbour $MA^+$ cations of the monitored $I^-$ drift towards the cavity. It is intriguing to find that the departing $I^-$ ion does not enter solvent immediately and the surrounding $MA^+$ cations do not leave the lattice following the $I^-$ ion. The heterogeneous interface evolves towards a state in which

the $I^-$ is partly hydrated, but remains trapped close to the surface illustrated in Fig. 7.2e and Fig. 7.2f. We assign this local energy minimum as an intermediate state (IM). The partially hydrated $I^-$ is in an adatom-like configuration. Upon transition from $TS^I$ to IM, the coordination number of the $I^-$ with the solvent water molecules increases from $\sim 2$ to $\sim 4$.

During the whole simulation, we find the system spends a long time at IM basin. The partly hydrated $I^-$ stays on top of one neighbour $MA^+$ cation due to an electrostatic attraction. Once the IM basin is filled, the system comes to the second transition state ($TS^{II}$), the corresponding configuration is shown in Fig. 7.2g and Fig. 7.2h. From IM to $TS^{II}$, the pulling forces from water molecules acting on the $I^-$ gradually overwhelm the interactions between the $I^-$ and underneath $MA^+$. The adatom-like $I^-$ ion detaches from the $MA^+$ cation. The number of water molecules in the hydration shell of $I^-$ increase to 5. The system needs to conquer the barrier of 0.22 eV to reach $TS^{II}$. This relatively larger energy barrier (compared with the initial 0.16 eV) is explained by breaking of the electrostatic attraction between the leaving $I^-$ and $MA^+$. After passing through the $TS^{II}$, the system evolves to a final state (FS) shown in Fig. 7.2i and Fig. 7.2j. We characterize the FS as a state where $I^-$ escapes from the $MAPbI_3$ surface and fully dissolves in water. In the FS, $I^-$ ion is coordinated by $\sim 7$ water molecules, consistent with both experimental and *ab initio* simulated coordination number of $6 - 9$[25,41]. The overall energy barrier for the initial dissolution event is obtained as the energy difference between the IS and $TS^{II}$ which is 0.18 eV.

We portray the FES of the dissolution process of $MAPbI_3$ in water in Fig. 7.3. The ease of the first dissolution event happening is determined by an energy barrier between IS and $TS^I$. Figure 7.3 suggests that the initial configuration needs to conquer 0.16 eV energy barrier to break the I−Pb bond in aqueous environment to reach $TS^I$. For comparison, Caddeo et al.[9] reported an energy barrier of 0.36 eV consisting of a layer-by-layer degradation of $MAPbI_3$ in water. Lin et al.[38] reported a larger energy barrier (greater than 0.5 eV) when

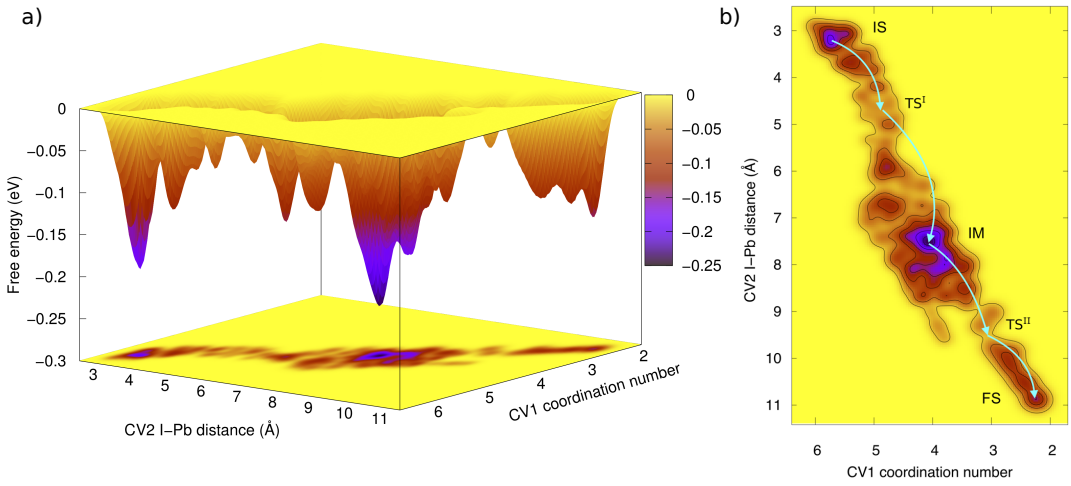


Figure 7.3: Reconstructed free energy surface of dissolution of $MAPbI_3$ in water from metadynamic simulation. a) gives the free energy landscape of the dissolution process of $MAPbI_3$ in water. b) is the contour plot of the free energy surface. Arrows point steps on the dissolution pathway.

dissolving an $I^-$ from $CsPbI_3$ surface in water. Releasing the $I^-$ is a competition between the hydration by water molecules and the electrostatic attraction to atoms on the surface and in the bulk of $MAPbI_3$. From a thermodynamic point of view, the dissolution phenomenon is an effect of compensating electrostatic energy stored in the $MAPbI_3$ surface by heat released from the hydration of the $I^-$. This process is further promoted by the entropy gain during $I^-$ entering water. Detailed thermodynamic analysis of the overall dissolution process is discussed in the following section. Both the hydrophilicity of $I^-$ and $MA^+$ ion and the intrinsic low electrostatic energy of $MAPbI_3$ [16,71] contribute to these very low energy barriers in Fig. 7.3.

Simulations of NaCl dissolution in water identify a clear preference for the dissolution

of $Cl^-$ as the initial step over $Na^+$ [39,50,68]. To investigate the preference of ions leaving $MAPbI_3$ surface at the beginning of the dissolution process, we performed an alternative metadynamic simulation where the dissolution starts with $MA^+$. The FES of dissolution of $MA^+$ is constructed and it renders a deeper energy basin ($\sim$ 0.31 eV), see Fig. S1 in Appendix A supporting materials. However, we only obtained the FES for the initial basin of the dissolution of $MA^+$. We find that the initial basin of $MA^+$ dissolution is much wider and deeper than the case of $I^-$ ion. Although we use relative large Gaussian height and weight, it is hard to explore the sequent stages of $MA^+$ dissolution in water. A larger Gaussian will accelerate the exploration, however, the sacrifice of accuracy is expected. Due to the capability of our facility and limited time, we stopped here for exploring the sequent FES of MA+ dissolution in water. The shape and rotational property of $MA^+$ ion may contribute to the large initial basin.

The difference of the initial basins indicates $I^-$ is relatively easier to dissolve in water. Although $-NH_3{}^+$ group of $MA^+$ is hydrophilic, the connected $-CH_3$ group is hydrophobic. When dissolving $MA^+$ in water, the hydrophobic $-CH_3$ group needs more space to settle in the water molecules[15]. Seeking for more space in water molecule network and breaking the interactions of $MA^+$ with surrounding ions in $MAPbI_3$ surface together lead to a higher energy barrier for the first dissolution of $MA^+$. As a result, the lower energy barrier suggests a priority of $I^-$ leaving the surface. Note that in the supporting information of Caddeo et al.[9], their simulation indicates that the first step of the dissolution MAI-terminated surface in water is releasing $MA^+$ at 5 ps. Differently, during our over 33.5 ps simulation time including equilibrium relaxation and metadynamics, we only observe the dissolution of one $I^-$ ion in water. Liu et al.[39] indicated a forcefield-based description of NaCl dissolution in water failed to capture a preference for $Cl^-$ over $Na^+$ dissolution. Limitations related to a proper description of bond breaking or formation in the empirical potential framework may contribute to this discrepancy.

It is worthy to note that we did not observe any decomposition of $MA^+$ cation during

the whole simulation. Compared with the high deprotonation energy (∼4.03 eV) of $MA^+$ cation[12], the low energy barrier of releasing $I^-$ suggests the initial degradation $MAPbI_3$ in water is the dissolution of MAI-terminated layer into water solute. It is meaningful to mention that the energy barrier of transformation of the $PbI_2$ 2D-planer layer to $PbI_2$ trigonal configuration is around 0.26 eV[14]. Considering the low energy barriers of dissolving $I^-$ in water as well the low energy barriers of decomposition of Pb−I layer, the overall degradation energy barrier of $MAPbI_3$ dissolution in water is less than 0.3 eV.

### 7.3.2 Thermodynamics of $MAPbI_3$ dissolution in water

Followed by the discussion of the initial process of $MAPbI_3$ dissolution in water, the thermodynamic analysis of the overall decomposition proceeds in this section. It is also intriguing to investigate how $CsPbI_3$ reacts with water as a comparison. The dissolution of $MAPbI_3$ via water can be described as follows:

$$CH_3NH_3PbI_3(s) \xrightarrow{\Delta G_{\text{diss}}} CH_3NH_3^+(aq) + I^-(aq) + PbI_2(s) \ . \tag{7.3.1}$$

Estimation of the change of the Gibbs free energy($\Delta G_T^\circ$) between the reactants and products is a standard approach for predicting whether a reaction or process will occur spontaneously. Combination of the density functional theory (DFT) calculation with additional thermodynamic data (see Chap. 7 in Ref. Sholl and Steckel[59]) is used to predict $\Delta G_T^\circ$ of phase separation of $MAPbI_3$[62]. Kye et al.[33] utilize an *ab initio* thermodynamic formalism with the effect of solution to investigate the behaviour of defects on phase stability of $CsPbI_3$. Here, we apply the combination of theoretical and experimental data to estimate the Gibbs free energy change ($\Delta G_{\text{diss}}$) of $MAPbI_3$ dissolution in water at temperature $T$ as stated in Eq. (7.3.1). According to Sholl and Steckel[59], $G_T^\circ$ can be expressed as,

$$G_T^\circ = E_{\text{tot}} + \tilde{\mu}_T^\circ \ . \tag{7.3.2}$$

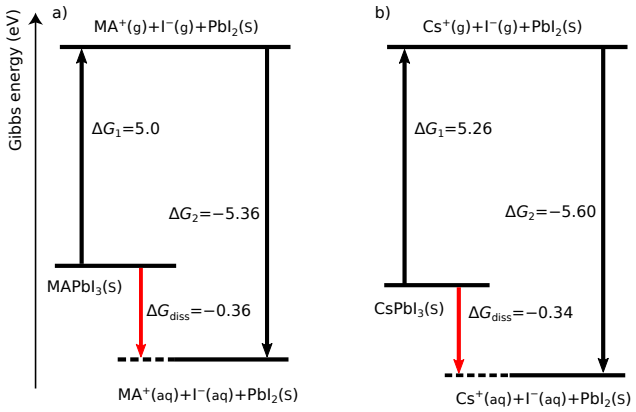


Figure 7.4: A thermodynamic cycle for the calculation of the dissolution Gibbs free energy change ($\Delta G_{\text{diss}}$) for (a) $MAPbI_3$ and (b) $CsPbI_3$ in water.

Here, $E_{\text{tot}}$ is the standard state enthalpy at zero temperature which is evaluated based on DFT total energy calculations. $\tilde{\mu}^{\circ}_{T}$ captures finite temperature effects on the chemical potentials of species involved which is evaluated from NIST-JANAF thermochemical tables as well as other experimental resources.

In order to capture $\Delta G_{\text{diss}}$ at finite temperature, we designed a two-step thermodynamic cycle as shown in Fig. 7.4a. The first step of the thermodynamic cycle is the dissociation of $MAPbI_3$(s) to oppositely charged ions $MA^+$(g) and $I^-$(g) and $PbI_2$(s),

$$CH_3NH_3PbI_3(s) \xrightarrow{\Delta G_1} CH_3NH_3^+(g) + I^-(g) + PbI_2(s) \ . \tag{7.3.3}$$

During this process, finite temperature effect on enthalpies and entropies of the system from solid inital state to intermediate gaseous state and $PbI_2$(s) are evaluated, respectively

$$\tilde{\mu}^{\circ}_{T} = H^{\circ}_{T} - H^{\circ}_{0\,\text{K}} - TS^{\circ}_{T} \ . \tag{7.3.4}$$

The addition of the resultant $\tilde{\mu}^{\circ}_{T}$ and calculated $E_{\text{tot}}$ generates $G^{\circ}_{T}$ of each species. Related thermodynamic properties of species involved in the first step of the thermodynamic cycle

Table 7.1: Electronic total energy $E_{\text{tot}}$ per formula unit (f.u.), $H_T - H_{0\text{K}}$, standard state entropy $S^\circ_T$, the chemical potential $\tilde{\mu}^\circ_T$ and standard Gibbs free energy $G^\circ_T$ in the first step of the thermodynamic cycle involving $MAPbI_3$/$MAPbCl_3$ dissolution in water. Here, we focus on room temperature $T = 298.15$ K.

| Species | $E_{\text{tot}}$ (eV/f.u.) | $H_T - H_{0\text{K}}$ (kJ/mol) | $S^\circ_T$ (J mol$^{-1}$ K$^{-1}$) | $\tilde{\mu}^\circ_T$ (eV/f.u.) | $G^\circ_T$ (eV/f.u.) |
|---|---|---|---|---|---|
| $MAPbI_3$ (s) | −50.93 | 44.79[a] | 374.13[a] | −0.69 | −51.62 |
| $MAPbCl_3$ (s) | −54.36 | 41.79[a] | 313.35[a] | −0.54 | −54.89 |
| $PbI_2$ (s) | −8.63 | 19.50[b] | 174.84[b] | −0.34 | −8.97 |
| $PbCl_2$ (s) | −10.73 | 19.50[b] | 136.0[b] | −0.22 | −10.95 |
| $MA^+$ (g) | −32.84 | 6.20[b] | 327.7[b] | −0.95 | −33.79 |
| $I^-$ (g) | −3.40 | 6.20[b] | 169.26[b] | −0.46 | −3.86 |
| $Cl^-$ (g) | −3.95 | 6.20[b] | 153.36[b] | −0.41 | −4.36 |
| $CsPbI_3$ (s) | −14.25 | 20.28[c] | 219.61[c] | −0.47[c] | −14.72 |
| $Cs^+$ (g) | 3.83 | 6.20[b] | 169.84[b] | −0.46 | 3.37 |
| MAI(s) | −42.36 | 22.25[d] | 159.7[d] | −0.26 | −5.69 |
| CsI(s) | −5.45 | 13.50[e] | 123.1[e] | −0.24 | −42.62 |

[a] Data obtained from Onoda-Yamamuro et al.[52]; [b] Data extracted from the NIST-JANAF thermochemical tables; [c] Data extracted from Hinuma et al.[20], Ong et al.[51]; [d] Data obtained from Yamamuro et al.[66]; [e] Data obtained from Rumble[56].

of $MAPbI_3$ dissolution in water are listed in Table 7.1. According to Table 7.1, it is feasible to calculate the change in Gibbs free energy $\Delta G_1$ for the first step

$$\Delta G_1 = G^\circ_{T,\text{MA}^+\text{(g)}} + G^\circ_{T,\text{I}^-\text{(g)}} + G^\circ_{T,\text{PbI}_2} - G^\circ_{T,\text{MAPbI}_3} \ . \tag{7.3.5}$$

The calculated $\Delta G_1 = 5.0$ eV is shown in Fig. 7.4a. The second step of the designed cycle of $MAPbI_3$ dissolution in water involves the hydration of $MA^+$(g) and $I^-$(g)

$$\text{MA}^+\text{(g)} + \text{I}^-\text{(g)} + \text{PbI}_2\text{(s)} \xrightarrow{\Delta G_2} \text{MA}^+\text{(aq)} + \text{I}^-\text{(aq)} + \text{PbI}_2\text{(s)} \ . \tag{7.3.6}$$

The chemical potentials of aqueous ions $\tilde{\mu}^\circ_T$(aq) in this step can be obtained via

$$\tilde{\mu}^\circ_T(\text{aq}) = \tilde{\mu}^\circ_T + \Delta H_{\text{hyd}} - T(S^\circ_T(\text{aq}) - S^\circ_T) \ . \tag{7.3.7}$$

Table 7.2: Hydration enthalpy $\Delta H^{\circ}_{\mathrm{hyd}}$, entropy $S^{\circ}_{T}(\mathrm{aq})$ of aqueous ions, and Gibbs free energy $G^{\circ}_{T}$ of species involved in the second step of the thermodynamic cycle of $MAPbI_3/MAPbCl_3$ dissolution in water at room temperature 298.15 K.

| Species | $\Delta H^{\circ}_{\mathrm{hyd}}$ (kJ/mol) | $S^{\circ}_{T}(\mathrm{aq})$ (J mol$^{-1}$ K$^{-1}$) | $\tilde{\mu}^{\circ}_{T}(\mathrm{aq})$ (eV/f.u.) | $G^{\circ}_{T}$ (eV/f.u.) |
|---|---|---|---|---|
| $MA^+$ (aq) | $-284.6^a$ | $142.7^b$ | $-3.33$ | $-36.17$ |
| $I^-$ (aq) | $-305.0^c$ | $111.3^d$ | $-3.44$ | $-6.84$ |
| $Cl^-$ (aq) | $-381.0^c$ | $56.5^d$ | $-3.44$ | $-8.0$ |
| $Cs^+$ (aq) | $-264.0^c$ | $133.1^d$ | $-3.08$ | 0.75 |

[a] Data obtained from Housecroft and Jenkins[22]; [b] Data extracted from Marcus and Loewenschuss[40]; [c] Data extracted from Smith[61]; [d] Data extracted from Rumble[56].

$S^{\circ}_{T}(\mathrm{aq})$ is the entropy of an aqueous ion. Decreased enthalpies and entropies due to hydration process contribute to the values of $G^{\circ}_{T,\mathrm{MA^+(aq)}}$ and $G^{\circ}_{T,\mathrm{I^-(aq)}}$. Related thermodyanmic properties of the second step are shown in Table 7.2.

The change of the Gibbs free energy of the second step

$$\Delta G_2 = G^{\circ}_{T,\mathrm{MA^+(aq)}} + G^{\circ}_{T,\mathrm{I^-(aq)}} - G^{\circ}_{T,\mathrm{MA^+(g)}} + G^{\circ}_{T,\mathrm{I^-(g)}} \tag{7.3.8}$$

amounts to $\Delta G_2 = -5.36$ eV. The strongly negative change of Gibbs free energy in the second step overcomes the Gibbs free energy gain in the first step. Combining the two-step Gibbs free energy change, we can obtain $\Delta G_{\mathrm{diss}} = \Delta G_1 + \Delta G_2 = -0.36$ eV. The negative $\Delta G_{\mathrm{diss}}$ of the dissolution $MAPbI_3$ in water at a finite concentration indicates the reaction in Eq. (7.3.1) would proceed spontaneously. The thermodynamic analysis of $MAPbI_3$ dissolution process suggests an intrinsic water instability of $MAPbI_3$. Although the negative $\Delta G_{\mathrm{diss}}$ reflects a spontaneity of a reaction, it only predicts the trend of the proposed reaction. According to Arrhenius equation, the rate of a reaction is controlled by the energy barrier, i.e., activation energy. A low activation energy indicates a high rate constant. The low activation energy obtained from metadynamic calculations for the $MAPbI_3$ degradation in water demonstrates the corresponding reaction will proceed quickly. In all, for the reaction of $MAPbI_3$ in water, the negative $\Delta G_{\mathrm{diss}}$ renders a thermodynamic

instability and the low energy barrier points to a kinetic instability.

It would be interesting to discuss water stability of $MAPbCl_3$. We also performed a thermodynamic analysis of $MAPbCl_3$ dissolution in water using the data in Tables 7.1 and 7.2. Compared with $\Delta H = -0.19$ eV in Fig. 7.5 for $MAPbI_3$ dissolution in water, $\Delta H = -0.17$ eV is obtained for $MAPbCl_3$ dissolution in water. The unfavourable reaction enthalpy for $MAPbCl_3$ decomposition[71] is compensated by the large hydration enthalpies of $MA^+$ and $Cl^-$ ions. Intriguingly, the calculated $T\Delta S = 0.07$ eV for $MAPbCl_3$ dissolution in water is smaller than $T\Delta S = 0.17$ eV for the case of $MAPbI_3$. The entropy term contributes less to the $\Delta G_{\text{diss}}$ for $MAPbCl_3$ dissolution in water. Finally, we obtain $\Delta G_{\text{diss}} = -0.24$ eV for $MAPbCl_3$ dissolution in water. This negative $\Delta G_{\text{diss}}$ renders an instability of $MAPbCl_3$ in water environment. The magnitude of $\Delta G_{\text{diss}}$ for $MAPbCl_3$ dissolution in water is smaller than that for the case of $MAPbI_3$. The smaller value indicates that $MAPbCl_3$ is less prone to dissolution in water than $MAPbI_3$.

Compared with a large number of discussions on the fragility of $MAPbI_3$ in water, the stability of $CsPbI_3$ in water recently attracts attention and is also under discussion. Lin et al.[38] indicated the water invasion triggered the phase transition of $CsPbI_3$ from a high-temperature cubic phase to a low-temperature orthorhombic phase and they found that water is adsorbed on the surface without penetrating the interior of $CsPbI_3$. The appearance of water molecules will create surface vacancies which further lower the free-energy barrier to nucleation of orthorhombic phase[38]. Conversely, Yuan et al.[69] observed the $CsPbI_3$ quantum dots degraded in a chamber with a wet gas flow. They confirmed the moisture was responsible for the degradation of these $CsPbI_3$ quantum dots. Here, we employ the two-step thermodynamic cycle to the case of $CsPbI_3$ dissolution in water to clarify these controversies.

The first step of the proposed thermodynamic cycle of dissolution $CsPbI_3$ in water is given as

$$CsPbI_3(s) \xrightarrow{\Delta G_1} Cs^+(g) + I^-(g) + PbI_2(s) \ . \tag{7.3.9}$$

Related thermodynamic properties of species involved in the first step of $CsPbI_3$ dissolution in water are listed in Table 7.1. We can obtain the Gibbs free energy change $\Delta G_1 = 5.26$ eV for Eq. (7.3.9). The thermodynamic cycle of $CsPbI_3$ is shown in Fig. 7.4b. The second step of $CsPbI_3$ dissolution in water involves the hydration of $Cs^+(g)$ and $I^-(g)$

$$Cs^+(g) + I^-(g) + PbI_2(s) \xrightarrow{\Delta G_2} Cs^+(aq) + I^-(aq) + PbI_2(s) \ . \tag{7.3.10}$$

Related thermodyanmic properties are shown in Table 7.2. Using Gibbs free energies in Tables 7.1 and 7.2, the change of the Gibbs free energy of the second step is estimated as $\Delta G_2 = -5.60$ eV. The overall $\Delta G_{\text{diss}} = \Delta G_1 + \Delta G_2 = -0.34$ eV for the dissolution $CsPbI_3$ in water

$$CsPbI_3(s) \xrightarrow{\Delta G_{\text{diss}}} Cs^+(aq) + I^-(aq) + PbI_2(s) \ . \tag{7.3.11}$$

The above discussion indicates that the orthorhombic $CsPbI_3$ is also prone to decompose in water. The thermodynamic analysis of $CsPbI_3$ dissolution in water corroborates the degradation of $CsPbI_3$ quantum dots observed by Yuan et al.[69]. The energy barrier of the dissolution process determines the rate of the reaction. Compared with the very low energy barrier (about 0.18 eV) for the initial dissolution of $MAPbI_3$, the relatively high energy barrier (greater than 0.5 eV[38]) for releasing $I^-$ into water from $CsPbI_3$ surface suggests a slow process of dissolution of $CsPbI_3$ which explains the differences in degradation rates at heterogeneous interfaces: water/$MAPbI_3$ *vs* water/$CsPbI_3$ observed by Lin et al.[38].

Zhang et al.[70] first used the energy differences obtained from DFT calculation to characterize the intrinsic instability of $MAPbI_3$ and $CsPbI_3$, considering a decomposition reaction of $MAPbI_3$ into solid state products

$$MAPbI_3(s) \rightarrow MAI(s) + PbI_2(s). \tag{7.3.12}$$

In Fig. 7.5 we show our calculated $\Delta E_{\text{tot}}$ for $MAPbI_3$ and $CsPbI_3$ which match well with

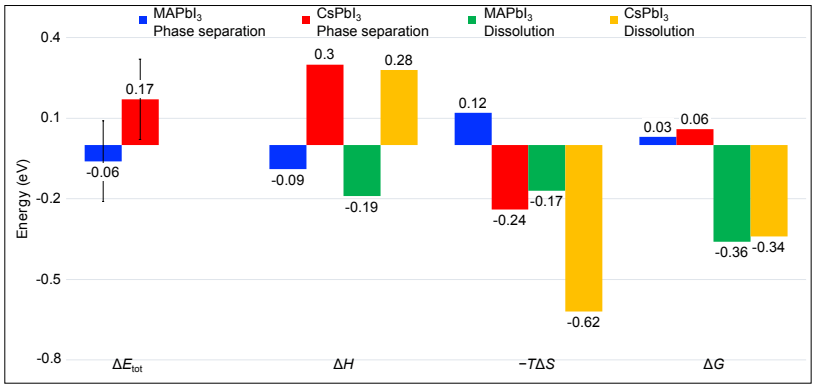


Figure 7.5: Thermodynamic quantities for decomposition of $MAPbI_3$ and $CsPbI_3$ via two alternative routes: a phase separation [Eq. (7.3.12)] or a dissolution in water [Eq. (7.3.1)]. $\Delta E_{\text{tot}}$ is the bare-DFT energy difference between products and the reactant (perovskite). The error bars indicate a chemical uncertainty of the DFT exchange-correlation functional (see text for details). $\Delta H$ is the enthalpy change at $T = 298.15$ K. $T\Delta S$ captures the entropy change during decomposition. $\Delta G$ is the resultant Gibbs free energy change of $MAPbI_3$ and $CsPbI_3$ phase separation and dissolution in water.

$\Delta E_{\text{tot}}$ from Zhang et al.[70]. According to Zhang et al.[70], a positive value of $\Delta E_{\text{tot}}$ corresponds to a stable perovskite structure. They proposed the entropy term of MAI is higher than that of $MAPbI_3$ which will further destabilize $MAPbI_3$. However, from the measurements of entropies of MAI and $MAPbI_3$ listed in Table 7.1, it clearly indicates a reverse trend. To note that, the entropy contribution of $PbI_2$ cannot be neglected. The overall entropy in reaction (7.3.12) decreases and stabilizes $MAPbI_3$ which has been indicated in Tenuta et al.[62]. The entropy gains during $CsPbI_3$ phase separation which is contrary to $MAPbI_3$. The enthalpy change of $CsPbI_3$ phase separation is large enough to overcome this entropy gain resulting in a positive $\Delta G$ that is slightly greater than the value of $MAPbI_3$.

The positive $\Delta G$ values for phase separation process in Fig. 7.5 indicate a feasibility of synthesis of $MAPbI_3$ and $CsPbI_3$ compounds. However, the result should be taken with caution, since the uncertainty in reaction energies obtained with Perdew, Burke, and Ernzerhof (PBE)[54] exchange-correlation functional is of the order of $\pm 0.03$ eV/atom[19]. With five atoms per perovskite formula unit ($MA^+$ is considered as one cation), the estimated

error is about ±0.15 eV as shown by the errorbars in Fig. 7.5. When considering a water environment, the Gibbs free energy change of the decomposition reaction mentioned above decreased by 0.39 eV and becomes strongly negative. This decrease is due to hydration of $MA^+/Cs^+$ and $I^-$ ions. The amount of enthalpy change during the designed two-step thermodynamic cycle for $MAPbI_3$ dissolution in water corresponding to Eq. (7.3.1) is negative (see $\Delta H$ in Fig. 7.5). This $\Delta H$ indicates the released energy during hydration process of $MA^+$ and $I^-$ in Eq. (7.3.6) overcomes the energy consumed in Eq. (7.3.3). It renders the dissolution $MAPbI_3$ in water is an exothermic reaction. The entropy gain during the dissolution of $MAPbI_3$ in water further lowers $\Delta G$ in Fig. 7.5, suggesting the dissolution process is thermodynamically preferable. Dissimilarly, a positive $\Delta H = 0.28$ eV for $CsPbI_3$ dissolving in water indicates the released energy during hydration process of $Cs^+$ and $I^-$ in Eq. (7.3.10) is less than the energy consumed during Eq. (7.3.9). This positive $\Delta H$ renders dissolution $CsPbI_3$ in water belongs to an endothermic reaction. Interestingly, a large entropy enhancement of dissolution $CsPbI_3$ in water brings down $\Delta G$ to a negative value, see in Fig. 7.5. This large entropy enhancement comes from the difference of a low entropy of orthorhombic $CsPbI_3$ and a high entropy of $Cs^+$(aq). The relative high entropy of $MAPbI_3$ and low entropy of $CsPbI_3$ in Table. 7.1 are consistent with the strong anharmonicity of $MAPbI_3$ and weak anharmonicity of $CsPbI_3$ recently discussed by Zhu and Ertekin[74] and Marronnier et al.[42]. Compared with $CsPbI_3$, the large hydration enthalpy of $MA^+$ ion and the entropy gain together direct the negative $\Delta G_{\text{diss}}$. In all, we can conclude that the large hydration enthalpies of $MA^+/Cs^+$ and $I^-$ and entropy enhancement as well as the low lattice energies of halide perovskite structures are responsible for the degradation of $MAPbI_3/CsPbI_3$ in water.

So far, we did not discuss an ionic activity $a_\pm$ of $CH_3NH_3I$ solution and its contribution $k_BT\ln(a_\pm)$ to a chemical potential term of an electrolyte when estimating $\tilde{\mu}^\circ_T$(aq). The

actual chemical potential of an electrolyte is expressed as

$$\mu_T \approx \tilde{\mu}_T^{\circ}(\text{aq}) + k_B T \ln(a_{\pm}). \tag{7.3.13}$$

The mean ionic activity $a_{\pm}$ of $CH_3NH_3I$ solution

$$a_{\pm} = (\gamma_{\pm} c/c^{\circ})^2 \tag{7.3.14}$$

is determined by its molar concentration $c$ relative to the concentration in standard state $c^{\circ} = 1$ M and the mean ionic activity coefficient $\gamma_{\pm}$, which accounts for non-ideality of the solution. Thermodynamic data listed in Table 7.1 correspond to $c = 1$ M. Bonner[6] and Belvèze et al.[4] reported $\gamma_{\pm}$ of MACl is 0.58 when $c = 1$ M. This value is taken as an estimation of $\gamma_{\pm}$ for MAI. The additional term $k_{\mathrm{B}} T \ln(a_{\pm})$ for MAI solution is estimated as $-0.028$ eV at $c = c^{\circ}$, which is relatively small considering $\Delta G_{\text{diss}} = -0.36$ eV. In a dilute solution limit ($c \ll 1$ M), the term $k_B T \ln(a_{\pm})$ becomes negative and drives the water decomposition reaction of $MAPbI_3$[62]. When decomposition proceeds to reach a finite concentration (*e.g.*, $c = c^{\circ}$), the $\Delta G_{\text{diss}}$ is no longer governed by $k_B T \ln(a_{\pm})$ but dominant by enthalpies and entropies of aqueous ions (see $\Delta H$ and $-T\Delta S$ of dissolution process in Fig. 7.5). Upon further dissolution, chemical potentials of the aqueous solution increase until $\Delta G_{\text{diss}} = 0$ eV, the solution is then saturated and the dissolution process ceases.

## 7.4 Conclusion

The water instability of $MAPbI_3$ is a major problem for the commercialization of perovskite photovoltaics. Explanations of the underline mechanism are under debate. Here, we use *ab initio* metadynamic method to reconstruct the free energy surface of the dissolution process of $MAPbI_3$ in explicit water. The predictive power of metadynamics unravels the pathway of water dissolving $MAPbI_3$ surface. One intermediate state and two transition states are

identified during the initial dissolution process. The first transition state involves breaking of I−Pb bond and formation of an intermediate state (I−MA interactions) at the surface with a low energy barrier of 0.16 eV. The second transition state corresponds to dissociation I−MA interaction and hydration of the $I^-$ ion with the energy barrier of 0.22 eV. In addition, using DFT calculations augmented with experimental data, the analysis of the thermodynamics of $MAPbI_3$ decomposition in water at a finite concentration indicates a negative Gibbs free energy change which suggests the spontaneity of water dissolution of $MAPbI_3$. It is worth mentioning that a large hydration enthalpy of $MA^+$ and an entropy gain under aqueous condition direct the negative $\Delta G_{\text{diss}}$. Combined with the low energy barrier for ease of ions escaping from the $MAPbI_3$ surface and spontaneous nature of dissolving in water, it can be explained why the water immediately destroys pristine $MAPbI_3$. We also analyze how $CsPbI_3$ reacts with water from the thermodynamic point of view. It is found that the Gibbs free energy change of dissolution $CsPbI_3$ in water is also a negative value similar to the value of $MAPbI_3$, which is consistent with experimental observation of $CsPbI_3$ degradation in a moist environment. Compared with $MAPbI_3$, a large entropy enhancement of $Cs^+$ dominates the negative $\Delta G_{\text{diss}}$ for $CsPbI_3$ dissolution in water. Our explanation provides a deeper insight into the water instability of $MAPbI_3$ and presents a perspective on improving the instability of perovskite photovoltaics in the future.

# Bibliography

[1] Best research-cell efficiency chart. `https://www.nrel.gov/pv/cell-efficiency.html`. Accessed: 2019-10-01.

[2] N. Aristidou, C. Eames, M. S. Islam, and S. A. Haque. Insights into the increased degradation rate of $CH_3NH_3PbI_3$ solar cells in combined water and $O_2$ environments. *J. Mater. Chem. A*, 5(48):25469–25475, 2017. doi: 10.1039/c7ta06841g.

[3] A. M. Askar, G. M. Bernard, B. Wiltshire, K. Shankar, and V. K. Michaelis. Multinuclear magnetic resonance tracking of hydro, thermal, and hydrothermal decomposition of $CH_3NH_3PbI_3$. *J. Phys. Chem. C*, 121(2):1013–1024, 2017. doi: 10.1021/acs.jpcc.6b10865.

[4] L. S. Belvèze, J. F. Brennecke, and M. A. Stadtherr. Modeling of activity coefficients of aqueous solutions of quaternary ammonium salts with the electrolyte-NRTL equation. *Ind. Eng. Chem. Res*, 43(3):815–825, 2004. doi: 10.1021/ie0340701.

[5] P. Blöchl. Projector augmented-wave method. *Phys. Rev. B*, 50(24):17953, 1994.

[6] O. D. Bonner. Osmotic and activity coefficients of methyl-substituted ammonium chlorides. *J. Chem. Soc. Faraday Trans.*, 77(10):2515–2518, 1981. doi: 10.1039/F19817702515.

[7] M. Bonomi, D. Branduardi, G. Bussi, C. Camilloni, D. Provasi, P. Raiteri, D. Donadio, F. Marinelli, F. Pietrucci, and R. A. Broglia. Plumed: A portable plugin for free-energy calculations with molecular dynamics. *Comput. Phys. Commun.*, 180(10):1961–1972, 2009. doi: 10.1016/j.cpc.2009.05.011.

[8] T. Bucko. *Ab Initio* calculations of free-energy reaction barriers. *J. Phys.: Condens. Matter*, 20(6):064211, 2008. doi: 10.1088/0953-8984/20/6/064211.

[9] C. Caddeo, M. I. Saba, S. Meloni, A. Filippetti, and A. Mattoni. Collective molecular mechanisms in the $CH_3NH_3PbI_3$ dissolution by liquid water. *ACS nano*, 11(9):9183–9190, 2017.

[10] C. Caddeo, D. Marongiu, S. Meloni, A. Filippetti, F. Quochi, M. Saba, and A. Mattoni. Hydrophilicity and water contact angle on methylammonium lead iodide. *Adv. Mater. Interfaces*, page 1801173, Dec. 2018. doi: 10.1002/admi.201801173.

[11] J.-C. Chen, B. Reischl, P. Spijker, N. Holmberg, K. Laasonen, and A. S. Foster. *Ab Initio* kinetic monte carlo simulations of dissolution at the NaCl-water interface. *Phys. Chem. Chem. Phys.*, 16:22545–22554, 2014. doi: 10.1039/C4CP02375G.

[12] P. Delugas, A. Filippetti, and A. Mattoni. Methylammonium fragmentation in amines as source of localized trap levels and the healing role of Cl in hybrid lead-iodide perovskites. *Phys. Rev. B*, 92:045301, Jul 2015. doi: 10.1103/PhysRevB.92.045301.

[13] B. Ensing, A. Laio, M. Parrinello, and M. L. Klein. A recipe for the computation of the free energy barrier and the lowest free energy path of concerted reactions. *J. Phys. Chem. B*, 109(14):6676–6687, 2005. doi: 10.1021/jp045571i.

[14] Z. Fan, H. Xiao, Y. Wang, Z. Zhao, Z. Lin, H.-C. Cheng, S.-J. Lee, G. Wang, Z. Feng, and W. A. Goddard III. Layer-by-layer degradation of methylammonium lead tri-iodide perovskite microplates. *Joule*, 1(3):548–562, 2017.

[15] M. Fedotova and S. Kruchinin. Hydration of methylamine and methylammonium ion: Structural and thermodynamic properties from the data of the integral equation method in the rism approximation. *Russ. Chem. Bull.*, 61(2):240–247, 2012. doi: 10.1007/s11172-012-0034-5.

[16] J. M. Frost, K. T. Butler, F. Brivio, C. H. Hendon, M. Van Schilfgaarde, and A. Walsh.

Atomistic origins of high-performance in hybrid halide perovskite solar cells. *Nano Lett.*, 14(5):2584–2590, 2014. doi: 10.1021/nl500390f.

[17] S. Grimme, J. Antony, S. Ehrlich, and H. Krieg. A consistent and accurate *Ab Initio* parametrization of density functional dispersion correction (DFT-D) for the 94 elements h-pu. *J. Chem. Phys.*, 132(15):154104, 2010. doi: 10.1063/1.3382344.

[18] B. Hailegnaw, S. Kirmayer, E. Edri, G. Hodes, and D. Cahen. Rain on methylammonium lead iodide based perovskites: Possible environmental effects of perovskite solar cells. *J. Phys. Chem. Lett.*, 6(9):1543–1547, 2015.

[19] G. Hautier, S. P. Ong, A. Jain, C. J. Moore, and G. Ceder. Accuracy of density functional theory in predicting formation energies of ternary oxides from binary oxides and its implication on phase stability. *Phys. Rev. B*, 85:155208, Apr 2012. doi: 10.1103/PhysRevB.85.155208.

[20] Y. Hinuma, G. Pizzi, Y. Kumagai, F. Oba, and I. Tanaka. Band structure diagram paths based on crystallography. *Comput. Mater. Sci.*, 128:140–184, 2017.

[21] W. G. Hoover. Canonical dynamics: Equilibrium phase-space distributions. *Phys. Rev. A*, 31(3):1695, 1985.

[22] C. E. Housecroft and H. D. B. Jenkins. Absolute ion hydration enthalpies and the role of volume within hydration thermodynamics. *RSC Adv.*, 7(45):27881–27894, 2017.

[23] M. Iannuzzi, A. Laio, and M. Parrinello. Efficient exploration of reactive potential energy surfaces using car-parrinello molecular dynamics. *Phys. Rev. Lett.*, 90:238302, Jun 2003. doi: 10.1103/PhysRevLett.90.238302.

[24] A. Kakekhani, R. N. Katti, and A. M. Rappe. Water in hybrid perovskites: Bulk $MAPbI_3$ degradation *via* super-hydrous state. *APL Mater.*, 7(4):041112, 2019.

[25] A. Karmakar and A. Chandra. Water in hydration shell of an iodide ion: Structure and dynamics of solute-water hydrogen bonds and vibrational spectral diffusion from first-principles simulations. *J. Phys. Chem. C*, 119(27):8561–8572, 2015.

[26] J. C.-R. Ke, A. S. Walton, D. J. Lewis, A. Tedstone, P. O'Brien, A. G. Thomas, and W. R. Flavell. *In situ* investigation of degradation at organometal halide perovskite surfaces by x-ray photoelectron spectroscopy at realistic water vapour pressure. *Chem. Commun.*, 53(37):5231–5234, 2017. doi: 10.1039/C7CC01538K.

[27] J. Klimeš, D. R. Bowler, and A. Michaelides. Chemical accuracy for the van der waals density functional. *J Phys. Condens. Matter*, 22(2):022201, 2009. doi: 10.1088/0953-8984/22/2/022201.

[28] W. Kohn and L. J. Sham. Self-consistent equations including exchange and correlation effects. *Phys. Rev.*, 140(4A):A1133, 1965. doi: 10.1103/PhysRev.140.A1133.

[29] A. Kojima, K. Teshima, Y. Shirai, and T. Miyasaka. Organometal halide perovskites as visible-light sensitizers for photovoltaic cells. *J. Am. Chem. Soc.*, 131(17):6050–6051, 2009. doi: 10.1021/ja809598r.

[30] F. U. Kosasih and C. Ducati. Characterising degradation of perovskite solar cells through *In-Situ* and operando electron microscopy. *Nano Energy*, 47:243–256, May 2018. doi: 10.1016/j.nanoen.2018.02.055.

[31] G. Kresse and J. Furthmüller. Efficient iterative schemes for *Ab Initio* total-energy calculations using a plane-wave basis set. *Phys. Rev. B*, 54(16):11169, 1996.

[32] G. Kresse and D. Joubert. From ultrasoft pseudopotentials to the projector augmented-wave method. *Phys. Rev. B*, 59(3):1758, 1999.

[33] Y.-H. Kye, C.-J. Yu, U.-G. Jong, K.-C. Ri, J.-S. Kim, S.-H. Choe, S.-N. Hong, S. Li,

J. N. Wilson, and A. Walsh. Vacancy-driven stabilization of the cubic perovskite polymorph of $CsPbI_3$. *J. Phys. Chem. C*, 123(15):9735–9744, 2019.

[34] A. Laio and M. Parrinello. Escaping free-energy minima. *Proc. Natl. Acad. Sci. U.S.A.*, 99(20):12562–12566, 2002. doi: 10.1073/pnas.202427399.

[35] Y. Li and K. Yang. High-throughput computational design of organic-inorganic hybrid halide semiconductors beyond perovskites for optoelectronics. *Energy Environ. Sci.*, 12:2233–2243, 2019. doi: 10.1039/C9EE01371G.

[36] Y. Li, X. Xu, C. Wang, C. Wang, F. Xie, J. Yang, and Y. Gao. Degradation by exposure of coevaporated $CH_3NH_3PbI_3$ thin films. *J. Phys. Chem. C*, 119(42):23996–24002, 2015. doi: 10.1021/acs.jpcc.5b07676.

[37] C.-C. Lin, Y. Lyu, D. L. Hunston, J. H. Kim, K.-T. Wan, D. L. Stanley, and X. Gu. Cracking and delamination behaviors of photovoltaic backsheet after accelerated laboratory weathering. In *Reliability of Photovoltaic Cells, Modules, Components, and Systems VIII*, volume 9563, page 956304. International Society for Optics and Photonics, 2015.

[38] J. Lin, M. Lai, L. Dou, C. S. Kley, H. Chen, F. Peng, J. Sun, D. Lu, S. A. Hawks, and C. Xie. Thermochromic halide perovskite solar cells. *Nat. Mater.*, 17(3):261–267, 2018. doi: 10.1038/s41563-017-0006-0.

[39] L.-M. Liu, A. Laio, and A. Michaelides. Initial stages of salt crystal dissolution determined with *Ab Initio* molecular dynamics. *Phys. Chem. Chem. Phys.*, 13(29):13162–13166, 2011. doi: 10.1039/C1CP21077G.

[40] Y. Marcus and A. Loewenschuss. Chapter 4. standard entropies of hydration of ions. *Annu. Rep. Prog. Chem., Sect. C: Phys. Chem.*, 81:81–135, 1984. doi: 10.1039/PC9848100081.

[41] G. Markovich, R. Giniger, M. Levin, and O. Cheshnovsky. Photoelectron spectroscopy of iodine anion solvated in water clusters. *J. Chem. Phys.*, 95(12):9416–9419, 1991. doi: 10.1063/1.461172.

[42] A. Marronnier, G. Roma, S. Boyer-Richard, L. Pedesseau, J.-M. Jancu, Y. Bonnassieux, C. Katan, C. C. Stoumpos, M. G. Kanatzidis, and J. Even. Anharmonicity and disorder in the black phases of caesium lead iodide used for stable inorganic perovskite solar cells. *ACS nano*, 12(4):3477–3486, 2018. doi: 10.1021/acsnano.8b00267.

[43] J. A. McLeod and L. Liu. Prospects for mitigating intrinsic organic decomposition in methylammonium lead triiodide perovskite. *J. Phys. Chem. Lett.*, 9(9):2411–2417, Apr. 2018. doi: 10.1021/acs.jpclett.8b00323.

[44] K. Momma and F. Izumi. Vesta 3 for three-dimensional visualization of crystal, volumetric and morphology data. *J. Appl. Crystallogr.*, 44(6):1272–1276, 2011. doi: 10.1107/S0021889811038970.

[45] H. J. Monkhorst and J. D. Pack. Special points for brillouin-zone integrations. *Phys. Rev. B*, 13:5188–5192, Jun 1976. doi: 10.1103/PhysRevB.13.5188.

[46] E. Mosconi, J. M. Azpiroz, and F. De Angelis. *Ab Initio* molecular dynamics simulations of methylammonium lead iodide perovskite degradation by water. *Chem. Mater.*, 27(13):4885–4892, 2015. doi: 10.1021/acs.chemmater.5b01991.

[47] G. Niu, W. Li, F. Meng, L. Wang, H. Dong, and Y. Qiu. Study on the stability of $CH_3NH_3PbI_3$ films and the effect of post-modification by aluminum oxide in all-solid-state hybrid solar cells. *J. Mater. Chem. A*, 2(3):705–710, 2014. doi: 10.1039/C3TA13606J.

[48] S. Nosé. A unified formulation of the constant temperature molecular dynamics methods. *J. Chem. Phys.*, 81(1):511–519, 1984. doi: 10.1063/1.447334.

[49] R. Ohmann, L. K. Ono, H.-S. Kim, H. Lin, M. V. Lee, Y. Li, N.-G. Park, and Y. Qi. Real-space imaging of the atomic structure of organic–inorganic perovskite. *J. Am. Chem. Soc.*, 137(51):16049–16054, 2015. doi: 10.1021/jacs.5b08227.

[50] H. Ohtaki, N. Fukushima, E. Hayakawa, and I. Okada. Dissolution process of sodium chloride crystal in water. *Pure Appl. Chem.*, 60(8):1321–1324, 1988.

[51] S. P. Ong, S. Cholia, A. Jain, M. Brafman, D. Gunter, G. Ceder, and K. A. Persson. The materials application programming interface (API): a simple, flexible and efficient API for materials data based on representational state transfer (rest) principles. *Comput. Mater. Sci.*, 97:209–215, 2015. doi: 10.1016/j.commatsci.2014.10.037.

[52] N. Onoda-Yamamuro, T. Matsuo, and H. Suga. Calorimetric and IR spectroscopic studies of phase transitions in methylammonium trihalogenoplumbates (ii). *J. Phys. Chem. Solids*, 51(12):1383–1395, 1990.

[53] S. Park, W. J. Chang, C. W. Lee, S. Park, H.-Y. Ahn, and K. T. Nam. Photocatalytic hydrogen generation from hydriodic acid using methylammonium lead iodide in dynamic equilibrium with aqueous solution. *Nat. Energy*, 2(1):16185, 2017. doi: 10.1038/nenergy.2016.185.

[54] J. P. Perdew, K. Burke, and M. Ernzerhof. Generalized gradient approximation made simple. *Phys. Rev. Lett.*, 77:3865, 1996. doi: 10.1103/PhysRevLett.77.3865.

[55] B. Philippe, B.-W. Park, R. Lindblad, J. Oscarsson, S. Ahmadi, E. M. Johansson, and H. Rensmo. Chemical and electronic structure characterization of lead halide perovskites and stability behavior under different exposures a photoelectron spectroscopy investigation. *Chem. Mater.*, 27(5):1720–1731, 2015. doi: 10.1021/acs.chemmater.5b00348.

[56] J. Rumble. *CRC Handbook of Chemistry and Physics*. CRC press, Boca Raton, Florida, 2017.

[57] M. I. Saidaminov, J. Kim, A. Jain, R. Quintero-Bermudez, H. Tan, G. Long, F. Tan, A. Johnston, Y. Zhao, O. Voznyy, and E. H. Sargent. Suppression of atomic vacancies via incorporation of isovalent small ions to increase the stability of halide perovskite solar cells in ambient air. *Nat. Energy*, 3(8):648–654, July 2018. doi: 10.1038/s41560-018-0192-2.

[58] L. She, M. Liu, and D. Zhong. Atomic structures of $CH_3NH_3PbI_3$ (001) surfaces. *ACS Nano*, 10(1):1126–1131, 2015.

[59] D. Sholl and J. A. Steckel. *Density Functional Theory: a Practical Introduction*. John Wiley & Sons, Hoboken, New Jersey, 2011.

[60] E. Smecca, Y. Numata, I. Deretzis, G. Pellegrino, S. Boninelli, T. Miyasaka, A. L. Magna, and A. Alberti. Stability of solution-processed $MAPbI_3$ and $FAPbI_3$ layers. *Phys. Chem. Chem. Phys.*, 18(19):13413–13422, 2016. doi: 10.1039/c6cp00721j.

[61] D. W. Smith. Ionic hydration enthalpies. *J. Chem. Educ.*, 54(9):540–542, 1977. doi: 10.1021/ed054p540.

[62] E. Tenuta, C. Zheng, and O. Rubel. Thermodynamic origin of instability in hybrid halide perovskites. *Sci. Rep.*, 6:37654, 2016. doi: 10.1038/srep37654.

[63] Y. Wang, T. Gould, J. F. Dobson, H. Zhang, H. Yang, X. Yao, and H. Zhao. Density functional theory analysis of structural and electronic properties of orthorhombic perovskite $CH_3NH_3PbI_3$. *Phys. Chem. Chem. Phys.*, 16(4):1424–1429, 2013. doi: 10.1039/C3CP54479F.

[64] W. Wei and Y. H. Hu. Catalytic role of $H_2O$ in degradation of inorganic-organic

perovskite ($CH_3NH_3PbI_3$) in air. *Int. J. Energy Res.*, 41(7):1063–1069, Nov. 2016. doi: 10.1002/er.3680.

[65] P. Whitfield, N. Herron, W. Guise, K. Page, Y. Cheng, I. Milas, and M. Crawford. Structures, phase transitions and tricritical behavior of the hybrid perovskite methyl ammonium lead iodide. *Sci. Rep.*, 6:35685, 2016. doi: 10.1038/srep35685.

[66] O. Yamamuro, M. Oguni, T. Matsuo, and H. Suga. Calorimetric and dilatometric studies on the phase transitions of crystalline $CH_3NH_3I$. *J. Chem. Thermodyn.*, 18 (10):939–954, 1986.

[67] J. Yang, Z. Yuan, X. Liu, S. Braun, Y. Li, J. Tang, F. Gao, C. Duan, M. Fahlman, and Q. Bao. Oxygen- and water-induced energetics degradation in organometal halide perovskites. *ACS Appl. Mater. Interfaces*, 10(18):16225–16230, Apr. 2018. doi: 10.1021/acsami.8b04182.

[68] Y. Yang, S. Meng, L. F. Xu, E. G. Wang, and S. Gao. Dissolution dynamics of NaCl nanocrystal in liquid water. *Phys. Rev. E*, 72:012602, Jul 2005. doi: 10.1103/PhysRevE.72.012602.

[69] G. Yuan, C. Ritchie, M. Ritter, S. Murphy, D. E. Gómez, and P. Mulvaney. The degradation and blinking of single $CsPbI_3$ perovskite quantum dots. *J. Phys. Chem. C*, 122(25):13407–13415, 2017. doi: 10.1021/acs.jpcc.7b11168.

[70] Y. Zhang, S. Chen, P. Xu, H. Xiang, X. Gong, A. Walsh, and S. Wei. Intrinsic instability of the hybrid halide perovskite semiconductor $CH_3NH_3PbI_3$. *Chin. Phys. Lett.*, 35(3): 036104, 2018. doi: 10.1088/0256-307X/35/3/036104.

[71] C. Zheng and O. Rubel. Ionization energy as a stability criterion for halide perovskites. *J. Phys. Chem. C*, 121(22):11977–11984, 2017. doi: 10.1021/acs.jpcc.7b00333.

[72] C. Zheng and O. Rubel. Aziridinium lead iodide: A stable, low-band-gap hybrid halide perovskite for photovoltaics. *J. Phys. Chem. Lett.*, 9(4):874–880, 2018. doi: 10.1021/acs.jpclett.7b03114.

[73] C. Zheng, S. Yu, and O. Rubel. Structural dynamics in hybrid halide perovskites: Bulk rashba splitting, spin texture, and carrier localization. *Phys. Rev. Materials*, 2 (11):114604, 2018.

[74] T. Zhu and E. Ertekin. Mixed phononic and non-phononic transport in hybrid lead halide perovskites: Glass-crystal duality, dynamical disorder, and anharmonicity. *Energy Environ. Sci.*, 12(1):216–229, 2019. doi: 10.1039/C8EE02820F.

# Chapter 8

# Conclusion

It is the long-term instability of hybrid halide perovskites that hinders the next development of large-scale fabrication. The main project in this thesis is to investigate the instability which is explored by using the first principles method.

At the beginning of this thesis, the characterization of this instability of $CH_3NH_3PbI_3$ is performed by estimating the reaction enthalpy between the reactants and the product. It is found that $CH_3NH_3PbI_3$ possesses a near-zero reaction enthalpy $\Delta H^\circ_{0\ \mathrm{K}} = 0.05$ eV which renders a margin condition at the stability. By combination calculated data with thermodynamic data, we found that finite temperature effect tends to stabilize $CH_3NH_3PbI_3$ $\Delta G^\circ_{300\ \mathrm{K}} = 0.16$ eV. However, this Gibbs free energy change of reactants and products are still close to zero. It means the stability will be easily perturbed by external stimuli.

By characterization of the intrinsic instability of hybrid halide perovskites, the extension of Born–Haber cycle to the hybrid halide perovskites was achieved to decompose the reaction enthalpy. Analysis of Born–Haber cycle of $CH_3NH_3PbI_3$, we pinpointed the ionization energy of A site cation affecting this reaction enthalpy. Hence, a criterion was proposed to screen cations for alternative perovskite absorber for photovoltaics.

Encouraged from a four-membered ring cation as a precursor for synthesizing perovskite structure, we theoretically proposed a hybrid halide perovskite structure with three-membered ring cation centring the structure. A more favorable reaction enthalpy $\sim 0.15$ eV lower than the value of $CH_3NH_3PbI_3$ (the lower the more stable). The size of this three-membered ring is slightly smaller than $CH_3NH_3{}^+$. These parameters suggested better formability for an alternative perovskite absorber. And this three-membered ring based structure rendered a very promising bandgap 1.5 eV. However, we noticed an instability of the three-membered ring cation itself. Halide ions and water molecules will open the ring. Further investigation of the instability, we found that ring-opened cation in the $Pb-I$ framework has a lower total energy $\Delta E = 0.7$ eV compared with $AZRPbI_3$. Besides, the water invasion of $AZRPbI_3$ will further lower the energy of corresponding products which is 1.6 eV lower than the total energy of $AZRPbI_3$. The nucleophilicity of water, high ring strain of aziridinium and low lattice energy of hybrid halide perovskite are responsible for this hydrolysis reaction.

Degradation mechanism of $CH_3NH_3PbI_3$ in liquid water is also very important when cracks appear on the encapsulation layer. We used metadynamics to estimate the energy barrier of the initial dissolution of $CH_3NH_3PbI_3$ in water. A very low energy barrier 0.18 eV suggested a fast and ease initial degradation process. Furthermore, we analyzed Gibbs free energy change considering dissolution in water. Both $CH_3NH_3PbI_3$ and $CsPbI_3$ had around $-0.3$ eV Gibbs free energy change which indicated both the perovskite had a trend of dissolution in liquid water. Intriguingly, it was found a large hydration enthalpy of $CH_3NH_3{}^+$ and an entropy gain was responsible for the degradation of $CH_3NH_3PbI_3$ in water. And a large entropy enhancement of $Cs^+$ dominates the Gibbs free energy change leading the degradation of $CsPbI_3$ in water.

# Appendix A

# Supporting materials

## Supporting Information

# Unraveling the Water Degradation Mechanism of $CH_3NH_3PbI_3$

Chao Zheng* and Oleg Rubel *

*Department of Materials Science and Engineering, McMaster University,*

*1280 Main Street West, Hamilton, Ontario L8S 4L8, Canada*

The free energy surface of $MA^+$ dissolution in water is plotted in FIG. S1. This free energy surface is only for initial basin. It is obtained via ~4.7 ps metadynamics with a Gaussian height of 0.026 and a Gaussian weight of 0.014 and a continuous ~4.6 ps metadynamic calculation with a Gaussian height of 0.052 and a Gaussian weight of 0.018. We found the case of $MA^+$ calculation took much longer time staying at the initial basin. Due to the capability of our facility and limited time, we stopped for exploring the sequent free energy surface of $MA^+$ dissolution in water.

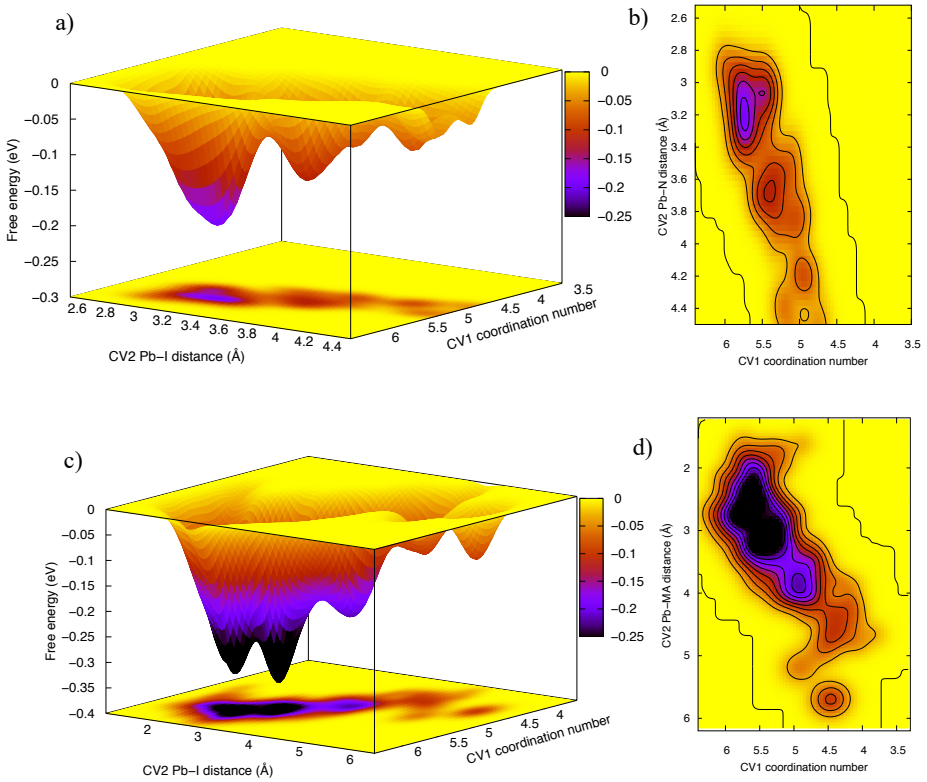


FIG. S1. (a) Free energy surface of initial basin of $I^-$ dissolution in water. (b) Contour of the free energy surface of $I^-$ dissolution in water. (c) Free energy surface of initial basin of $MA^+$ dissolution in water. (d) Contour of the free energy surface of $MA^+$ dissolution in water.

Comparing FIG. S1(a) and FIG. S1(c), we found the initial basin of $MA^+$ dissolution in water is deeper (~0.15 eV lower) than the value of $I^-$ dissolution in water. And from FIG. S1(b) and FIG. S1(d), we found the initial basin of $MA^+$ dissolution in water is wider than the case of $I^-$ dissolution in water. Hence, it explains the slow exploring rate and the inferiority of $MA^+$ dissolution in water for metadynamics.

# Appendix B

# Supporting materials

PHYSICAL REVIEW MATERIALS **2**, 114604 (2018)

# Structural dynamics in hybrid halide perovskites: Bulk Rashba splitting, spin texture, and carrier localization

Chao Zheng,[1] Shidong Yu,[1,2] and Oleg Rubel[1,*]

[1]*Department of Materials Science and Engineering, McMaster University, 1280 Main Street West, Hamilton, Ontario L8S 4L8, Canada*

[2]*College of Materials Science and Engineering, Jilin University, 2699 Qianjin Street, Changchun City 130012, China*

(Received 30 September 2018; published 28 November 2018)

The extended charge carrier lifetime in hybrid halide perovskites was attributed to a quasi-indirect band gap that arises due to a Rashba splitting in both conduction and valence band edges. In this paper, we present results for an effective relativistic band structure of $(CH_3NH_3)PbI_3$ with the focus on the dispersion of electronic states near the band edges of $(CH_3NH_3)PbI_3$ affected by thermal structural fluctuations. We establish a relationship between the magnitude of the Rashba splitting and a deviation of the Pb atom from its centrosymmetric site position in the $PbI_6$ octahedron. For the splitting energy to reach the thermal energy $k_BT \approx 26$ meV (room temperature), the displacement should be on the order of 0.3 Å, which is far above the static displacements of Pb atoms in the tetragonal phase of $(CH_3NH_3)PbI_3$. The significant dynamic enhancement of the Rashba splitting observed at earlier simulation times (less than 2 ps) later weakens and becomes less than the thermal energy despite the average displacement of Pb atoms remaining large (0.37 Å). A randomization of Pb-displacement vectors and associated cancellation of the net effective magnetic field acting on electrons at the conduction band edge is responsible for reduction of the Rashba splitting. The lattice dynamics also leads to deterioration of a Bloch character for states in the valence band leading to the subsequent localization of holes, which affects the bipolar mobility of charge carriers in $(CH_3NH_3)PbI_3$. These results call into question the quasi-indirect band gap as a reason for the long carrier lifetime observed in $(CH_3NH_3)PbI_3$ at room temperature. Analysis of spin projections and the spin overlap at the band edges also rules out the spin helicity as a possible cause for a long lifetime of optical excitations in perovskite structures. An alternative mechanism involves dynamic localization of holes and their reduced overlap with electrons in reciprocal space.

DOI: 10.1103/PhysRevMaterials.2.114604

## I. INTRODUCTION

Hybrid halide perovskites, with $(CH_3NH_3)PbI_3$ being a prominent member, have attracted enormous interest as a solar cell absorber material [1–5]. One unique property of this class of materials is that they combine benefits of direct and indirect semiconductors featuring both a long carrier lifetime in excess of 100 ns [6–9] and a sharp absorption edge [10]. These features are attributed to the presence of Rashba splitting, which occurs at the valence and conduction band edges of hybrid halide perovskites [11–13].

The physics of the Dresselhaus-Rashba effect [14,15] is linked to the spin-orbit coupling (SOC) due to an interaction between electron spin and an apparent magnetic field that arises from the electron moving in an electric field. Not all electronic states are directly susceptible to SOC. The coupling affects states that experience a net apparent magnetic field remaining after averaging over possible electron trajectories. In atoms, this leads to splitting of energy levels for states with the orbital angular momentum quantum number $\ell > 0$. In solids, electron orbitals experience an additional crystal field. If the crystal field lacks a central symmetry, Kramers' spin degeneracy is lifted leading to spin splitting and occurrence of an unusual band dispersion illustrated in Fig. 1(a). The Dresselhaus-Rashba effect is actively studied in spintronics (spin currents and the spin Hall effect) and topological insulators [16].

The extended carrier lifetime in hybrid halide perovskites was attributed to a quasi-indirect band gap that arises due to Rashba splitting in both conduction and valence band edges [17–19] as shown in Fig. 1(b). For this argument to stand, the magnitude of Rashba splitting must significantly exceed the solar cell operating temperature ($E_R > k_BT$) to prevent the finite-temperature population statistics from enabling direct optical transitions [Fig. 1(b)]. Niesner *et al.* [20] measured the valence band dispersion in $(CH_3NH_3)PbI_3$ using an angle-resolved photoelectron spectroscopy and found a rather large magnitude of Rashba splitting of $E_R = 0.16$ and 0.24 eV in orthorhombic (low temperature) and cubic (high temperature) phases, respectively, indicating that the splitting is enhanced by the lattice dynamics. Recent photogalvanic measurements [21] provide more moderate values of the combined (valence and conduction band) Rashba splitting of $E_R \sim 0.1$ eV that steadily increases with temperature.

Typically, the band structure of perovskites is calculated using a primitive unit cell (either pseudocubic, tetragonal, or orthorhombic structures), where atoms are relaxed to their lowest energy positions [22,23]. However, experimental studies of hybrid halide perovskites [24,25] clearly indicate a substantial dynamic disorder of atomic positions at room

*rubelo@mcmaster.ca

 

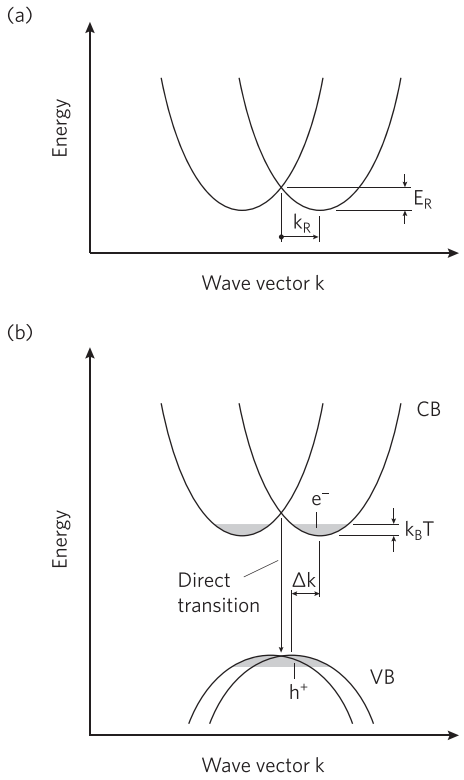


FIG. 1. (a) Schematic Dresselhaus-Rashba splitting with $E_R$ showing the magnitude of splitting. (b) Although the band gap is indirect ($\Delta k$), the final temperature carrier statistic allows for direct transitions if $E_R < k_BT$.

temperature, which should influence the electronic structure of these materials. For the aforementioned mechanism to operate, the lattice dynamics should produce a steady enhancement of the Rashba splitting and, *at the same time*, preserve the Bloch character (wave vector $k$) for electronic states at the band edges. Theoretical studies of dynamic effects on the Rashba splitting started only recently [26–30], and details on how the dispersion of electronic states near the band edges of $(CH_3NH_3)PbI_3$ is affected by thermal structural fluctuations are still missing.

In this paper, we calculate an effective relativistic band structure of $(CH_3NH_3)PbI_3$ taking the thermal disorder of atomic positions into account. The disorder is explicitly modeled via *ab initio* molecular dynamics (MD) simulation performed for a large supercell. The supercell band structure is later unfolded to a primitive (pseudocubic) Brillouin zone that allows its direct comparison with experimental data. In addition, we explore a possible spatial localization of electronic states at the band edges caused by dynamical structural fluctuations. Robustness of electronic states at the band edges is an important functional requirement for photovoltaic applications.

## II. COMPUTATIONAL DETAILS

The Vienna *Ab initio* Simulation Package (VASP) [31,32] density functional theory [33] (DFT) package was employed in this work. A Perdew, Burke, and Ernzerhof [34] (PBE) gradient approximation for the exchange-correlation functional was used in combination with the Grimme *et al.* [35] (D3) correction to capture long-range van der Waals interactions.

The original structure of tetragonal $(CH_3NH_3)PbI_3$ was taken from Stoumpos *et al.* [36] (database code ICSD 250739) with the following structural parameters: space group 108 ($I4cm$), $a = b = 8.849$ Å, $c = 12.642$ Å, fractional coordinates $u_{Pb} = (0, 0, 0)$, $u_{I1} = (0, 0, 0.24720)$, $u_{I2} = (0.21417, 0.71417, 0.00460)$. Once the $PbI_3$ cage was set, methylammonium cations were added, and the structure was relaxed while maintaining symmetry of the $PbI_3$ cage. Calculations were carried out using a $3 \times 3 \times 2$ Monkhorst and Pack [37] $k$ mesh for the primitive Brillouin zone of a tetragonal phase. The structural relaxation was performed by minimizing Hellmann-Feynman forces and stresses below 20 meV/Å and 0.5 kbar, respectively. The cutoff energy for the plane-wave expansion was set at 400 eV. Relativistic effects (SOC) were omitted from the structure optimization but included later in band structure calculations. The resultant optimized structure had lattice parameters of $a = b = 8.661$ Å and $c = 12.766$ Å and can be accessed at the Cambridge Crystallographic Data Center (CCDC) under deposition No. 1870783.

Next we describe a semiempirical scaling of the lattice parameters to achieve a finite-temperature structure of $(CH_3NH_3)PbI_3$ that is self-consistent with the PBE+D3 functional. The volume of the calculated tetragonal unit cell at 0 K yields a pseudocubic lattice parameter of $a_c(0\ \mathrm{K}) = 6.209$ Å. Changes in the pseudocubic lattice parameter with temperature can be expressed as

$$a_c(T) = a_c(0\ \mathrm{K})(1 + \alpha_a T) \tag{1}$$

with the linear expansion coefficient of $\alpha_a = 4.21 \times 10^{-5}\ \mathrm{K}^{-1}$ inferred from the experimental data [24] in the range of temperatures 150–350 K [see Fig. 6(c) therein]. Evolution of the pseudocubic lattice parameter with temperature is shown in Fig. 2(a).

Tetragonality of the structure can be expressed as

$$t = 1 - a_t/c_t, \tag{2}$$

where $a_t = b_t$ and $c_t$ are tetragonally distorted lattice parameters that are related to conventional lattice parameters of the tetragonal structure via $a = a_t\sqrt{2}$ and $c = 2c_t$. At 0 K the tetragonality is $t(0\ \mathrm{K}) = 0.04058$ as obtained from our DFT calculations. The tetragonality is significantly reduced with increasing temperature and amounts to $t(293\ \mathrm{K}) = 0.01$ [36]. The temperature-dependent tetragonality can be captured by a scaling function [24]

$$t(T) = t(0)(1 - T/T_c)^{2\beta} \tag{3}$$

with critical parameters $T_c = 333$ K and $\beta = 0.27$ taken from [24] [see Fig. 8(b) therein]. The temperature-dependent tetragonality parameter is shown in Fig. 2(b). The temperature-dependent tetragonally distorted lattice parameters $a_t(T)$ and $c_t(T)$ [Fig. 2(a)] were obtained by combining

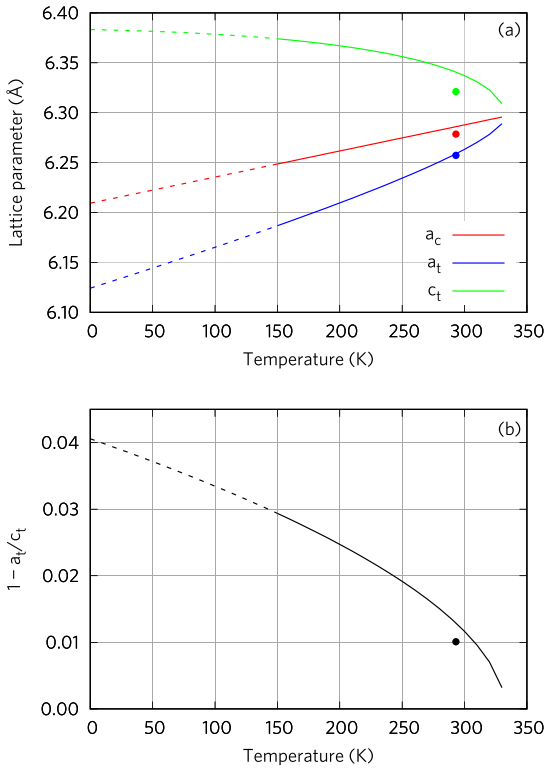


FIG. 2. Finite-temperature scaling of $(CH_3NH_3)PbI_3$ (a) lattice parameters and (b) tetragonality starting with DFT-PBE+D3 results for 0 K. Data are shown for $T < 150$ K even though the tetragonal structure is unstable in this temperature range. Experimental data [36] are shown with points.

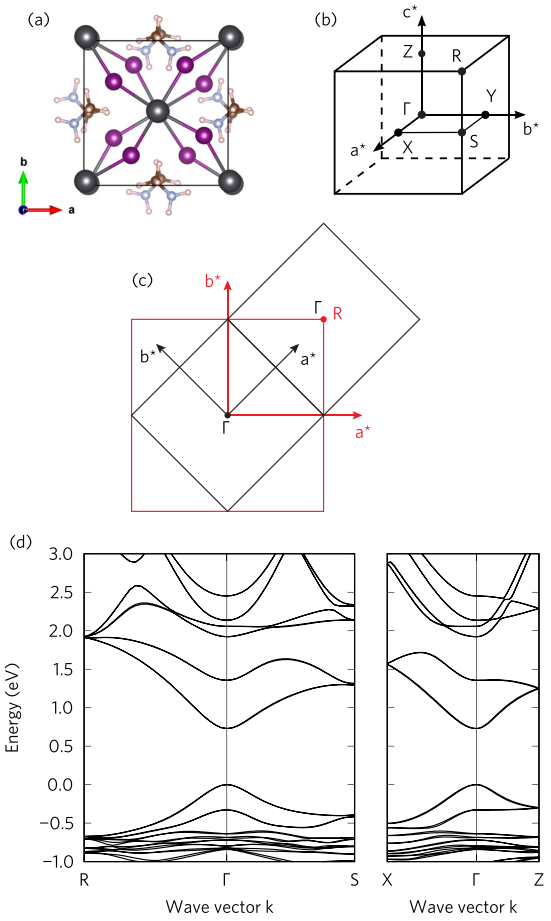


FIG. 3. (a) Tetragonal unit cell, (b) Brillouin zone, (c) folding of the $R$ point into Γ when the structure is transformed from a pseudocubic (red) to a tetragonal (black) cell, and (d) relativistic band structure of tetragonal $(CH_3NH_3)PbI_3$ with lattice parameters scaled to 300 K and the symmetrized $PbI_3$ cage. No sizable Rashba splitting is observed although the structure is noncentrosymmetric. The origin of the energy scale is set at the Fermi energy.

the $t(T)$ and $a_c(T)$ dependencies assuming an equal volume for both cubic and tetragonal structures ($a_c^3 = c_t a_t^2$) at a given temperature.

This approach yields finite-temperature tetragonal lattice parameters of $a = b = 8.858$ Å and $c = 12.674$ Å at 300 K that are self-consistent with PBE+D3. Atomic positions of this structure were further relaxed while maintaining symmetry of the $PbI_3$ cage. The corresponding structure file can be accessed at CCDC under deposition No. 1870784.

The MD simulation was performed in two stages: first preheating and then a "production" run. The initial structure was a $4 \times 4 \times 4$ supercell [Fig. 9(a)] with lattice parameters scaled to 300 K as described above. The symmetry (except for the translational one) was turned off during the simulation (VASP tag ISYM = 0). Preheating from 0 to 300 K was performed in 500 steps (step size of 1 fs) using a linear ramp-up function (VASP tag SMASS = −1). Velocities were scaled every 10 MD steps. Accuracy of computed Hellmann-Feynman forces was determined by the energy convergence criterion of $10^{-7}$ eV. Only one $k$ point at Γ was used to sample the Brillouin zone. Atomic positions and velocities at the end of the preheating stage were taken as input for the production run. The production run took 2200 steps (step size of 1 fs) of a constant energy MD (VASP tag SMASS = −3). Atomic positions during MD were stored every 10 steps.

Band structure calculations were performed taking SOC into account. Although the band gap is underestimated at the DFT-PBE level of theory, the band dispersion and the Rashba splitting should be properly captured. The band structure of supercells was unfolded to a primitive Brillouin zone corresponding to a pseudocubic structure. The unfolding was performed with a "fold2Bloch" utility [38].

A spin texture was analyzed in the following way. The spinor wave function is represented as a linear combination

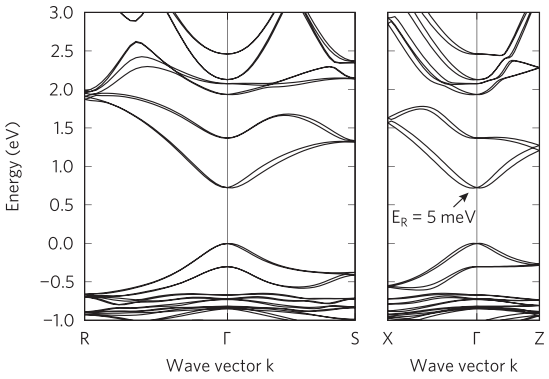


FIG. 4. Relativistic band structure of tetragonal $(CH_3NH_3)PbI_3$ with lattice parameters scaled to 300 K and relaxed $PbI_3$ cage. The Rashba splitting is present, but its magnitude is less that $k_BT$ at room temperature.

of spin up and down components,

$$|\psi\rangle = \alpha|\uparrow\rangle + \beta|\downarrow\rangle = \begin{pmatrix}\alpha\\ \beta\end{pmatrix}, \tag{4}$$

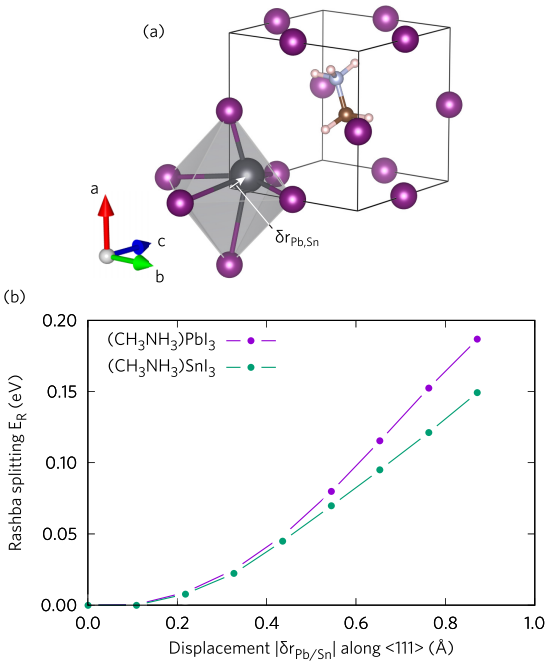


FIG. 5. (a) Displacement vector $\delta\boldsymbol{r}$ of the Pb or Sn atom from the center of the octahedron formed by iodine atoms. (b) Rashba splitting in a cubic structure as a function of the displacement of the Pb or Sn atom from its centrosymmetric position.

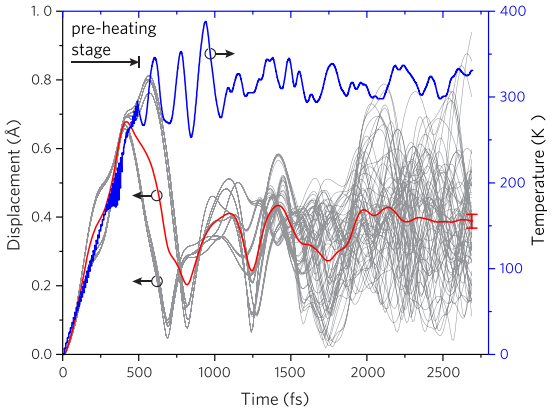


FIG. 6. Time evolution of a displacement $\delta r_{Pb_i}$ of Pb atoms from the center of their individual octahedra (gray curves, left axis), the average $\langle\delta r_{Pb}\rangle$ for all Pb atoms in the supercell (red curve, left axis), and temperature $T$ of the MD ensemble (blue curve, right axis). First 500 fs correspond to the preheating stage. Displacements fully dephase after approximately 2000 fs and $\langle\delta r_{Pb}(t)\rangle$ stabilizes.

that fulfill the normalization requirement $\alpha^2 + \beta^2 = 1$. Spin projections for individual eigenstates

$$\langle S_m\rangle = \langle\psi|\sigma_m|\psi\rangle \quad (m = x, y, z) \tag{5}$$

were computed along Cartesian coordinates (VASP tag LORBIT = 11, PROCAR file). Here $\sigma_m$ are Pauli matrices. The spin projections are related to spinor components as

$$\langle S_x\rangle = \alpha^*\beta + \beta^*\alpha, \tag{6a}$$
$$\langle S_y\rangle = i(\beta^*\alpha - \alpha^*\beta), \tag{6b}$$
$$\langle S_z\rangle = \alpha^2 - \beta^2. \tag{6c}$$

It is possible to determine $\alpha$ and $\beta$ from Eqs. (6) with the uncertainty of a phase factor $e^{i\theta}$, which affects neither the relative contribution of spin up/down components nor the spin overlap between two states. The uncertainty was resolved by constraining $\mathrm{Im}(\alpha) = 0$ that is consistent with eigenvectors of Pauli matrices.

The inverse participation ratio (IPR) $\chi$ was used as a measure of localization. It was evaluated on the basis of probabilities $\rho_n(E_i)$ of finding an electron with an eigenenergy $E_i$ within a muffin tin sphere centered at an atomic site $n$ [39,40]:

$$\chi(E_i) = \frac{\sum_n \rho_n^2(E_i)}{\left[\sum_n \rho_n(E_i)\right]^2}. \tag{7}$$

Here the summation index $n$ runs over all atomic sites.

## III. RESULTS AND DISCUSSION

### A. Static structures

We begin with presenting the electronic structure of tetragonal $(CH_3NH_3)PbI_3$ with lattice parameters scaled to $T =$ 300 K and the $PbI_3$ cage symmetry [Fig. 3(a)] obtained from x-ray diffraction studies [36]. The quasidirect band gap is

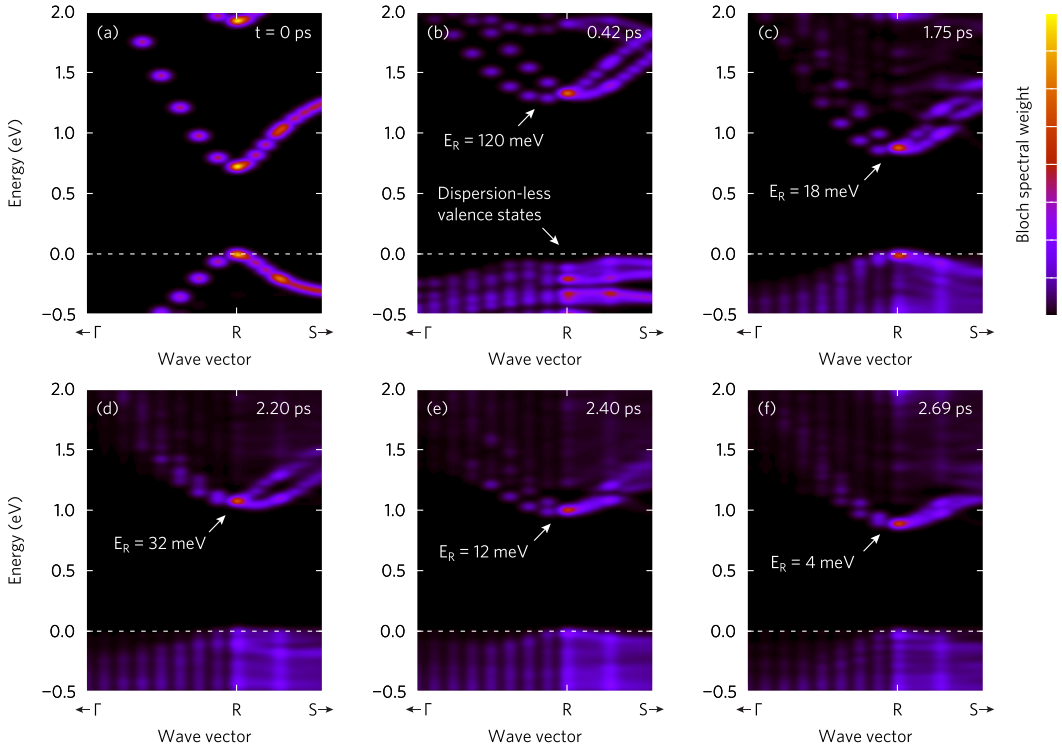


FIG. 7. Effective band structure of $4 \times 4 \times 4$ tetragonal $(CH_3NH_3)PbI_3$ supercell at different MD time snapshots: (a) $t = 0$, (b) 0.42 ps, (c) 1.75 ps, (d) 2.20 ps, (e) 2.40 ps, and (f) 2.69 ps. The Bloch character degrades at the VBE. Values for the Rashaba splitting $E_R$ were derived from all eigenvalues in the calculation, including those that do not appear on the $k$ path selected for the band structure plot. The strongest dynamical enhancement of $E_R$ is observed at the initial time steps. Data points were smeared using a Gaussian function with the standard deviation of $\sigma_k = 0.0025$ Å$^{-1}$ in $k$ space and $\sigma_E = 25$ meV on the energy scale.

typically observed at the $R$ point of the Brillouin zone [Fig. 3(b)]. However, the $R$ point is folded into Γ in the tetragonal phase [Fig. 3(c)]. The corresponding band structure is presented in Fig. 3(d) and shows no Rashba splitting as also noticed in Ref. [26]. A small nondegeneracy occurs at the band edges due to the field from methylammonium cations.

Experimentally, tetragonal $(CH_3NH_3)PbI_3$ has a centrosymmetric Pb-site symmetry even though the whole structure lacks an inversion center. Etienne *et al.* [26] and Kepenekian and Even [41] noted that Rashba splitting occurs due to breaking a *site* inversion asymmetry. This symmetry argument explains the absence of the Rashba splitting in Fig. 3(d).

Next, we fully relax atomic positions in the tetragonal structure (CCDC deposition No. 1870791) and repeat the calculation of the band structure. The relaxed structure shows a signature of Rashba splitting at the Γ point at the conduction band edge (CBE), although its magnitude is rather weak ($E_R = 5$ meV, Fig. 4), which is comparable to $E_R = 10$ meV found in relativistic quasiparticle calculations [30]. This result implies that the symmetry of the $PbI_3$ cage is broken after relaxation. The Rashba splitting is more prominent in the conduction band that is mostly composed of Pb-$p$ orbitals (83%) with a minor contribution from I-$p, s$ (14%). The orbital character at the valence band edge (VBE) has significantly less contribution from lead: I-$p$ (70%) and Pb-$s$ (30%).

To quantify a displacement of the Pb atom from the center of mass of an octahedron formed by iodine atoms [see Fig. 5(a)] we use the following expression:

$$\delta \boldsymbol{r}_{\mathrm{Pb}} = \boldsymbol{r}_{\mathrm{Pb}} - \frac{1}{6}\sum_{i=1}^{6} \boldsymbol{r}_{\mathrm{I}_i}. \tag{8}$$

Here $\boldsymbol{r}_{\mathrm{Pb}}$ and $\boldsymbol{r}_{\mathrm{I}_i}$ refer to the Cartesian coordinates of the corresponding atomic species. The tetragonal structure with relaxed atomic positions has a displacement of about $\delta r_{\mathrm{Pb}} \sim 0.1$ Å. Our results are consistent with the Pb-displacement value of 0.09 Å reported by Liu *et al.* [42] for the tetragonal phase. The displacement in a cubic structure is greater (about 0.25 Å [43]), which results in a larger magnitude of $E_R$ typically found in those structures [44].

To link the magnitude of the Rashba splitting $E_R$ with the displacement of the Pb atom, we performed calculations for a cubic structure ($a = 6.29$ Å) by varying $\delta \boldsymbol{r}_{\mathrm{Pb}}$ with I atoms fixed at their perfect positions expressed by the fractional coordinates $(1/2, 0, 0)$ and permutations of that. The most

effective displacement direction for enhanced $E_R$ is along the diagonal of the cube ⟨111⟩ [Fig. 5(a), CCDC deposition No. 1870792]. The largest Rashba splitting is observed in the $k$ plane that is perpendicular to the displacement vector $\delta \boldsymbol{r}_{Pb}$; the splitting vanishes for $k$ paths oriented parallel to the displacement vector.

Results for $E_R(\delta r_{Pb})$ are shown in Fig. 5(b). It is interesting that the same structure with Sn instead of Pb (used as a lead-free alternative to $(CH_3NH_3)PbI_3$ perovskites [45]) shows a comparable $E_R$ in spite of a drastic difference in the SOC constant between Pb and Sn ($\lambda_{SO} = 0.91$ eV vs 0.27 eV [46], respectively). At first this result may look counterintuitive since it is commonly accepted [47] that the Rashba parameter $\alpha_R$ is proportional to $\lambda_{SO}$, which leads to the much stronger dependence $E_R \propto \lambda_{SO}^2$. However, the SOC constant $\lambda_{SO}$ is determined for isolated atoms and serves as an approximation for orbitals that are significantly altered by chemical bonding. Comparable values of $E_R$ for Pb-based and Sn-based structures suggest that the vector product of an effective asymmetric electric field $\boldsymbol{E}_0$ experienced by electrons and their velocity $\boldsymbol{v}$ averaged over possible trajectories for a given orbital is similar in both cases.

For the splitting energy to reach $k_B T \approx 26$ meV at room temperature, the displacement should be on the order of 0.3 Å [Fig. 5(b)], which is far above the static displacements of Pb atoms in the tetragonal phase of $(CH_3NH_3)PbI_3$. Does the lattice dynamics provide sufficient distortions for the Rashba splitting to exceed 26 meV?

### B. Dynamic structures

Now we turn our attention to the dynamic structure of $(CH_3NH_3)PbI_3$. The supercell size selected in our calculations greatly exceeds previous simulations [26,30], which provides a more realistic model for structural fluctuations and allows access to phonon modes that are otherwise not present in smaller cells. Figure 6 shows a time evolution of $\delta r_{Pb}$. The dynamic amplitude of $\delta r_{Pb}$ near room temperature can reach 0.8 Å, and the average displacement stabilizes near 0.37 Å. According to Fig. 5, we would expect a much stronger Rashba splitting in those structures.

Interpretation of band structure calculations of supercells is not straightforward due to a band folding. Here, we used an unfolding technique implemented in the "fold2Bloch" utility [38]. Effective band structures of the $(CH_3NH_3)PbI_3$ supercell, taken at different MD simulation times, are shown in Fig. 7 (structure files can be accessed at CCDC deposition Nos. 1870785–1870790). As anticipated, the initial ($t = 0$) structure features no Rashba splitting [compare Fig. 7(a) and Fig. 3(d)] and serves as a benchmark for comparison with other structures. The Bloch character of primitive wave vectors $k$ (pseudocubic in this case) is well defined for the initial structure, which is indicative of periodicity of the wave function preserved throughout the supercell.

It should be noted that values of the Rashba splitting $E_R$ in Fig. 7 are evaluated with respect to the CBE in the *full* Brillouin zone

$$E_R = E_{CB}(R) - \min[E_{CB}(\boldsymbol{k})]. \quad (9)$$

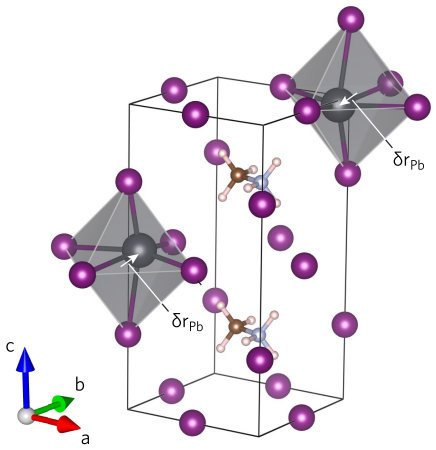


FIG. 8. Perovskite structure with two Pb atoms displaced in opposite directions by the same magnitude.

The energy eigenvalue $\min[E_{CB}(\boldsymbol{k})]$ may not necessarily lie on the Γ-$R$-$S$ path selected for the band structures in Fig. 7, which can give the impression of an inconsistency between the band structure and $E_R$ values. At $t = 0.42$ ps, for instance, the CBE unfolds into $\boldsymbol{k} = (1/2, -0.375, 1/2)$ with the Bloch spectral weights of 62%. Since this $k$ point does not belong to the Γ-$R$-$S$ path, the band structure in Fig. 7(a) does not capture the full extent of the Rashba splitting, whereas $E_R$ does.

In dynamic structures we observe breaking of the Kramers degeneracy with the most pronounced Rashba splitting of $E_R \approx 120$ meV [Fig. 7(b)] observed in the conduction band near the end of the preheating stage ($t = 0.42$ ps). It is a manifestation of the dynamic Rashba splitting present even in centrosymmetric structures [21,28,30]. This time frame corresponds to the maximum average displacement in Fig. 6 and sets an upper limit for dynamic $E_R$. It is instructive to analyze this result, but it can hardly be physically plausible since the MD displacements of Pb atoms are still coherent at this time. The Rashba splitting gradually decreases as the dynamics of Pb atoms becomes less coherent [Figs. 7(d)–7(f)] even though the average displacement vector $\langle \delta r_{Pb}(t) \rangle$ remains steady at the MD time $t > 2$ ps (Fig. 6). This behavior suggests that not only the displacement magnitude but also a mutual orientation of displacement vectors play a role in determining $E_R$.

To verify this hypothesis, we created a supercell where Pb atoms in two $PbI_6$ octahedra had equal displacements by magnitude but opposite in direction ($\delta \boldsymbol{r}_{Pb1} = -\delta \boldsymbol{r}_{Pb2}$) as shown in Fig. 8 (CCDC deposition No. 1870793). In spite of sizable displacements ($\delta r_{Pb} = 0.5$ Å), the Rashba splitting completely vanishes in this structure. To rationalize this result, we recall that the effective asymmetric electric field $\boldsymbol{E}_0$ that causes Rashba splitting is aligned with the displacement $\delta \boldsymbol{r}_{Pb}$. When atoms are displaced in opposite directions, the electric field on each atomic site opposes the other leading to cancellation of the net effective electric field. This reasoning explains why dynamic structures have a small $E_R$ despite a relatively large average displacement.

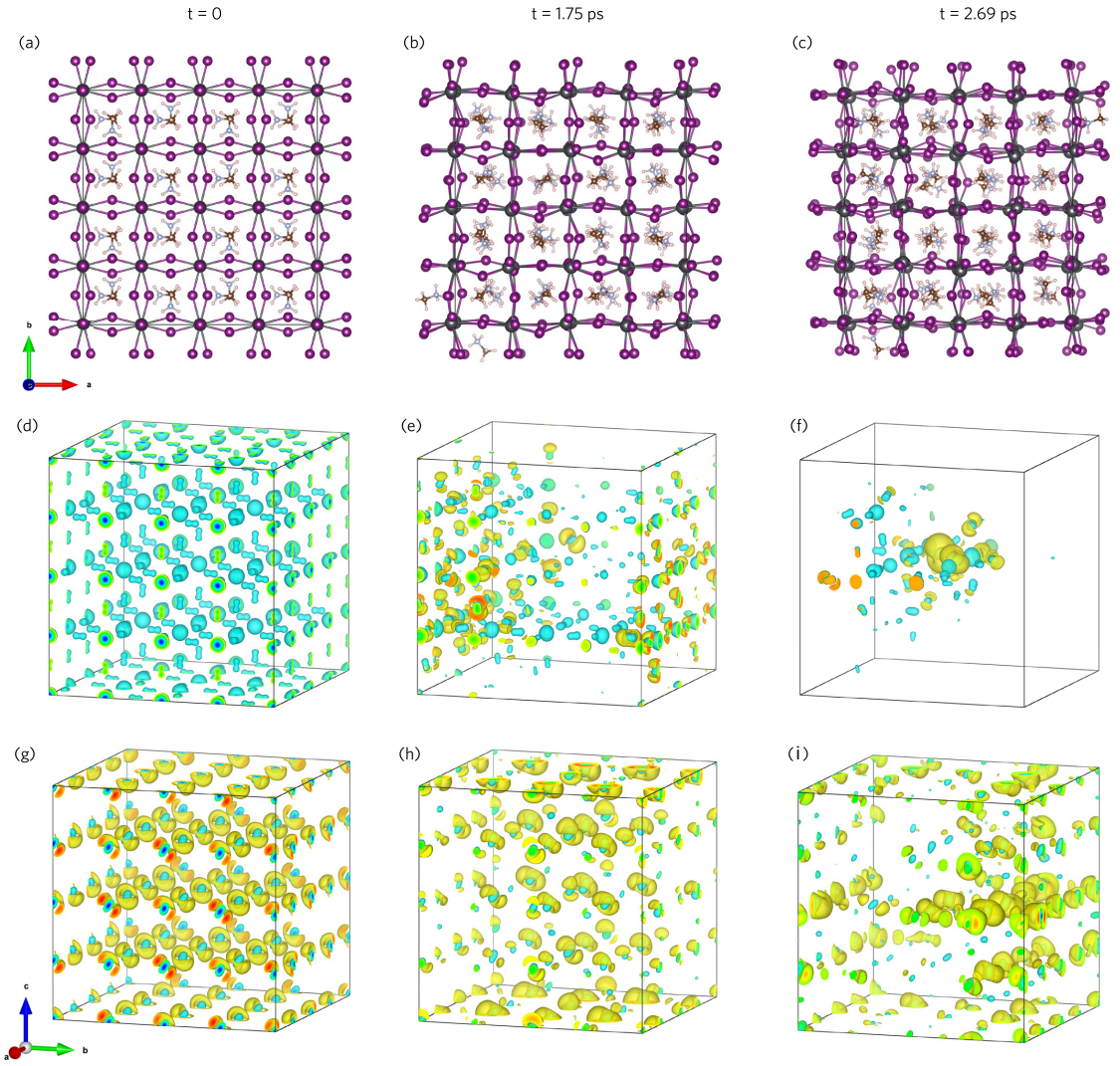


FIG. 9. (a)–(c) $4 \times 4 \times 4$ tetragonal $(CH_3NH_3)PbI_3$ supercell structure at different MD time steps and the corresponding spatial distribution of DFT orbitals $\psi_i(\boldsymbol{r})$ for (d)–(f) VBE and (g)–(i) CBE states. Isosurfaces correspond to the values of $\psi = \pm 5 \times 10^{-4}$.

Next, we discuss the valence band. In Fig. 7, the valence band becomes too disordered to make any conclusions about Rashba splitting there. This result suggests that $k$ is not a good quantum number for holes in the dynamic structure of $(CH_3NH_3)PbI_3$. The loss of Bloch character at the VBE undermines the argument about an indirect band gap [Fig. 1(b)], which implies that $\Delta k$ is well resolved. Instead, the prolonged carrier lifetime can originate from a weak overlap in real and reciprocal space between extended electron states and localized hole states.

For solar cells it is important to have a material with good bipolar transport properties. It is known that mobility decreases with $T$ due to electron-phonon scattering, which is also true for perovskites [48]. The question is whether the charge transport coefficients of electrons and holes are equally susceptible to thermal structural fluctuations. To address this question, we plot the wave function of electronic eigenstates at the VBE and CBE in Fig. 9. The structural fluctuations impact the spatial coherency of wave functions at the band edges. Electronic states at the VBE undergo the most significant changes which eventually leads to their spatial localization [Fig. 9(f)]. Electronic states at the CBE seem to be more robust against thermal structural fluctuations, which is also consistent with their better ability to retain the Bloch character (Fig. 7).

To further explore possible localization of electronic eigenstates, we present IPR spectra in Fig. 10 for structures at different MD time snapshots. IPR represents the inverse number

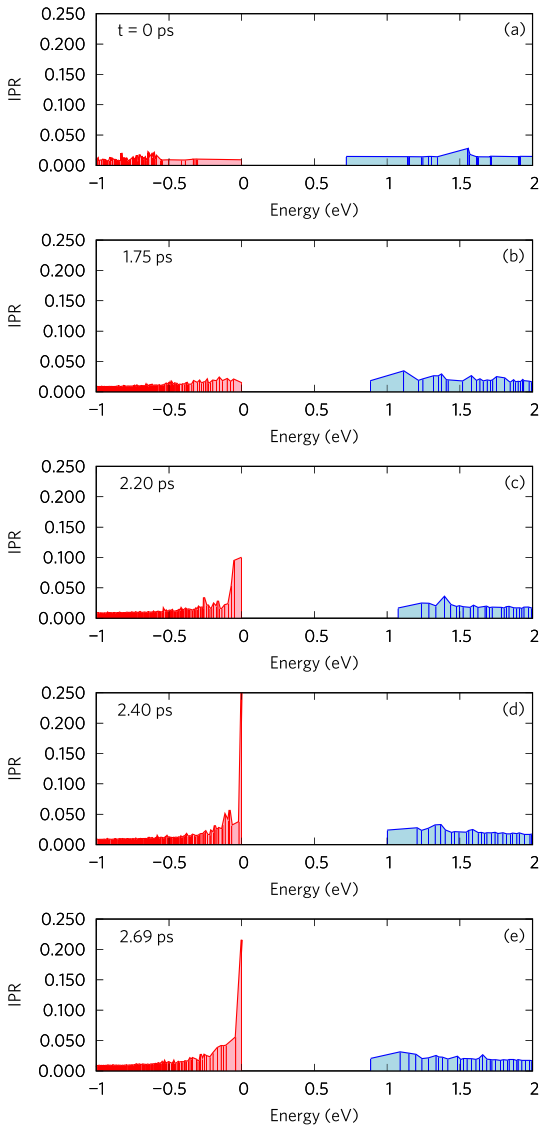


FIG. 10. Spectrally resolved inverse participation ratio for states in vicinity of the band gap of $4 \times 4 \times 4$ tetragonal $(CH_3NH_3)PbI_3$ supercell taken at different MD time snapshots: (a) $t = 0$, (b) 1.75 ps, (c) 2.2 ps, (d) 2.4 ps, and (e) 2.69 ps. A spatial localization of the DFT orbitals takes place at the valence band edge due to dynamic atomic displacements. The structural fluctuations open the band gap, which continues to change dynamically.

of atoms that contribute to an eigenstate. Localized states exhibit higher IPR values. The initial structure [Fig. 10(a)] sets a baseline for the IPR spectrum in the case of a localization-free structure. The IPR spectrum shows a clear distinction between structures at 1.75 and 2.69 ps. A spike in the IPR spectrum at the VBE [Fig. 10(e)] confirms localization of these states. Additional spectra obtained at MD times of 2.2 and 2.4 ps [Figs. 10(c) and 10(d)] confirm that the localization in the VBE is a persistent feature, not a random occurrence. Thus, we would expect the mobility of holes in $(CH_3NH_3)PbI_3$ to be much more sensitive to thermal structural fluctuations (phonon scattering) than the mobility of electrons. This result is consistent with a steeper increase of the effective mass of holes with temperature predicted earlier [49].

By observing changes in the band gap in Fig. 10, we can conclude that the dynamic structural disorder opens up the band gap substantially as also noticed by Saidi *et al.* [50] and McKechnie *et al.* [30]. After opening, the band gap continues to change dynamically with fluctuations of ∼0.3 eV, which is consistent with the literature [28,50]. It is interesting to note that the band gap renormalization of such a large magnitude due to the structural dynamic is inherent to wide band gap materials only. Furthermore, the renormalization typically leads to a *decrease* of the band gap [51] contrary to what is observed in perovskites where the gap widens.

Finally, we would like to comment on a spin texture at the band edges of perovskites. The long carrier lifetime is sometimes also attributed to spin-forbidden optical transitions rooted in the Rashba splitting [12]. Figure 11 presents the band structure of cubic $(CH_3NH_3)PbI_3$ [$\delta_{Pb} = 0.54$ Å, Fig. 5(a)] with three spin projections $\langle S_x \rangle$, $\langle S_y \rangle$, and $\langle S_z \rangle$. The Rashba valleys show a spin splitting with the symmetry $E(\boldsymbol{k}, \boldsymbol{S}) = E(-\boldsymbol{k}, -\boldsymbol{S})$ leading to a spin helicity. Optical transitions between CBE and VBE are hindered, provided the initial and final states have an opposite spin helicity. However, this is not the case in Fig. 11 where CBE and VBE have *similar* spin projections. Using spin projections it is possible to determine spinor components ($\alpha$ and $\beta$, see Sec. II) and the spin overlap at the band edges. Results presented in Table I indicate an almost perfect spin overlap of 99% between the two states representing CBE and the corresponding top of the valence band shown by the arrow in Fig. 11(c). The spin overlap remains high (greater than 90%) in the tetragonal phase of $(CH_3NH_3)PbI_3$ (Table I). Examination of spin states in two dynamic structures ($t = 0.42$ and 2.69 ps, Table I) reveals no changes in this trend. Thus, we reach the conclusion that the spin helicity poses no barriers for recombination of optical excitations in $(CH_3NH_3)PbI_3$ contrary to Ref. [12].

## IV. CONCLUSIONS

The extended carrier lifetime in hybrid halide perovskites was attributed to a quasi-indirect band gap that arises due to Rashba splitting in both conduction and valence band edges. In this paper we calculated the effective relativistic band structure of $(CH_3NH_3)PbI_3$ with the focus on the dispersion of electronic states near the band edges of $(CH_3NH_3)PbI_3$ affected by thermal structural fluctuations. The disorder is explicitly modeled via *ab initio* molecular dynamics simulation performed for a large supercell. A semiempirical scaling of the lattice parameters was used to achieve a finite-temperature structure of $(CH_3NH_3)PbI_3$.

Our preliminary studies involving static structures indicated that a tetragonal $(CH_3NH_3)PbI_3$ with the $PbI_3$ cage symmetry fixed to that obtained from x-ray diffraction studies shows no Rashba splitting even though the whole structure

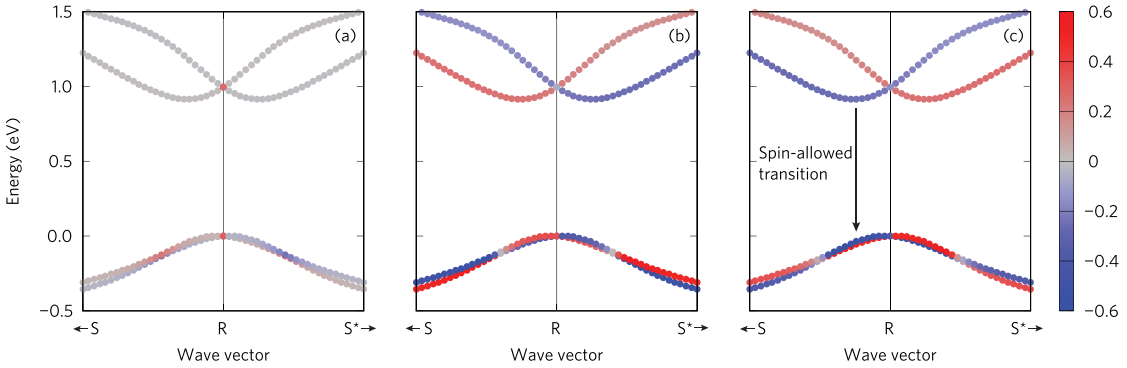


FIG. 11. Spin texture (a) $\langle S_x \rangle$, (b) $\langle S_y \rangle$, and (c) $\langle S_z \rangle$ in a symmetrized unit cell of cubic $(CH_3NH_3)PbI_3$ with Pb atom displaced by 0.54 Å along the [111] direction from the center of an octahedron formed by iodine atoms [Fig. 5(a), CCDC deposition No. 1870792].

lacks the inversion center. This result is attributed to a centrosymmetric Pb-site symmetry. The fully relaxed tetragonal structure showed a weak Rashba splitting ($E_R = 5$ meV), which occurs due to breaking a Pb-atom site inversion symmetry. For the splitting energy to reach $k_B T \approx 26$ meV at room temperature, the displacement should be on the order of 0.3 Å, which is far above the static displacements of Pb atoms in the tetragonal phase of $(CH_3NH_3)PbI_3$. Remarkably, lead-free perovskite structures (with Pb substituted by Sn while keeping the geometry the same) show a comparable $E_R$ despite a drastic difference in the spin-orbit coupling constants.

The dynamic average displacement of Pb atoms amounts to 0.37 Å at room temperature with the amplitude reaching 0.8 Å. The band structure of supercells taken at different time snapshots during molecular dynamics simulation were unfolded to a primitive (pseudocubic) Brillouin zone. The most pronounced Rashba splitting of $E_R \approx 120$ meV is observed when the dynamics of Pb atoms is still coherent. The dynamic Rashba splitting diminishes down to 4 meV as the molecular dynamics progresses to longer times (beyond 2 ps), which is assigned to randomization of Pb-displacement vectors and associated cancellation of the net effective magnetic field acting on electrons at the conduction band edge. At the same time, the valence band becomes disordered and loses the Bloch character that undermines the argument about an indirect band gap present in the dynamic structure of $(CH_3NH_3)PbI_3$ at room temperature. Analysis of the spatial distribution of DFT orbitals at the valence band edge reveals their spatial localization in the dynamic structures as also confirmed by the inverse participation ratio spectra. Electronic states at the conduction band edge are more robust against thermal structural fluctuations, which is also consistent with their better ability to retain the Bloch character. Thus, the mobility of holes should be much more susceptible to phonon scattering than the mobility of electrons. The finite-temperature structural dynamics opens the band gap that continues to fluctuate with the amplitude of ∼0.3 eV at the sub-picosecond time scale. Analysis of spin projections

TABLE I. Spin texture and spin overlap between the conduction band edge and the valence band in different structures of $(CH_3NH_3)PbI_3$.

| Parameter | cubic [$\delta_{Pb} = 0.54$ Å, Fig. 5(a)] | tetragonal | MD ($t = 0.42$ ps) | MD ($t = 2.69$ ps) |
|---|---|---|---|---|
| Conduction band edge | | | | |
| Wave vector $\boldsymbol{k}$ | [0.44, 1/2, 1/2] | [0.02, 0, 0] | [0, 1/2, 0] | [0, 0, 0.111] |
| Unfolded $\boldsymbol{k}$ (Bloch character) | | | [1/2, −0.375, 1/2] (62%) | [1/2, 1/2, 0.472] (56%) |
| $\langle S_x \rangle$ | 0.008 | −0.026 | −0.086 | 0.154 |
| $\langle S_y \rangle$ | 0.238 | 0.192 | −0.001 | −0.028 |
| $\langle S_z \rangle$ | −0.245 | −0.089 | 0.083 | −0.008 |
| Spin up $\alpha$ ($\lvert\alpha\rvert^2$) | $-0.376 + 0i$ (14%) | $-0.539 + 0i$ (29%) | $-0.920 + 0i$ (85%) | $0.690 + 0i$ (48%) |
| Spin down $\beta$ ($\lvert\beta\rvert^2$) | $-0.030 - 0.926i$ (86%) | $0.098 - 0.836i$ (71%) | $0.392 + 0.006i$ (15%) | $0.712 - 0.130i$ (52%) |
| Valence band | | | | |
| $\langle S_x \rangle$ | 0.063 | −0.021 | −0.033 | 0.228 |
| $\langle S_y \rangle$ | 0.322 | 0.367 | −0.035 | −0.043 |
| $\langle S_z \rangle$ | −0.524 | −0.452 | 0.135 | −0.187 |
| Spin up $\alpha$ ($\lvert\alpha\rvert^2$) | $0.276 + 0i$ (8%) | $0.335 + 0i$ (11%) | $0.985 + 0i$ (97%) | $0.432 + 0i$ (19%) |
| Spin down $\beta$ ($\lvert\beta\rvert^2$) | $0.185 + 0.943i$ (92%) | $-0.054 + 0.941i$ (89%) | $-0.118 - 0.123i$ (3%) | $0.887 - 0.167i$ (81%) |
| Spin overlap $\lvert\langle\psi_v\rvert\psi_c\rangle\rvert^2$ (%) | 99 | 95 | 91 | 90 |

and the spin overlap at the band edges rules out spin helicity as a possible mechanism for a long lifetime of optical excitations in perovskite structures.

## ACKNOWLEDGMENTS

The authors are thankful to Dr. Ray LaPierre from McMaster University for reading the manuscript. C.Z. and O.R. would like to acknowledge funding provided by the Natural Sciences and Engineering Research Council of Canada under the Discovery Grant Programs RGPIN-2015-04518. S.Y. would like to acknowledge funding provided by the Mitacs Globalink Research Internship program. DFT calculations were performed using a Compute Canada infrastructure supported by the Canada Foundation for Innovation under the John R. Evans Leaders Fund program.

C.Z. carried out MD simulations. S.Y. contributed the analysis of atomic displacements. O.R. designed the project, performed unfolded band structure calculations, and wrote the manuscript. All authors reviewed the manuscript before submitting for publication.

[1] A. Kojima, K. Teshima, Y. Shirai, and T. Miyasaka, J. Am. Chem. Soc. **131**, 6050 (2009).
[2] M. M. Lee, J. Teuscher, T. Miyasaka, T. N. Murakami, and H. J. Snaith, Science **338**, 643 (2012).
[3] M. Grätzel, Nat. Mater. **13**, 838 (2014).
[4] K. A. Bush, A. F. Palmstrom, Z. J. Yu, M. Boccard, R. Cheacharoen, J. P. Mailoa, D. P. McMeekin, R. L. Z. Hoye, C. D. Bailie, T. Leijtens *et al.*, Nat. Energy **2**, 17009 (2017).
[5] T. Singh and T. Miyasaka, Adv. Energy Mater. **8**, 1700677 (2018).
[6] Y. Yamada, T. Yamada, L. Q. Phuong, N. Maruyama, H. Nishimura, A. Wakamiya, Y. Murata, and Y. Kanemitsu, J. Am. Chem. Soc. **137**, 10456 (2015).
[7] D. Bi, W. Tress, M. I. Dar, P. Gao, J. Luo, C. Renevier, K. Schenk, A. Abate, F. Giordano, J.-P. Correa Baena *et al.*, Sci. Adv. **2**, e1501170 (2016).
[8] Y. Bi, E. M. Hutter, Y. Fang, Q. Dong, J. Huang, and T. J. Savenije, J. Phys. Chem. Lett. **7**, 923 (2016).
[9] T. Handa, D. M. Tex, A. Shimazaki, A. Wakamiya, and Y. Kanemitsu, J. Phys. Chem. Lett. **8**, 954 (2017).
[10] X. Ziang, L. Shifeng, Q. Laixiang, P. Shuping, W. Wei, Y. Yu, Y. Li, C. Zhijian, W. Shufeng, D. Honglin *et al.*, Opt. Mater. Express **5**, 29 (2015).
[11] J. Even, L. Pedesseau, J. M. Jancu, and C. Katan, Phys. Status Solidi Rapid Res. Lett. **8**, 31 (2014).
[12] F. Zheng, L. Z. Tan, S. Liu, and A. M. Rappe, Nano Lett. **15**, 7794 (2015).
[13] M. Kepenekian, R. Robles, C. Katan, D. Sapori, L. Pedesseau, and J. Even, ACS Nano **9**, 11557 (2015).
[14] G. Dresselhaus, Phys. Rev. **100**, 580 (1955).
[15] E. I. Rashba and V. I. Sheka, Fiz. Tverd. Tela: Collected Papers **2**, 162 (1959).
[16] G. Bihlmayer, O. Rader, and R. Winkler, New J. Phys. **17**, 050202 (2015).
[17] C. Katan, L. Pedesseau, M. Kepenekian, A. Rolland, and J. Even, J. Mater. Chem. A **3**, 9232 (2015).
[18] P. Azarhoosh, S. McKechnie, J. M. Frost, A. Walsh, and M. van Schilfgaarde, APL Mater. **4**, 091501 (2016).
[19] T. Wang, B. Daiber, J. M. Frost, S. A. Mann, E. C. Garnett, A. Walsh, and B. Ehrler, Energy Environ. Sci. **10**, 509 (2017).
[20] D. Niesner, M. Wilhelm, I. Levchuk, A. Osvet, S. Shrestha, M. Batentschuk, C. Brabec, and T. Fauster, Phys. Rev. Lett. **117**, 126401 (2016).
[21] D. Niesner, M. Hauck, S. Shrestha, I. Levchuk, G. J. Matt, A. Osvet, M. Batentschuk, C. Brabec, H. B. Weber, and T. Fauster, Proc. Natl. Acad. Sci. USA **115**, 9509 (2018).
[22] E. Menéndez-Proupin, P. Palacios, P. Wahnón, and J. C. Conesa, Phys. Rev. B **90**, 045207 (2014).
[23] F. Brivio, K. T. Butler, A. Walsh, and M. van Schilfgaarde, Phys. Rev. B **89**, 155204 (2014).
[24] P. S. Whitfield, N. Herron, W. E. Guise, K. Page, Y. Q. Cheng, I. Milas, and M. K. Crawford, Sci. Rep. **6**, 35685 (2016).
[25] G. M. Bernard, R. E. Wasylishen, C. I. Ratcliffe, V. Terskikh, Q. Wu, J. M. Buriak, and T. Hauger, J. Phys. Chem. A **122**, 1560 (2018).
[26] T. Etienne, E. Mosconi, and F. De Angelis, J. Phys. Chem. Lett. **7**, 1638 (2016).
[27] B. Monserrat and D. Vanderbilt, Phys. Rev. Mater. **1**, 054201 (2017).
[28] B. Monserrat and D. Vanderbilt, arXiv:1711.06274.
[29] T. Etienne, E. Mosconi, and F. De Angelis, J. Phys. Chem. C **122**, 124 (2018).
[30] S. McKechnie, J. M. Frost, D. Pashov, P. Azarhoosh, A. Walsh, and M. van Schilfgaarde, Phys. Rev. B **98**, 085108 (2018).
[31] G. Kresse and J. Furthmüller, Phys. Rev. B **54**, 11169 (1996).
[32] G. Kresse and J. Furthmüller, Comput. Mater. Sci. **6**, 15 (1996).
[33] W. Kohn and L. J. Sham, Phys. Rev. **140**, A1133 (1965).
[34] J. P. Perdew, K. Burke, and M. Ernzerhof, Phys. Rev. Lett. **77**, 3865 (1996).
[35] S. Grimme, J. Antony, S. Ehrlich, and H. Krieg, J. Chem. Phys. **132**, 154104 (2010).
[36] C. C. Stoumpos, C. D. Malliakas, and M. G. Kanatzidis, Inorg. Chem. **52**, 9019 (2013).
[37] H. J. Monkhorst and J. D. Pack, Phys. Rev. B **13**, 5188 (1976).
[38] O. Rubel, A. Bokhanchuk, S. J. Ahmed, and E. Assmann, Phys. Rev. B **90**, 115202 (2014).
[39] N. C. Murphy, R. Wortis, and W. A. Atkinson, Phys. Rev. B **83**, 184206 (2011).
[40] C. Pashartis and O. Rubel, Phys. Rev. Appl. **7**, 064011 (2017).
[41] M. Kepenekian and J. Even, J. Phys. Chem. Lett. **8**, 3362 (2017).
[42] S. Liu, F. Zheng, I. Grinberg, and A. M. Rappe, J. Phys. Chem. Lett. **7**, 1460 (2016).
[43] W.-L. Yan, G.-H. Lu, and F. Liu, J. Phys. Chem. C **120**, 17972 (2016).
[44] S. Hu, H. Gao, Y. Qi, Y. Tao, Y. Li, J. R. Reimers, M. Bokdam, C. Franchini, D. Di Sante, A. Stroppa *et al.*, J. Phys. Chem. C **121**, 23045 (2017).

[45] P. V. Kamat, J. Bisquert, and J. Buriak, ACS Energy Lett. **2**, 904 (2017).
[46] K. Wittel and R. Manne, Theor. Chim. Acta **33**, 347 (1974).
[47] S. Picozzi, Front. Phys. **2**, 1 (2014).
[48] R. L. Milot, G. E. Eperon, H. J. Snaith, M. B. Johnston, and L. M. Herz, Adv. Funct. Mater. **25**, 6218 (2015).
[49] Y.-B. Lu, H. Yang, W.-Y. Cong, P. Zhang, and H. Guo, Appl. Phys. Lett. **111**, 253902 (2017).
[50] W. A. Saidi, S. Poncé, and B. Monserrat, J. Phys. Chem. Lett. **7**, 5247 (2016).
[51] M. Cardona and M. L. W. Thewalt, Rev. Mod. Phys. **77**, 1173 (2005).